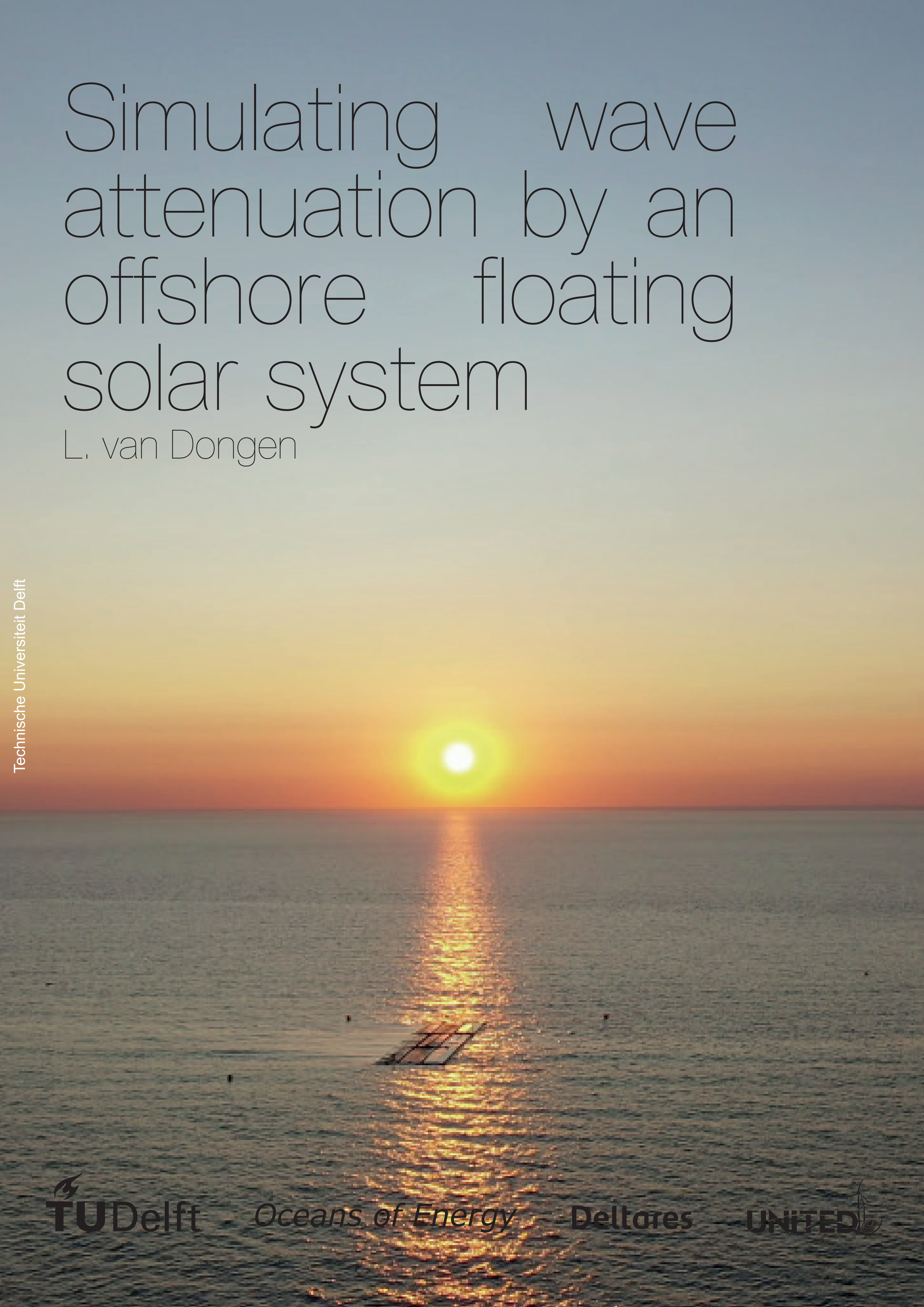

Simulating wave attenuation by an offshore floating solar system

L. van Dongen

Technische Universiteit Delft

TU Delft

Oceans of Energy

Deltares

UNITED

Simulating wave attenuation by an offshore floating solar system

by

L. van Dongen

to obtain the degree of Master of Science
at the Delft University of Technology,
to be defended publicly on Tuesday July 27, 2021 at 10:00 AM.

Student number:	4458885	
Project duration:	November 1, 2020 – July 27, 2021	
Thesis committee:	Dr. Ir. Y.M. Dijkstra,	TU Delft, supervisor
	Ir. A.J. van der Hout,	Deltares, supervisor
	Prof. Dr. Ir. M.B. van Gijzen,	TU Delft, chairman
Additional supervisors:	Ir. R.J. van der Wiel,	Oceans of Energy, supervisor
	Ir. R. Hoekstra,	Deltares, supervisor
	Dr. Ir. N.G. Jacobsen,	Deltares, supervisor

This thesis is confidential and cannot be made public until July 27, 2023.

TU Delft

Preface

Before you lies my thesis report ”*Simulating wave attenuation by an offshore floating solar system*”, which presents the research I conducted over the past eight months. I had the opportunity to do a graduation internship at Deltares and Oceans of Energy, where I could put my mathematical background to use by modelling the wave environment around a floating solar structure. This research is part of the UNITED project, a European research project regarding multi-use at offshore locations. This interesting context, the combination of practical work for scale model tests and numerical modelling, and the collaboration between two different parties made it an exciting and challenging graduation project.

I would like to thank everyone at Oceans of Energy for their inspiring spirit and their interest in my project. You welcomed me in the OOE family and showed me what real team work is! From my field trip to the North Sea, to everyone bringing their kids to the office to help with building the scale model, it was a great adventure. Hereby a special thanks to Gijs, Daniëlle, Erik, Kees, Fabian & Marco for helping me out with the 264 floaters and thousands of zip ties.

At Deltares, the enthusiasm for all water-related research topics showed for every employee I met, during my experiments in the Scheldt flume as well as from the guests at the online intern coffee moments. It was great to get to know the work environment of such a large knowledge institute, even though I was not able to work there in person due to the Covid restrictions.

Of course, I would like to thank all my supervisors for their guidance and support throughout this thesis. Niels Jacobsen, thanks for showing me how the mathematics I knew fitted within your field of expertise, and for the additional ’light reading material’ you dropped in my postbox. Roderik Hoekstra, for your support on the project management and the positive note in your feedback. Arne van der Hout, for jumping in right away when Niels went to Denmark. I learned from you that I should try to use my intuition and look at the bigger picture sometimes, instead of diving into the mathematical details. Robert van der Wiel, for asking the right questions and convincing me of the 80-20 rule, although I still have points to learn there. Lastly, I would like to thank Yoeri Dijkstra, in the first place for stepping into a graduation project with this many parties involved. I am thankful for your listening ear during our weekly meetings, and your flexibility in proofreading my work towards the end of the project.

Furthermore, I would like to thank my friends and family for their support in this past year. Papa, mama, Sophie and Friso, thanks for ensuring me that everything will be okay in the end during my times of stress. Here we are, I think you were right!

L. van Dongen
Delft, July 2021

Abstract

Because the demand for green energy increases rapidly, it is expected that solar and wind energy will dominate future power generation. New in this field is the development of offshore floating solar systems, consisting of multiple interconnected platforms that are covered with PV panels. Besides satisfying the demand for electricity, these floating solar systems may have a beneficial impact on their wave environment. If waves are attenuated, down-wave shadow zones could be useful for other marine activities such as aquaculture or for the protection of a harbour, and therefore create opportunities for offshore multi use. The overall research objective of this study is to research the effect of an interconnected multi-body floating solar structure on the transmission of wave height. This was done using a scale model test and a numerical model, in a two-dimensional setting.

From the scale model tests, wave transmission showed to be highly dependent on the wave frequency, and thus the wavelength, of the incident waves. The floating solar system acts as a low pass filter: it lets the low frequency waves pass through, whereas the waves with higher frequency are attenuated by the structure. This dependence is governed by the ratio between the incident wavelength and the length of the rigid platforms that the solar structure consists of, measured in parallel to the wave propagation direction. When the wavelengths were smaller than twice the length of a platform, waves were almost fully attenuated. Apart from the dependence on frequency, the basin test results also showed that the amount of wave attenuation increases linearly with the total length of the system, but only with a small slope. Furthermore, analysis of the reflected wave signal indicated that higher order dissipative effects are likely needed to describe the decrease in transmission accurately, because the amount of wave energy that was reflected by the structure was limited.

A proof-of-concept for applying a linear numerical boundary element diffraction model to a fixed shallow solar structure was carried out. The wave surface elevation could be obtained, and these solutions were in accordance with the physical expectations. The results showed similar trends to the basin test results, but did not match quantitatively. This difference could lie in the model approach, where a two-dimensional transmission coefficient is determined from three-dimensional simulations. It could also be that the scattering effects alone cannot approximate the transmission behaviour of the system, because linear radiation effects or higher order dissipation effects might be of similar importance and are therefore required for an accurate simulation. Radiation could be included in a linear diffraction model, but dissipation requires higher order wave theory.

Regarding the multi-use context, a down-wave shadow zone can form if the incident waves are short enough. For the North Sea location considered, where waves are typically longer than 25 m, the floating solar structure might not have the breakwater performance that is desired to protect other offshore activities.

Contents

1

Introduction

1.1. Context & Motivation

Because environmental issues rapidly increase the urge for green energy, it is expected that solar and wind energy will dominate future power generation. In 2019, only 19% of the European energy consumption was renewable [16, 20]. To increase this share to the expected 70% in 2050, wind and solar energy are highly promoted.

Until now, PV panels have been installed on land or at inshore waters, but this space is often scarce. Therefore, moving solar farms to the oceans and seas could be a major opportunity to increase the green energy production in a minimally invasive way, and even to fully satisfy the future energy demand. Additionally, floating solar PV panels are likely to have a higher efficiency than onshore solar farms due to the cooling effect of the water. The average annual output energy is more than 10% higher at sea [9, 22]. In combination with wind energy farms, the space at sea can be used efficiently. Also, using these energy resources together can offer a more stable and continuous power supply.

Besides satisfying the demand for electricity, floating solar farms may have an impact on their wave environment, reducing the wave height in certain locations. In this case, the solar system would have breakwater-like properties and a shadow zone could form down-wave of the floating structure. This could have benefits for other offshore activities, such as aquaculture, wind farms and protection of shores or harbours. Firstly, a location with smaller waves could be well suitable for aquaculture, for example seaweed cultivation. A seaweed farm system can handle waves up to certain wave heights or wave loads, above which the system can break down [23]. Therefore, a sheltered location is favourable as the farm is more likely to survive. Wind farms could also have benefits from deploying floating solar in between the wind turbines, such that they suffer lower wave loads. Lastly, if the solar structure is of significant size and would be deployed near shore, it could act as a floating breakwater to prevent coastal erosion or to protect harbours. For different stakeholders it could become important to predict the impact of the solar structure on the wave environment and the locations of potential shadow zones.

1.2. Existing research

Because offshore floating solar is still a young field of research and various system designs are considered, there have not yet been any studies on its wave attenuation properties. Therefore, other fields where wave-structure interaction is analysed form the basis of the existing literature.

Wave attenuation due to floating objects has previously been researched in the field of floating breakwaters. These are large structures that are installed to protect their leeward area of severe wave conditions. This way, a harbour, moored vessel, or part of a shoreline can be protected from excessive incident wave energy. The dynamics and performance of these floating structures have been studied intensively from the 1970s until now, see [12, 25] for reviews. Studies with scale model tests [32, 43], as well as ones exploring analytical solutions [24, 39, 58–60] and numerical models [24, 42, 44, 48], gave an extensive literature background to study the influence of a floating body on the wave field.

The scale model studies often measured the breakwater attenuation performance in a two-dimensional setting, with regular and irregular unidirectional plane waves (which means the wavefronts are parallel planes normal to the uniform propagation direction). Wave attenuation is quantified by means of a transmission coefficient K_t, which is defined as the transmitted wave height H_t (behind the floating object) over the incident wave height H_i

$$K_t = \frac{H_t}{H_i} \tag{1.1}$$

Because breakwaters are passive systems which do not create wave energy, $H_t \leq H_i$ and therefore $K_t \in [0,1]$. This is true for the entirely two-dimensional setting; if three-dimensional diffraction effects are present the transmitted wave behind the breakwater can be higher than the incident wave. When the object does not attenuate the incident waves $K_t = 1$, if the waves are fully blocked $K_t = 0$. Similarly, a reflection coefficient K_r is defined to measure the redirection of waves as

$$K_r = \frac{H_r}{H_i} \tag{1.2}$$

where H_r is the wave height for the reflected waves coming back from the floating object. This coefficient gives an indication whether the reflection of waves has caused the decreased transmission. By energy conservation, it should hold that the total incident wave energy is equal to the sum of the transmitted, redirected and dissipated wave energy: $E_i = E_t + E_r + E_d$. Because wave energy $E \propto H^2$, it must hold that [32]

$$K_t^2 + K_r^2 + K_d^2 = 1 \tag{1.3}$$

Thus, the relation between K_t and K_r shows the cause for any lack of transmission; if $K_t^2 + K_r^2 < 1$, there must be dissipation effects present.

In the analytical and numerical breakwater studies, linear wave theory is used to describe the wave-structure interaction. Non-linear dissipative effects such as wave-breaking, overtopping and eddies are neglected in this approach. Linear velocity potential theory is used to describe the radiation and scattering effects, which together form the linear hydrodynamics. A schematic overview of wave-structure interaction is given in Figure 1.1.

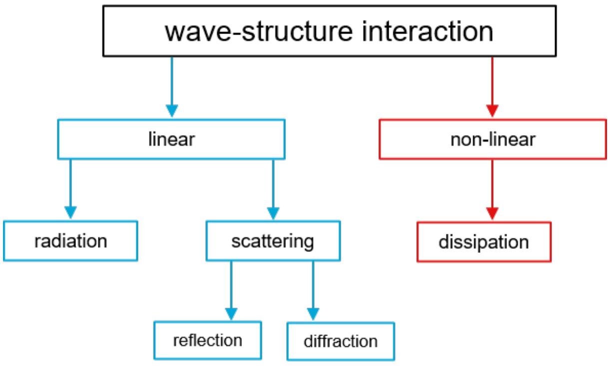

Figure 1.1: Schematic overview of effects that describe wave-structure interaction.

In a two dimensional setting, the linear effects of the structure will reflect and/or radiate part of the incident waves in opposite direction. Non-linear effects can dissipate the incident wave energy, and thus work as an energy sink. A schematic diagram of these effects is given in Figure 1.2

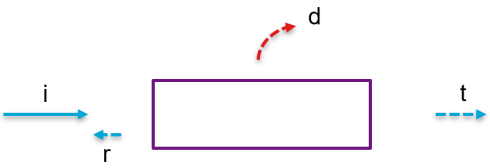

Figure 1.2: Schematic diagram of incident i, transmitted t, reflected r and dissipated d waves by influence of a floating object.

The radiation and scattering of waves by the breakwater can be solved analytically for the most simple cases, such as a floating pontoon breakwater over a flat bottom [24, 58, 60]. For other breakwater configurations, a boundary element method (BEM, also known as panel method) diffraction model can be used to find a description of the linear hydrodynamics. Such a model is designed to compute the hydrodynamic coefficients of a floating object, often a ship, which describe its motion and the wave loads.

Existing research on breakwater performance shows dependence on structural parameters, such as breakwater length, draft and mooring line stiffness, as well as wave environment parameters, such as wave height, wave period or wavelength and water depth. In case of multiple floating breakwaters, the spacing between the objects and the number of objects also determines the decreased wave transmission.

Although these breakwater studies give a framework to study wave-structure interaction and attenuation performance, it is not trivial if and how this wave analysis can be applied to the floating solar structure. For instance, the floating solar system consists of platforms with a relatively small draft, whereas breakwaters have a much larger draft as they are designed to reduce wave height. Also, this thesis focuses on the impact on the wave environment rather than a description of the object motion. Therefore, it should be investigated how the surrounding wave field or wave surface elevation can be derived from a diffraction model output. Moreover, BEM diffraction models are naturally designed to model one or a few floating objects at the time. Extending the calculations to a large number of objects can therefore bring challenges.

1.3. UNITED project and North Sea Pilot

The UNITED project is a European research project which aims to provide evidence that the development of multi-use platforms or co-location of different activities in a marine and ocean space is a viable approach (economically, socially and environmentally) for European maritime industry and local ecosystems.[1] Developing knowledge on the potential for upscaling floating solar wave attenuation for multi-use is one of the aims of the project. In total, 26 European partners participate in the UNITED consortium. Deltares coordinates the full project as well as the technological pillar.

The main activities centre around five pillars: technology, economy, environment, society and legal/policy/governance. This research fits well in the technological pillar ('how could the solar structure be optimised to create shallow wave conditions for multi-use?') and the environmental pillar ('what is the effect of the floating solar structure on the wave-environment?').

The project is based on five pilot demonstrators, which combine different kinds of offshore activities. The Dutch pilot, located 15 km offshore from Scheveningen, consists of an offshore wind farm, floating solar and seaweed cultivation.

The floating solar system is developed and maintained by Oceans of Energy, and was installed in 2019 as the first offshore solar farm on the North Sea. It consists of multiple interconnected rigid platforms covered with PV panels. A picture of the system is shown in Figure 1.3, a schematic top-view of a 4×2 floater system in Figure 1.4. The rigid platforms move as wave followers on the sea waves and the system is held in place with mooring lines. When the system is scaled up to a larger number of floaters, it could potentially bring shelter from incident waves for the wind or seaweed farms.

---

[1] UNITED is a European research project funded by the European Union Horizon 2020 programme under Grant Agreement number 862915. It stands for "multi-Use platforms and co-locatioN pilots boosting cost-effecTive, and Eco-friendly and sustainable production in marine environments". For more information on the UNITED project, see `https://www.h2020united.eu/`

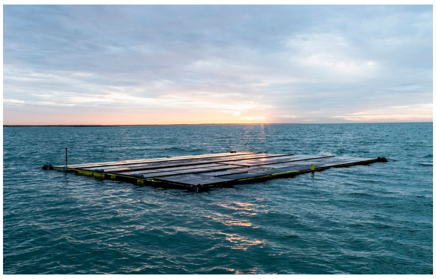

Figure 1.3: Oceans of Energy's floating solar system.

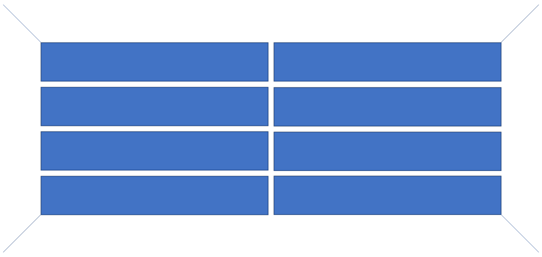

Figure 1.4: Schematic top view of the floating solar system, in a 4×2 floater configuration.

1.4. Research objective

The aim of this thesis is to research the effect of floating solar on surrounding wave field. Because wave attenuation due to the floating system can be caused by various physical processes, which either redirect or dissipate wave energy, the parameter that is investigated is the transmission of the waves. The overall long term research objective within the context of this study is defined as:

What is the effect of an interconnected multi-body floating solar structure
on the transmission of wave height?

In this thesis, a first step will be taken towards an answer to this question by using scale model testing and numerical modelling. A basin test will give an indication of the transmission through the solar structure, which physical effects are involved and what parameters govern the transmission behaviour. The numerical model could predict the wave environment around the floating solar structure, in various configurations and system sizes. This thesis will investigate a proof of concept for applying a linear boundary element method diffraction model to the floating solar structure, restricted to scattering only (see Figure 1.1). Finally, the results of both approaches will be compared.

To restrict the scope of this research, the focus will be on the near-field wave environment of the solar structure in intermediate water depth with a horizontal seabed. The wave transmission will be studied in a two dimensional setting, for regular and irregular (spectral) waves. Thus, the transmission of unidirectional plane waves (which means the wavefronts are parallel planes normal to the uniform propagation direction) through an interconnected, multi-body floating solar structure is considered. This setup is shown in Figure 1.5.

Within these restrictions, the following research questions will be investigated in this thesis:

1. How do the transmission and reflection coefficients, K_t and K_r, depend on the incident wave frequency f (and thus wavelength λ), the incident wave height H and the number of rows of floaters the model consists of n_{FL}? ⋆⋄
2. How well does the scattering solution of a linear boundary element method diffraction model describe the wave transmission through a multi-body floating solar structure? ⋆⋄
    (a) Physically: to what extent do linear effects, thus the redirection of wave energy, explain a decreased transmission? ⋆
    (b) Numerically: can a linear boundary element method diffraction model be applied to a shallow multi-body floating solar structure? ⋄

⋆ - question answered with basin test results
⋄ - question answered with numerical model results

For the numerical model, the focus was on answering question 2 by showing a proof-of-concept for modelling wave transmission by diffraction around a shallow floating object. Confidence lies in answering this question in the physical sense especially, the numerical applicability is discussed briefly with preliminary findings on mesh sensitivity.

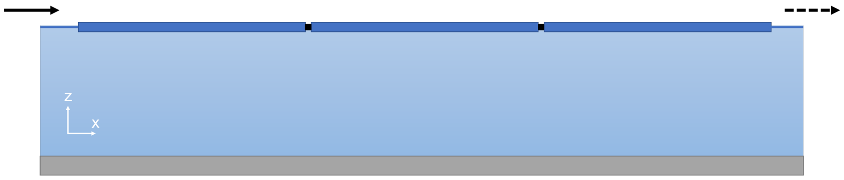

Figure 1.5: Schematic diagram of two-dimensional setup with horizontal seabed, number of floater rows $n_{FL} = 3$. Incident waves (solid arrow) propagate in positive x-direction through the floating solar system, and become transmitted waves (dashed arrow).

1.5. Research approach

The effect of the floating solar structure on the wave environment is researched in various ways. As a first step, the problem definition was specified mathematically. Linear velocity potential theory, focused on the diffraction of waves around a floating body, was used to formulate the physical problem into a mathematical description. The derivation of this description and the assumptions needed were studied and are described in Chapter 2.

This problem is then studied by using four different approaches, as illustrated in Figure 1.6. Central to these research lines is the problem definition.

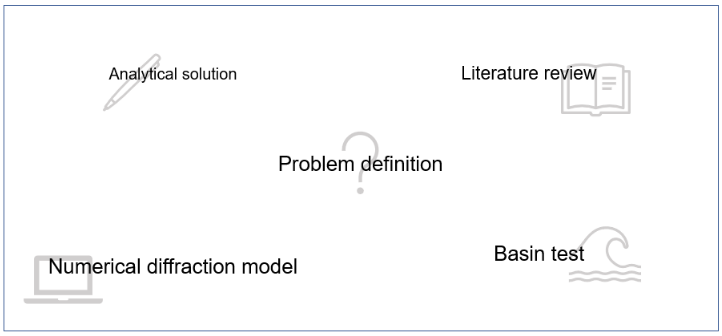

Figure 1.6: Diagram of the research approach.

The four research approaches are shortly explained below.

1. Literature review
   A hypothesis on the overall impact is formed by literature review on floating breakwaters. This also gives an insight in the parameter dependence of the problem and the way transmission can be defined.
2. Analytical solutions
   Linear velocity potential diffraction problem can be solved analytically in a two-dimensional setting for a single rigid barge and regular (harmonic) waves.
3. Numerical model
   The boundary element method diffraction model computes the surface elevation around the floating solar structure. A transmission coefficient is computed, dependent on frequency, for an approximately two-dimensional setup. Only the diffraction problem will be studied, where the object is fixed and affected by regular (harmonic) waves.
4. Basin test
   A basin test is done in a wave flume, where the effect of a floating solar scale model on regular and irregular waves is measured in a two-dimensional setup.

The results from these four pillars will be combined and compared. It should be noted that the analytical solution method is studied, but the final solutions have not been obtained completely. The basin test gives insights in the actual physical behaviour of the structure and shows the response in irregular weaves representing a JONSWAP spectrum [26, 28], which simulate the North Sea conditions. A numerical model gives the opportunity to vary parameters easily and to predict the effect of the structure in different configurations or large sizes. Therefore, the combination gives a more complete description and creates the opportunity to validate the model with the basin test results.

1.6. Structure of report

This report will start by introducing the mathematical problem description in chapter 2, which explains how to describe ocean waves, linear wave theory and wave-structure interaction. After that, chapter 3 will briefly discuss the literature review on floating breakwaters, which was mainly used to form a frame of reference for studying wave attenuation. Chapter 4 will dive into the scale model tests that were performed, followed by the numerical model in chapter 5. Here, the linear boundary element method diffraction model is introduced and a proof-of-concept is presented for simulating the wave environment around floating solar platform. The discussion in chapter 6 will combine the obtained results, present reflections on the work and give suggestions for further research. Finally, chapter 7 will state the conclusions of this research.

2

Mathematical problem description

The goal of this chapter is to give the mathematical description of the interaction between a floating multi-body (solar) structure and ocean waves. In order to formulate this problem, ocean waves will be described with first order velocity potential theory.

This chapter is structured in the following way. First, the description of ocean waves is introduced briefly. Linear potential flow theory for free surface waves in finite depth water is explained in section 2.2. After that, the equation of motion for rigid body dynamics is discussed in section 2.3. Lastly, the velocity potential theory and the rigid body dynamics are combined in section 2.4 on wave-structure interaction section.

2.1. Description of ocean waves

In order to describe ocean waves mathematically, a few definitions will be introduced first, based on Holthuijsen (2007) [28] and Journée and Massie (2008) [30].

The surface elevation $\eta(t)$ is defined as the instantaneous elevation of the sea surface relative to some reference level, often taken as the still-water level. The surface elevation profile between two downward zero-crossings is called a wave, shown in grey in Figure 2.1. Its wave height is then defined as the vertical distance between the highest and lowest surface elevation in the wave. Its wave period is defined as the time between two downward zero-crossings of the surface elevation.

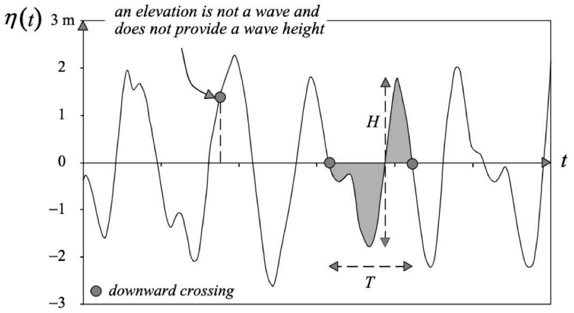

Figure 2.1: The definition of wave height H and wave period T in a time-record of surface elevation. [28]

The significant wave height is defined as the mean of the highest third of the waves in a record of observations. This is the wave height which is close to the visually estimated wave height, and is given by

$$H_s = \frac{1}{N/3}\sum_{j=1}^{N/3} H_j \tag{2.1}$$

In this definition, j is the rank number of the wave based on its wave height ($j = 1$ corresponds to the highest wave, $j = N$ to the lowest wave) and N is the total number of waves in the record.

2.1.1. Wave spectrum

When analysing ocean waves, they are often described by a wave spectrum. Observations of the surface elevation are formally treated as realisations of a stochastic process, therefore as time series. This treatment is based on the random-phase/amplitude model, which is explained in detail in Appendix A. The variance density spectrum gives a full description of the surface elevation of ocean waves in a statistical sense, as a function of time in one geographic location. It is given by

$$E_{var}(f) = \lim_{\Delta f \to 0} \frac{\mathbb{E}\{\frac{1}{2}\underline{a}^2\}}{\Delta f} \tag{2.2}$$

under the assumption that the surface elevation can be seen as a stationary Gaussian process. In this equation, f is the oscillation frequency of the surface elevation considered and Δf the frequency interval around it (which is send to 0 as a continuous spectrum is desired). $\mathbb{E}\{\frac{1}{2}\underline{a}^2\}$ shows the variance of the random wave component amplitude $\underline{a}$, which is Rayleigh distributed (see Appendix A).

The variance density spectrum gives insight in the distribution of waves over the frequencies and its units are [m^2/Hz]. All statistical characteristics of the wave field can be expressed in terms of $E_{var}(f)$. For example, the energy density spectrum can be derived from the variance density spectrum by multiplication with the water density ρ and gravitational constant g.

$$E_{energy}(f) = \rho g E_{var}(f) \tag{2.3}$$

Note that the unit of this energy density spectrum quantity is [kg/s], therefore the spectrum gives the distribution of energy [kg m^2/s^2] per unit surface area ·[m^{-2}] over the frequencies · [Hz^{-1}] = [s]. The shape of the energy density curve is thus the same as the variance density curve, only the values are scaled with a constant factor.

The total energy per unit ocean surface area of the wave spectrum is obtained in the following way, by integration over all frequencies

$$\mathrm{E} = \int_0^\infty E_{energy}(f)df = \int_0^\infty g\rho E_{var}(f)df \tag{2.4}$$

which is given in [kg/s^2].

From these wave spectra, the peak period T_p is defined as the wave period with the highest energy. This period thus translates to the frequency where the peak of the spectrum is located.

2.2. Linear potential flow theory

The derivation of the linear wave theory equations from the mass and momentum conservation are presented in Appendix B. The linear potential flow theory for free surface waves in finite-depth water will be central in the mathematical definition of the wave-structure interaction and is used in the numerical diffraction model

The assumptions that underlie the linear potential flow equations and their boundary conditions are the following:

1. small amplitude approximation: the wave amplitudes should be small compared to their wavelength as well as the water depth
2. water is assumed to be an ideal fluid: incompressible, with constant density and no viscosity
3. water body is continuous, so there are no air bubbles in the water domain considered

4. free wave assumption: the only force acting on the water is gravity force (wind-induced pressure and surface tension are thus excluded)
5. water particles cannot leave the water surface, i.e. no splashing or wave breaking
6. water particles cannot penetrate the bottom of the sea

Before the equations for linear potential flow theory can be introduced, a domain has to be defined. For a free-surface wave in Cartesian coordinates, the domain to solve for the water particle velocity u (and velocity potential ϕ, which will be introduced shortly) will be $(x, y) \in \mathbb{R}^2, z \in [-h, 0]$. The surface elevation $\eta(x, y)$ is taken relative to the still water level at $z = 0$. A two-dimensional cross section in (x, z) is shown in Figure 2.2 of a part of this domain.

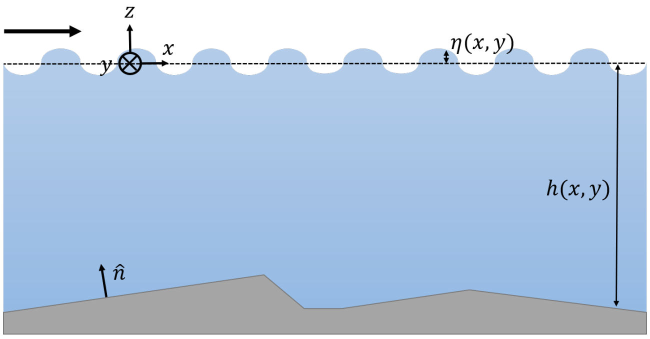

Figure 2.2: Domain of a free surface wave setup, shown in (x, z), with water depth $h(x, y)$, unit vector normal to the seabed $\hat{n}(x, y)$, and surface elevation $\eta(x, y)$. This example shows plane waves propagating in $+x$ direction, thus with propagation angle $\beta = 0$.

The linear wave equations are expressed in terms of the velocity potential function $\Phi(x, y, z, t)$, which is defined such that:

$$u_x = \frac{\partial \Phi}{\partial x}, \qquad u_y = \frac{\partial \Phi}{\partial y}, \qquad u_z = \frac{\partial \Phi}{\partial z} \tag{2.5}$$

where u_x, u_y and u_z are the particle velocities in x, y and z-direction respectively. The resulting continuity equation is given by the Laplace equation for Φ, which is

$$\nabla^2 \Phi = \frac{\partial^2 \Phi}{\partial x^2} + \frac{\partial^2 \Phi}{\partial y^2} + \frac{\partial^2 \Phi}{\partial z^2} = 0 \tag{2.6}$$

It can be solved for Φ using the kinematic boundary conditions (related to the motion of the water particles). These boundary conditions are linearised around the equilibrium water surface, taken $\eta(x, y, t) = 0$ at $z = 0$, which results into the expression

$$\frac{\partial \Phi}{\partial z} = \frac{\partial \eta}{\partial t} \qquad \text{at } z = 0 \tag{2.7}$$

for the surface boundary condition. When the water depth is assumed to be finite, defined as $z = -h(x, y)$, the kinematic boundary condition at the bottom is equal to

$$\nabla \Phi \cdot \hat{\mathbf{n}} = \frac{\partial \Phi}{\partial n} = 0 \qquad \text{at } z = -h(x, y) \tag{2.8}$$

where $\hat{\mathbf{n}}$ is the unit vector normal to the seabed. Note that when the seabed is assumed to be horizontal, this results in $\frac{\partial \Phi}{\partial z} = 0$.

The Laplace equation (2.6) and the (linearised) kinematic boundary conditions (2.7) and (2.8) are enough to solve for the velocity potential and hence all kinematic aspects of the waves. The dynamic behaviour of the waves (related to the forces acting on the water particles) can be found by using the linearised Bernoulli equation for unsteady flow, in combination with the dynamic surface boundary condition. This linearised Bernoulli equation follows from the momentum balance equation (see Appendix B), and is given by

$$\frac{\partial \Phi}{\partial t} + \frac{p}{\rho} + gz = 0 \tag{2.9}$$

where p is the pressure in the fluid relative to atmospheric pressure, ρ is the water density (assumed to be constant) and g is the gravitational acceleration constant. The linearised dynamic boundary condition is as follows

$$\frac{\partial \Phi}{\partial t} + g\eta = 0 \qquad \text{at } z = 0 \tag{2.10}$$

2.2.1. Propagating harmonic free-surface wave

If the motion described is assumed to be time-harmonic with a specified frequency, the velocity potential can be split in a complex position dependent potential $\phi(x, y, z)$ and a time dependent part

$$\Phi(x, y, z, t) = \text{Re}\{\phi(x, y, z)e^{-i\omega t}\} \tag{2.11}$$

In this case, the Laplace equation (2.6) should be satisfied by $\phi(x, y, z)$ throughout the fluid domain.

$$\nabla^2 \phi = 0 \tag{2.12}$$

In terms of ϕ, the linearised free-surface condition becomes

$$\frac{\partial \phi}{\partial z} = K\phi \qquad \text{on } z = 0 \tag{2.13}$$

where $K = \omega^2/g$, and the bed condition (2.8) becomes

$$\frac{\partial \phi}{\partial n_B} = 0 \qquad \text{on } z = -h(x, y) \tag{2.14}$$

The free-surface wave solution, for equations (2.12) - (2.14), is a plane wave of amplitude A and wavenumber k. In cylindrical coordinates, it is expressed by the following potential $\phi(r, \theta, z) \in \mathbb{C}$

$$\phi = -\frac{igA}{\omega \cosh kh} e^{ikr\cos(\theta - \beta)} \cosh k(z + h) \tag{2.15}$$

where its propagation angle is denoted with the angular coordinate $\theta = \beta$ from the x-axis. This velocity potential corresponds to the free-surface elevation below, derived from the dynamic condition (2.10).

$$\eta = Ae^{ikr\cos(\theta - \beta)} \tag{2.16}$$

To let this solution satisfy the free surface condition (2.13), $K = \omega^2/g$ and k have to be related by the dispersion relation as

$$K = k\tanh(kh) \tag{2.17}$$

2.3. Rigid body dynamics

To describe the dynamics of structures in water, a rigid body is the simplest structure to start with. A free floating, rectangular, impermeable rigid structure with appropriate dimensions can be seen as a simplified model of a floating solar structure. Therefore, it is relevant to start the study of rigid body dynamics in the first place.

The dynamics of a floating rigid body can be described with an equation of motion, based on Newton's second law. First, the degrees of freedom of a floating object are defined in section 2.3.1. After that, the equations of motion in frequency domain are introduced in section 2.3.2. In Appendix C, the rigid body dynamics are described in more detail.

2.3.1. Degrees of freedom

Six degrees of freedom are used to describe motion of an object at sea. The three translational directions in x, y, z are called surge, sway and heave. The three corresponding rotational directions are called roll, pitch and yaw respectively. An illustration of the definitions for these six degrees of freedom is given in Figure 2.3, the origin located at the object's centre of gravity.

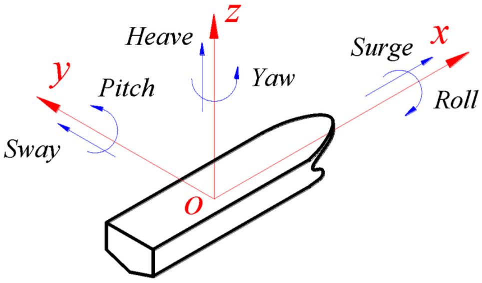

Figure 2.3: The 6 degrees of freedom of the centre of gravity: roll, pitch, yaw, heave, sway and surge. [14]

The object velocity of a point on the surface of the structure, measured normal to the surface, is given by V_n (see Appendix C). This velocity can be rewritten in terms of the modes of motion for these six degrees of freedom as

$$V_n = \sum_{j=1}^{6} U_j n_j \tag{2.18}$$

In this expression, $U_j = \mathrm{Re}(u_j e^{-i\omega t})$ for time-harmonic motion with the single frequency ω, and u_j the complex amplitude of the oscillations in mode j. The normals $\{n_j, j = 1, 2, 3\}$ are the x, y, z components of the unit normal vector $\vec{n}$ to the structure and $\{n_j, j = 4, 5, 6\}$ are the components of the cross product $\vec{r} \times \vec{n}$ with $\vec{r}$ the position vector for the centre of rotation.

2.3.2. Equations of motion

To describe the movement of a floating object, the linear equation of motion in time domain can be derived with Newton's second law, $\vec{F} = m\vec{a}$. This equation is often referred to as Cummins equation [10], an extensive explanation can be found in Journée & Massie (2008) [30]. It is difficult to use this equation to obtain the object velocity, because a convolution of the object velocity and a retardation function is used to evaluate the hydrodynamic damping force, which makes it difficult to solve. As this thesis focuses on wave attenuation in equilibruim state and there is no specific interest in the exact time-dependence, the frequency domain equations of motions are looked at instead.

The equation of motion for a floating object in frequency domain is given by [30]

$$\{-\omega^2(M + A(\omega)) + i\omega B(\omega) + C\}U(\omega, \theta) = F(\omega, \theta) \tag{2.19}$$

This equation consists of matrices and vectors, because the object velocity U is a vector that includes the oscillation modes in each degree of freedom, as introduced in section 2.3.1. In this equation, C is the structure stiffness matrix, $B(\omega)$ the hydrodynamic damping matrix, M the mass matrix of the floating structure, $A(\omega)$ is the hydrodynamic added mass matrix and $F(\omega, \theta)$ is the hydrodynamic force vector. The exact definitions and derivations of these matrices and vectors are given in Appendix C and they will be briefly explained here.

The equation of motion is used to solve for the body motion $U = (U_1, U_2, ..., U_6)$, included in equation (2.18) to express the velocity of the object. It is dependent on both the wave frequency ω and the incident wave angle θ. The matrices M and $C \in \mathbb{R}^6 \times \mathbb{R}^6$ are defined from the body dimensions, body mass, gravitational constant g and water density ρ and are thus constant. The added mass A, hydrodynamic damping matrix B and exciting force F can be found from linear velocity potential theory, their exact definitions will be explained in section 2.4.3. These coefficients are often computed using a boundary element diffraction model, which is introduced in Chapter 5. The physical properties of these matrices are as follows.

The added mass $A \in \mathbb{R}^6 \times \mathbb{R}^6$ can be explained as the mass of the water that is forced to move with the motion of the object considered. Thus, when an object oscillates in still water, the surrounding water volume that is caused to move due to acceleration of the body is considered to be the added mass. Added mass is given in [kg], is frequency dependent, and its value can differ per degree of freedom if the object considered is not symmetrical. The matrix element A_{ij} shows the effect of a unit amplitude motion of the object in degree of freedom i on the additional mass that has to be considered the equation of motion of mode j.

The hydrodynamic radiation damping $B \in \mathbb{R}^6 \times \mathbb{R}^6$ can be thought of as the damping due to the wave energy that radiates outward, away from a moving structure. The unit used to express radiation damping is [Ns/m] and it is dependent on the frequency ω. Again, if the object is not symmetrical, this will be different for movement in the various modes. The matrix element B_{ij} shows the damping effect of a unit amplitude motion of the object in degree of freedom i on the movement of the object motion mode j.

The hydrodynamic force $F \in \mathbb{C}^6$, also known as exciting force, is the force due to wave loads of the incoming and reflected waves. It gives the force or moment generated by a unit amplitude wave with wave frequency ω and incoming angle θ. This force is a combination of the Froude-Krylov and the diffraction force, which will be explained in section 2.4.3. The vector elements F_i give the force (for $i \in \{1, 2, 3\}$) or moment (for $i \in \{4, 5, 6\}$) ating on the object in the direction of the degree of freedom i. This force includes a phase term and is therefore complex valued.

All matrices are sized $n_{DOF} \times n_{DOF}$ when considering a single frequency ω. Here, n_{DOF} is the number of degrees of freedom that the body is assumed to have. If a rigid body can move freely in all directions, $n_{DOF} = 6$, as explained in section 2.3.1. However, if an object is restricted in its movement and can perform only heave motion for example, the matrix vector equation will be restricted to a scalar equation as $n_{DOF} = 1$.

2.4. Wave-structure interaction

Wave-structure interaction can be studied using linear velocity potential theory, for example to predict the motion of a ship or floating breakwater. An introduction has been given in section 1.2, with an overview of the effects present in Figure 1.1. In this section, these effects are discussed one by one: scattering in 2.4.1, radiation in 2.4.2 and dissipation in 2.4.4. Section 2.4.3 explains how the hydrodynamic coefficients in the equation of motion (2.19) can be derived from the complex spatial velocity potential ϕ.

Linear potential flow theory has been introduced for free surface waves in section 2.2. This theory can also be used to describe wave-structure interaction, by introducing different boundary conditions to the Laplace equation (2.6). Figure 1.1 already introduced the two types of linear wave-structure interaction: scattering and radiation. The scattering problem solves the velocity potential for a restrained object in water that is exposed to incoming waves; the object is held in fixed position and reflects the waves fully at its boundaries. The radiation problem expresses the velocity potential in case the object oscillates in water that is initially still. The addition of these descriptions will give back the total motion of an object in waves. This is visualised in Figure 2.4.

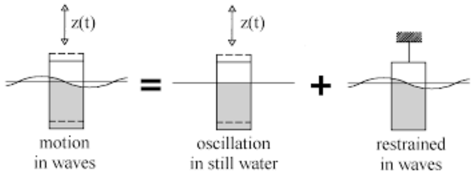

Figure 2.4: Motion in waves can be split up in a radiation problem, where waves radiate outward from an oscillating object in still water, and a scattering problem, where waves diffract around a fixed structure [30].

This way of mathematically splitting up the problem is possible due to the linearity of the velocity potential theory. This results in the following expression

$$\Phi = \Phi_S + \Phi_R = \Phi_I + \Phi_D + \Phi_R \tag{2.20}$$

In this equation, Φ_S is the solution of the scattering problem, in which the structure is held fixed in the waves. The scattered potential Φ_S may be decomposed into the incident undisturbed wave potential Φ_I and the diffracted wave potential Φ_D. Φ_I describes the free surface waves that are initially present, $\Phi_I + \Phi_D$ the resulting wave field when waves are diffracted and reflected by the object. The radiated wave potential Φ_R is the solution of the radiation problem, in which the structure is forced to oscillate in the absence of an incident wave.

Note that for time-harmonic motions, the time and space dependent parts can again be split by separation of variables into

$$\Phi_I = \text{Re}\{\phi_I e^{-i\omega t}\}, \qquad \Phi_D = \text{Re}\{\phi_D e^{-i\omega t}\}, \qquad \Phi_R = \text{Re}\{\phi_R e^{-i\omega t}\} \tag{2.21}$$

Here, Φ_I, ϕ_D and ϕ_R are complex valued functions of position only. The undisturbed incident wave potential ϕ_I is defined as the harmonic free-surface wave solution in equation (2.15). Thus, Φ_I is a known potential:

$$\Phi_I = \text{Re}\left\{-\frac{igA}{\omega \cosh kh} e^{ikr\cos(\theta-\beta)} \cosh k(z+h) e^{-i\omega t}\right\} \tag{2.22}$$

Φ_D and Φ_R have to be found from the Laplace equations with appropriate boundary conditions, which will be introduced in the next subsections. Remember that the numerical model will be restricted to the scattering solutions, $\Phi_I + \Phi_D$.

The domain in which this linear wave-structure interaction will be studied is shown in Figure 2.5. It is characterised by an intermediate water depth with horizontal seabed at $z = -h$. The wetted surface of the object in equilibrium state ($\eta = 0$) is defined as S_B, the body velocity by $\vec{V}$ and the normal vectors on the structure surface, directed out of the fluid, by $\hat{n}_B$. The complete domain is given by $(x, y) \in \mathbb{R}^2$, $z \in [-h, 0]$ for the free surface wave areas, $z \in [-h, -d]$ underneath the object.

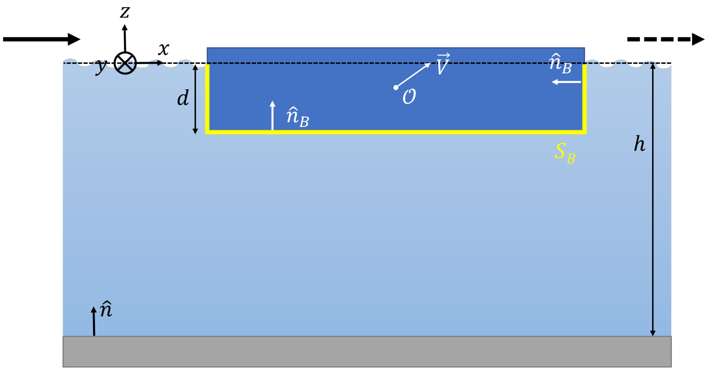

Figure 2.5: Domain for linear wave-structure interaction, shown as a cross section in (x, z), with horizontal seabed at $z = -h$ and unit vector normal to the seabed $\hat{n}$. The body has a centre of gravity at O, a velocity $\vec{V}$, wetted surface S_B and normal vectors directed out of the fluid $\hat{n}_B$. This example shows plane waves propagating in $+x$ direction, thus with propagation angle $\beta = 0$. The incident waves are pictured with the solid arrow, transmitted waves with the dashed arrow.

2.4.1. Diffraction problem

In the diffraction or scattering problem, the structure is assumed to be fixed at a certain location and it will not perform any motion. Therefore, the velocity of the water normal to any structure boundary must be zero (water will not penetrate the structure and the structure doesn't move). When the total velocity potential of this scattering subproblem is denoted by ϕ_S, the boundary condition that should hold is therefore

$$\nabla\phi_S \cdot \hat{\mathbf{n}}_B = \frac{\partial \phi_S}{\partial n_B} = 0 \qquad \text{on } S_B \tag{2.23}$$

Using $\phi_S = \phi_I + \phi_D$, this implies that for the diffraction potential

$$\frac{\partial \phi_D}{\partial n_B} = -\frac{\partial \phi_I}{\partial n_B} \qquad \text{on } S_B \tag{2.24}$$

The scattering problem is thus solving the Laplace equation (2.12) for ϕ_D within the fluid domains. It should satisfy the free-surface condition (2.13), the bed condition (2.14) and the fixed structure condition above (2.24).

To ensure a unique solution, the radiation condition must be satisfied as well. This condition specifies that the waves corresponding to the diffraction potential ϕ_D propagate outward; away from the structure. Infinitely far away from the structure, an undisturbed wave field should be present as the influence of the structure decreases far away. The same condition is also required for the radiation problem ϕ_R, explained in section 2.4.2. The mathematical description of this condition in two dimensions is as follows

$$\lim_{kx \to \pm\infty} \left(\frac{\partial \phi}{\partial x} \mp ik\phi \right) = 0 \tag{2.25}$$

for $\phi = \phi_D$ (or $\phi = \phi_R$) . If the problem is three dimensional, cylindrical coordinates are used in the x, y plane so that the radiation condition becomes

$$\lim_{kr \to \infty} \sqrt{r} \left(\frac{\partial \phi}{\partial r} - ik\phi \right) = 0 \tag{2.26}$$

The diffraction problem can be solved analytically for a two-dimensional setup, with an infinitely wide fixed barge [24, 39, 59, 60]. Appendix D explains the derivation of this analytical solution, based on separation of variables and a matched eigenfunction expansion in three subdomains. In the end, an infinite set of integral equations is obtained to find the complex weights for the eigenfunction modes. This can be truncated to a linear system of complex equations and solved numerically to approximate the analytical solution for the diffraction potential ϕ_D.

2.4.2. Radiation problem

In the radiation problem, the object moves in still water, which causes waves radiating outwards. For harmonic motion, the problem results in solving the Laplace equation (2.12) for ϕ_R within the fluid domains. ϕ_R is defined as in (2.21). It should satisfy the free-surface condition (2.13), the bed condition (2.14) and the body surface boundary condition (2.27) below. To ensure a unique solution, the radiating condition (2.25) or (2.26) should be satisfied for ϕ_R as well.

$$\frac{\partial \phi_R}{\partial n_B} = V_n \qquad \text{on } S_B \tag{2.27}$$

In this boundary condition, V_n is the component of the structural velocity in the direction of the normal coordinate n directed out of the fluid (equation (2.18)). This normal velocity is generally normalised at $V_n = 1$ in all directions, and can then be scaled with a motion amplitude afterwards because the problem is linear.

Using the complex amplitude of the oscillations in mode u_j as introduced in section 2.3.1, the radiation velocity potential ϕ_R can also be decomposed using linear superposition

$$\phi_R = \sum_{j=1}^{6} u_j \phi_{R,j} \tag{2.28}$$

where $\phi_{R,j}$ describes the wave field due to oscillations in mode j with unit velocity amplitude.

The object boundary condition (2.27) is satisfied with V_n given by (2.18) if

$$\frac{\partial \phi_{R,j}}{\partial n_B} = n_j \qquad \text{on } S_B, \text{ for } j = 1, 2, \ldots, 6 \tag{2.29}$$

Again, $\phi_{R,j}$ describes the wave field due to oscillations in mode j with unit velocity amplitude. This velocity potential should satisfy the free surface boundary condition (2.13), the bed condition (2.14) and additionally the radiation condition (2.25) or (2.26) to ensure a unique solution.

To find the normal velocity that results from the forces of the incident waves, and thus to determine the complex oscillation amplitude u_j, the equation of motion (2.19) has to be solved. Because this requires the (initially unknown) hydrodynamic coefficients, as described in section 2.4.3, the radiation problem is first solved with $V_n = 1$. The final velocity potential solution that expresses the actual wave-structure interaction is then found in second instance with the appropriate velocity components obtained.

This problem can also be solved using the matched eigenfunction expansion method, which is described for the diffraction solution in Appendix D [24, 60].

2.4.3. Hydrodynamic forces and moments

Now that the linear velocity potential theory for wave-structure interaction has been introduced completely in the previous sections, it is possible to connect this theory with the definition of the hydrodynamic coefficients. These were coefficients in the equation of motion (2.19) introduced in section 2.3.2. From the velocity potential solutions ϕ_I,ϕ_D and ϕ_R, it is possible to derive the frequency dependent coefficients A, B, and F.

Recall that in the diffraction problem, the floating object is kept still and the wave loads of incident and diffracted waves on the rigid, impermeable body are determined. These loads correspond to the exciting force F in the equation of motion. Therefore, it is possible to obtain F from the diffraction velocity potential ϕ_D and the incident undisturbed wave potential ϕ_I. Similarly, it is possible to derive the added mass A and radiation damping B for a rigid floating object from the radiation potential ϕ_R.

The integration of the dynamic pressure along the wetted surface of the body S_B is used to find the total hydrodynamic forces and moments. From the linearised Bernoulli equation (2.9), one can see that the hydrodynamic pressure term reads

$$p = -\rho \frac{\partial \phi}{\partial t} \qquad \text{for } z \approx 0 \tag{2.30}$$

The total force on a submerged structure is found by integrating this dynamic pressure multiplied by the unit normal vector along the wetted structure surface S_B. Because the linear problem can be split up in $\phi = \phi_I + \phi_D + \phi_R$, we obtain the hydrodynamic force

$$\mathcal{F}_{e,i} = -\int_{S_B} \rho \frac{\partial \Phi_I}{\partial t} n_i \,\mathrm{d}S - \int_{S_B} \rho \frac{\partial \Phi_D}{\partial t} n_i \,\mathrm{d}S - \int_{S_B} \rho \frac{\partial \Phi_R}{\partial t} n_i \,\mathrm{d}S \tag{2.31}$$

for each degree of freedom $i \in \{1, 2, ..., 6\}$. In this expression, the first term is the Froude-Krylov force and the second the diffraction force. Together, these forces combine to the excitation force vector F in the equation of motion (2.19). The third term is the radiation term, from which the added mass A and radiation damping B can be derived directly. The added mass is proportional to the acceleration and the radiation damping is proportional to the velocity. For time-harmonic motion, we can write $\mathcal{F}_{e,i} = \mathrm{Re}(F_{e,i} e^{-i\omega t})$.

To conclude, we obtain the expressions to find the hydrodynamic coefficients from section 2.3 from the linear velocity potential theory. For time-harmonic motion, such that $\Phi = \phi e^{-i\omega t}$ and $\partial\Phi/\partial t = -\mathrm{i}\omega\phi$, these expressions are

$$F_i(\omega) = \mathrm{i}\omega\rho \int_{S_B} (\phi_I + \phi_D) n_i \,\mathrm{d}S \tag{2.32}$$

for the exciting force F and

$$A_{ij}(\omega) + \frac{\mathrm{i}B_{ij}}{\omega} = \rho \int_{S_B} \phi_{R,i} n_i \,\mathrm{d}S \tag{2.33}$$

for the added mass A and radiation damping B. $\phi_{R,i}$ is the radiation potential for a unit amplitude oscillation in degree of freedom i.

A complete derivation of the hydrodynamic coefficients can be found in for example [36, 39].

2.4.4. Dissipation effects

In this research, linear velocity potential theory is applied to describe the wave-structure interaction. With this approach, all the dissipative effects are neglected and excluded from the model. This section aims to point out some of these higher-order, dissipative effects that could play a role in the wave-structure interaction.

Non-linear flow

When considering a single barge, viscous flow, vortex shedding and even turbulence could be effects that are present. When a barge with limited height (and thus small freeboard) is exposed to waves, these waves will tend to flow over the structure (overtopping), giving rise to friction and viscous flow therefore dissipating wave energy. Additionally, when the water will flow around the rigid structure, non-linear currents will show depending on the shape of the structure. With rectangular floaters, eddies will likely form at the corners for example. Reading on the causes for dissipation of a single barge or an array of independent barges can start with the references [11, 21, 30, 38, 42].

Mooring and interconnectors

When looking further into the solutions for interconnected and moored solar platforms, this will introduce even more possible dissipation effects such as water coming up through the gaps between the platforms and dissipation in the mooring lines or interconnectors through heat generation. Line friction on the sea bed and drag forces normal to the mooring line due to the motion of the lines through the water can also cause mooring line damping, but will be less influential in case horizontal mooring is assumed.

3

Floating breakwaters

Wave attenuation due to floating objects has previously been researched in the field of floating breakwaters. These are large structures that are installed to protect its leeward area of severe wave conditions. This way, a harbour, moored vessel, or even part of a shoreline can be protected from excessive incident wave energy.

The dynamics and performance of these floating structures has been studied intensively from the 1970s until this moment. Literature reviews that give an overview of the research performed are for example [12, 25]. Studies with scale model tests [32, 43], as well as ones exploring analytical solutions [24, 39, 58–60] and numerical models [17, 24, 42, 44, 48], gave an extensive literature background to study the influence of a floating body on the wave field.

A hypothesis on the impact of the floating offshore solar structure is formed by literature review on floating breakwater studies. First, the way breakwater performance is defined and studied will be explained in section 3.1. Then, section 3.2 presents the parameter dependence of this performance.

3.1. Breakwater performance: transmission coefficient

As floating breakwaters are designed to block or dampen out waves in order to protect a certain area, the wave field surrounding this breakwater is often a focus of their studies. In numerical or analytical research where linear, harmonic waves are considered, the wave field around the floating object is expressed in terms of either the complex spatial velocity potential $\phi(x, y, z)$ or the complex surface elevation $\eta(x, y, z)$. Their definitions have been explained in Chapter 2, based on $\Phi(x, y, z, t) = \phi(x, y, z)e^{-i\omega t}$.

In model tests or field tests however, it is not possible to derive the full surface elevation around the structure. Only at a few positions in space the surface elevation is measured. Therefore, it is convenient to describe the performance of a floating breakwater in terms of the wave height H in front and behind the structure. Namely, this wave height can be reconstructed from a collection of surface elevation measurements at a fixed location. Note that if the wave is regular and harmonic, the analytical or numerical expressions of $\eta(x, y, z) \in \mathbb{C}$ can also give the wave height as twice the amplitude of the complex surface elevation.

In terms of wave height, the performance of a floating breakwater can be defined by means of the transmission coefficient $K_t = H_t/H_i$, introduced in section 1.2. This measure is introduced to quantify the effect of the breakwater, without defining what the physical effect is that attenuates the waves. In other words, a transmission of less than 100% indicates the breakwater has an effect on the wave height behind the structure, but does not specify whether this is caused by for example reflection or dissipation.

From the transmission coefficient K_t it is also possible to derive the energy transmission (and thus the wave energy loss). Notice that wave energy $E \propto H^2$ in linear wave theory, such that K_t^2 gives an indication of the transmitted wave energy through the breakwater.

This transmission coefficient is dependent on many factors, which will be explained in section 3.2. The breakwater dimensions, water depth and wavelengths considered all influence the value of K_t. An exact expression is given by Macagno (1953) [45], based on linear wave theory and assuming no motion of the breakwater, no overtopping of water and a constant water depth [12, 25]

$$K_t = \frac{1}{\sqrt{1 + \left[\frac{k_i W \sinh(k_i h)}{2\cosh(k_i h - k_i d)}\right]^2}} \tag{3.1}$$

In this expression, $k_i = 2\pi/\lambda$ is the incident wave number, W the breakwater width, h the constant water depth and d the draft of the breakwater. This relation already indicates some of the important parameters that influence the wave transmission, which will be discussed in section 3.2 further.

3.2. Parameter dependence

Parametric studies which investigate breakwater performance for various wave and structural parameters were reviewed. Examples of the most relevant papers are [17, 58, 59]. Breakwater performance depends on wave environment and structure properties, and is often measured by the transmission coefficient K_t introduced in equation (1.1). The most important parameters that determine the wave transmission were found to be the following:

- length L (parallel to the incident wave direction)
- draft d
- mooring line stiffness K
- wave height H
- wave period T / wavelength λ
- water depth h
- regular / irregular waves
- direction of incident waves θ

Notice that the effect of the mass of the object is indirectly included through the combination of the object dimensions and the draft. In case of multiple floating breakwaters, the additional parameters were:

- spacing between adjacent breakwaters a
- number of breakwaters n_{FL} (parallel to the incident wave direction)

Most studies considered multiple breakwaters that were not connected to each other. However, if this would be the case, the dynamic properties of the connecting elements might also be of importance.

Some of the conclusions of these parameter studies that are relevant for this research were:

1. Floating breakwaters are most effective in low wave energy environments. [58]
2. Especially the ratio between the length parallel to the wave direction and the incident wavelength L/λ determines the breakwater performance. [17, 25]
3. Wave reflection properties of the structures depend strongly on their width, draft and spacing and the mooring line stiffnesses, while their excess buoyancy is of lesser importance. [58]

The general relations between the transmission coefficient K_t and the parameters introduced above were intuitive: a larger breakwater length L, draft d or number of breakwaters n_{FL} leads to less transmission and thus a better breakwater performance. However, the performance showed to be determined mainly by the ratio between the wave and the structure properties; the higher d/h or L/λ, the better the performance.

For the spacing between floaters a, in line with the incident wave direction, it could be concluded that narrow spacing is effective for reflecting long waves. The breakwater behaves as if it is continued in length, leading to more effective attenuation. For short waves however, a wider spacing is preferred because the floating bodies act as independent breakwaters in a sequence. [12, 58]

Regarding the mooring line stiffness K, the breakwater was more effective in reflecting long waves with a smaller stiffness, but this also leads to a more narrow wave frequency band where the breakwater performance is good. For short waves, the mooring stiffness does not have as much impact, although the motion of the floater should be restrained [12, 58]. Also, the eigenfrequency of the floating object is approximately equal to $\omega = \sqrt{K/m}$, with m the mass of the object. If the floating structure is subject to incident waves with this frequency, resonant behaviour can occur and the amplitude of this object oscillation mode can increase. This could lead to an increased transmission, because of the waves radiating outward. Therefore, it is convenient if the eigenfrequency of the mooring system is outside the intended performance interval of the breakwater.

The incoming wave angle θ can increase or decrease the efficiency of the breakwater because the L/λ ratio changes if the waves come in at an angle. For a single breakwater, an orientation of 45 degrees with respect to the incoming wave leads to the most efficient behaviour because L/λ is larger [12].

Especially the dependence on the incident wavelength (and thus wave frequency or wave period) is investigated in this study, which will be discussed in the next section.

3.2.1. Floater length to wavelength ratio

Because the wavelength dependency will be studied in both the numerical model and the basin test, the ratio L/λ is relevant to look into further. Because the breakwater (and eventually the floating solar structure) consists of rigid rectangular platforms, the waves will be forced to pass underneath. In general, the longer the breakwater with respect to the wavelength, the lower the transmission coefficient. A narrow breakwater is almost transparent for the long waves; it has a negligible impact.

Literature review by Hales (1981) [25] concluded that the wave attenuation features improve markedly and net result of forces on mooring and anchoring system becomes substantially less for $L/\lambda > 0.5$. This is because wave dynamics are exerting forces on a part of the structure in a direction opposite to those forces on other parts of the breakwater. Because the breakwater is assumed to be rigid, these forces lead to deformation of the wave; the floating structure cannot follow the wave neatly any longer. More recent literature review by Dai et al. (2018) [12] confirms this rule of thumb for various types of floating breakwaters; the length has to be at least half the wavelength. For smaller structures, the waves can pass underneath the floating breakwater, such that it acts as a wave follower.

From the experimental study by Wang et al. (2010) [57], it followed that transmission decreases below $K_t < 0.5$ for a length to wavelength ratio $L/\lambda = 0.35$. Note however that the exact transmission coefficient depends on more parameters. The experiments presented in [32] for a fixed breakwater in shallow and intermediate waters showed that the efficiency of the structure is considered satisfactory for a ratio $L/\lambda \geq 0.25$. Examples of exact transmission plots as a function of wavelength λ, dimensionless wavelength λ/L, or dimensionless parameter kh can be found in the following papers [12, 18, 25, 58, 59].

4

Basin test

A basin test was carried out as part of this thesis, with the goal to research the effect of the floating interconnected multi-body solar system on the waves. This effect can be subdivided in transmission, reflection and dissipation of the waves, and could be used as a comparison or validation for the numerical results.

First, the method is explained in section 4.1. After that, the test results are presented in section 4.2 and summarised in 4.3. The points of discussion, as well as the comparison with the numerical model results, will be discussed later in Chapter 6.

4.1. Method

The first part of this method section will explain experimental method of the basin test, in section 4.1.1. This includes a brief explanation of the design of the model, the flume setup and the wave conditions. Thereafter, the analysis method is presented in section 4.1.2.

4.1.1. Experimental setup

The scale model test was done in the Scheldt flume[1] at Deltares on a scale of 1:25. Froude scaling was used because the inertial effects were assumed to be more important in the floater dynamics than the viscous effects, see Appendix G. In this experimental setup section, all dimensions are given at basin test scale, unless stated otherwise. When the results are presented in section 4.2, all dimensions are translated to full (offshore) scale so that the results can be compared to offshore wave conditions and the numerical results of Chapter 5 more easily.

The wave attenuation caused by the floating solar structure was found by measuring the wave height in a two dimensional setup. The surface elevation was measured by 8 wave gauges in total, 4 in front and 4 behind the floating structure. These measurements were done for various wave conditions and floating solar system sizes, to test how the wave transmission depends on

- the wave frequency f, and therefore the wave period T and wavelength λ
- the wave height H
- the system size, thus then number of platforms the model consists of

Calibration tests were done in the empty flume such that effects on the waves that were not caused by the floaters could be eliminated.

In this section, the total setup of the tests will be discussed in more detail. The flume setup, model design, floater configurations and wave conditions will be explained.

---

[1] For more information on the Scheldt flume, see `https://www.deltares.nl/nl/faciliteiten/scheldegoot/`

Flume setup

A schematic overview of the configuration of the floating solar system, its mooring points, and the measurement devices in the Scheldt flume is presented in Figure 4.1. A picture of the setup is shown in Figure 4.2, and the exact positions of the objects present in the flume, measured from the wave paddle, are given in Table 4.1.

The setup was (approximately) two dimensional as the waves propagate along the 50 m long flume. The water depth was set to 0.85 m. Plane waves propagate in x-direction along the length of the basin. They have a surface elevation in z-direction and are considered constant in y-direction. Therefore, only one (orthogonal) incoming angle $\theta = 0$ is considered.

The waves are created by the wave paddle and propagate through the first set of wave gauges (WHM 1-4) towards the system. Behind the system, the waves are measured again with the second set of wave height meters (WHM 5-8). At the end of the flume, the waves are dampened out for the largest part. A reflected wave will travel back through the system, but can be filtered out in the result analysis. Any reflected waves that end up at the beginning of the flume are actively dampened out by the wave paddle; the Active Reflection Compensation (ARC) is used.

For all tests, second order steering was used for the wave paddle. This compensates for spurious waves and creates much of an airy wave as possible.

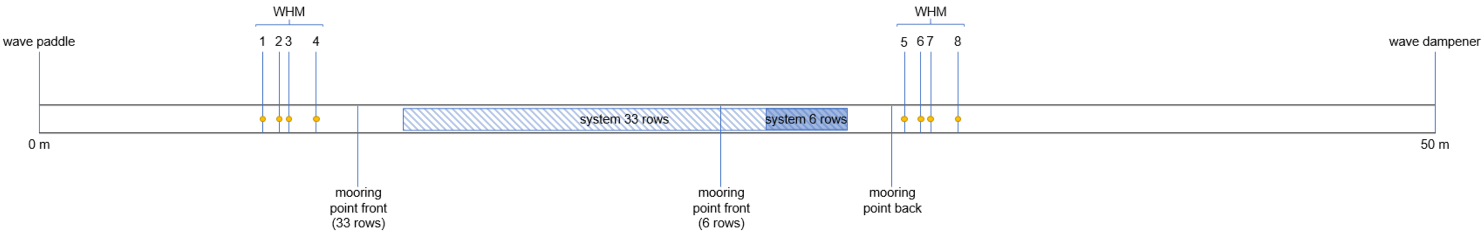

Figure 4.1: Schematic top-view of setup in the Scheldt flume. Wave paddle generates a wave propagating to the right. Surface elevation of the water measured by wave height meters WHM1-8, centred in the middle of the flume. Minimum system size of 6 rows of floater arrays and maximum system size of 33 rows of floater arrays are shown. The positions of these objects are also given in Table 4.1.

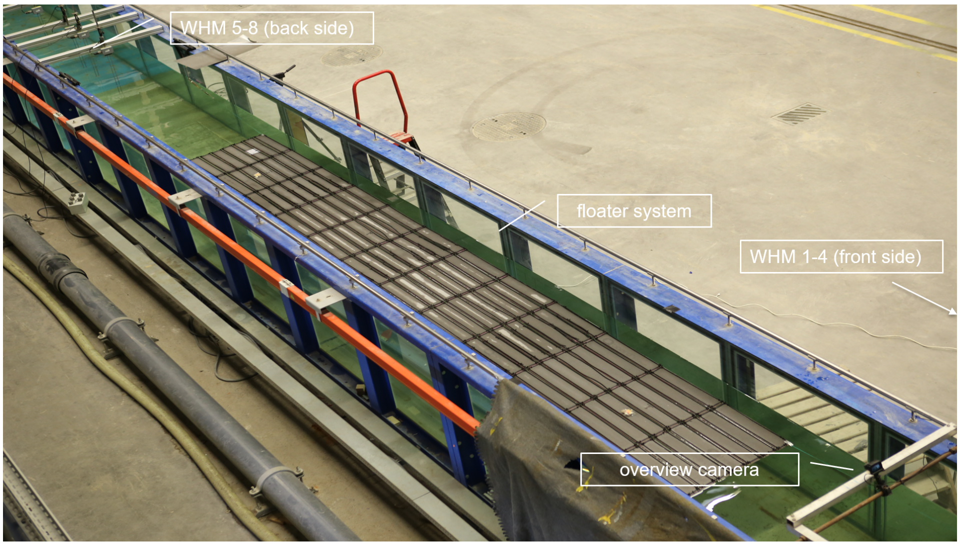

Figure 4.2: Picture of the flume setup with a configuration of 12 by 8 floaters.

object	position [m]
wave paddle	0.0
WHM 1	8.0
WHM 2	8.6
WHM 3	8.9
WHM 4	9.9
mooring point front (33 rows)	11.4
fore system (33 rows)	13.0
mooring point front (6 rows)	24.4
fore system (6 rows)	26.0
aft system	28.9
mooring point back	30.5
WHM 5	31.0
WHM 6	31.6
WHM 7	31.9
WHM 8	32.9
wave dampener	50.0

Table 4.1: Position of objects in Scheldt flume, measured from the wave paddle.

In Appendix H, the setup of the measurement devices, the floating model and the mooring connection are explained in more detail.

Design of the model

For the design of the model, the floating solar system of Oceans of Energy was taken as basis. Its properties were scaled back to the model scale, see Table 4.2. Together with the dimensions of the flume, this also imposed the maximum number of floaters that would fit into the width of the basin, which was 8. These rows of 8 floaters were installed perpendicular to the wave propagation direction and then connected together in the direction parallel to the flume. The top view of such a setup is shown in Figure 4.2.

physical parameter	full size	model size (desired)	model size (realised)
floater length [m]	11.75	0.47	0.47
floater width [m]	2.13	0.085	0.085
floater height [m]	0.22	0.009	0.012
floater mass [kg]	2400	0.154	0.20*
floater draft [m]	0.093	0.004	0.004
gap size [m]	0.3	0.012	0.012
water depth [m]	21.25	0.85	0.85
max wave height [m]	8.0	0.32	0.32

Table 4.2: Basin test model parameters, shown for full scale and model scale. The middle column gives the desired model dimensions by using scaling, the right column gives the actual realised dimensions.
* The weight of a single floater with interconnectors attached was measured at 0.17 kg when dry, 0.20 kg when water was absorbed (into the concrete layer).

The floater height and mass were realised slightly different from the intended parameters, but this difference is small enough. Namely, a realistic simulation of the offshore floating structure is still realised as the growth of additional mussels would also lead to increased mass and draft.

The floaters were made of XPS[2] isolation panels with a concrete top and bottom layer. This material approximately had the desired density, was easy to work with and not too expensive. The interconnectors in between the floaters were simulated using NBR rubber cord with a 4 mm diameter. These were attached on top of the floaters with zip ties, at the same location of the floaters as the full scale system.

---

[2] Extruded polystyrene, consists of closed cells and therefore offers higher stiffness and less water absorption than expanded polystyrene ('piepschuim' in Dutch).

Floater configurations

To determine the effect of the system size, the number of floater rows was gradually increased during the tests. This was done to investigate the influence of the number of floater rows n_{FL} on the transmission K_t. During the tests, the system was expanded with new floater blocks in direction of the wave paddle (as can be seen in Figure 4.1). The system size configurations that were used during the tests are show in Table 4.3.

test file label	number of floater arrays	total number of floaters
A	0	0
B	6	48
C	12	96
D	18	144
E	24	192
F	33	256

Table 4.3: System size configurations used during the basin tests. The first column shows the name of the test series, denoted by a letter. The second column shows the number of floater rows present in these tests. The third column shows the total number of floaters which are then present, which is equal to 8 times the number of floater arrays.

Wave conditions

In total, 32 different wave conditions were tested for each floater configuration. The majority of these tests were regular waves, to see exactly what happens for a singe frequency or wavelength and specified wave height. These are the kind of waves that the diffraction model (Chapter 5) will also describe, and are therefore well suitable for comparison. Spectral wave conditions were tested to see what the response is to the actual North Sea conditions. A JONSWAP spectrum is used to simulate the wave environment at the offshore test site.

The 25 regular wave conditions that were tested are given in Appendix I, Table I.1. These were chosen such that the dependencies on the wave height, wave period (or wavelength) and system size could be isolated from the results. Wave heights varied from $H = 0.04$ m to $H = 0.32$ m at basin scale, translating with scale factor $s = 25$ to waves in between $H = 1$ m and $H = 8$ m. Wave periods were chosen in between $T = 0.6$ s and $T = 5$ s, which scales with a factor of $\sqrt{s}$ to $T = 3$ s and $T = 25$ s (swell waves).

For the irregular wave tests, the exact conditions are given in Appendix I, Table I.2. Five North Sea conditions with increasing wave energy were chosen, based on measurement data of most occurring sea states [1]. Their significant wave heights varied from $H_s = 0.04$ m to $H_s = 0.20$ m, which corresponds to $H_s = 1.0$ m up to $H_s = 5.0$ m at offshore scale. The peak periods were minimally $T_p = 1$ s and maximally $T_p = 2$ s, which translates to $T_p = 5$ s and $T_p = 10$ s on full scale. Two additional tests were added with less steep waves.

For more information on the choice of these wave conditions, please see Appendix I.

4.1.2. Analysis method

Time series analysis

Now that the experimental setup has been introduced, the method to obtain transmission and reflection results from the raw measurement data is explained in this section.

In every wave test, the surface elevation is measured with a frequency of 400 Hz by 8 wave gauges. The resulting time series data is combined and processed to filter out forward and backward propagating waves. Both the first set of wave gauges, wave height meters 1-4, and the second set of wave gauges, wave height meters 5-8, will give a forward and backward propagating wave signal each. Therefore, the time series analysis results into four signals:

- Forward propagating waves in front of system (WHM 1-4) - $p1$
- Forward propagating waves behind floating system (WHM 5-8) - $p2$
- Backward propagating (reflected) waves in front of system (WHM 1-4) - $r1$

- Backward propagating (reflected) waves behind floating system (WHM 5-8) - $r2$

In Figure 4.3, a schematic diagram of these wave signals is given. The definitions of the wave heights H_{p1}, H_{r1}, H_{p2} and H_{r2} are shown.

Figure 4.3: Schematic diagram of the four wave signals that are found from the time series measurements by the wave gauges. The arrows show the propagation direction of the wave signal.

The separation into the wave signals that propagate in opposite direction is needed because the reflections from the back of the flume and from the floating object would influence the wave height measured. These wave signals were obtained by using the phase shift of the waves in between the wave gauges. With a known distance between the sensors (given in Table 4.1) a single wave signal can be reconstructed from four time series of surface elevation using the phase difference. For the regular wave analysis, the leading order harmonic coefficients are determined by least squares fit of the amplitudes as described in the appendix of Jacobsen et al. (2011) [29]. For irregular wave analysis, the non-linear ELA separation method is used [19]. Both methods are briefly explained in Appendix J.

Regular wave parameters
In the regular wave tests, the same wave signal is created over the whole duration of the test. Therefore, when averaging over time, a single set of wave heights that correspond to the four wave signals H_{p1}, H_{r1}, H_{p2} and H_{r2} (Figure 4.3) describes the full behaviour of the equilibrium wave environment. With these wave heights, an analysis can be done on the influence of the floating model on the waves. To begin, the transmission coefficient, defined before in equation (1.1), indicates what portion of the waves is transmitted through the structure. For the regular wave tests, it is computed by

$$K_t = \frac{H_{p2}}{H_{p1}} \tag{4.1}$$

For reflection, one would wish to define a reflection coefficient (1.2) that shows the amount of reflection that is caused by the floating structure. However, the backward propagating signal H_{r1} is largely influenced by reflections from the back of the flume, as the wave dampener still reflects about one third. The objective is now to filter out the backward propagating wave signal which was caused by the system, and not by the reflections from the back of the flume.

In the diagram in Figure 4.4, the various measured wave signals are shown in a schematic way. The measured wave heights H_{p1}, H_{r1}, H_{p2} and H_{r2} (as introduced above, Figure 4.3) are split up into different physical processes present in the flume.

Figure 4.4: Schematic diagram of the wave heights measured in the Scheldt flume tests.

In Figure 4.4, the wave paddle is positioned on the left. It creates forward propagating waves, which are shown in with the arrow *a*. These waves are part of the measured wave signal H_{p1} and are therefore included in its dashed box. When these waves propagate further and encounter the floating object, they can partially reflect from the front of the structure. The part of *a* which is reflected back to the wave paddle is shown by *b*. The remaining part of the waves propagates through the floating structure, and will be measured as a transmitted wave *d* by the second set of wave gauges once it arrives there.

Along the way, dissipation by friction from the structure might take place, thus *b* and *d* do not have to add up to the value of *a*. The arrow *d* thus displays the portion of initial waves *a* which is transmitted by the system. It is part of the wave height H_{p2}, as it is propagating in positive x-direction at location 2 (behind the structure).

Once these waves reach the end of the flume, they will be dampened out by the wave dampener. However, still around 30% of the wave signal will be reflected from the back of the flume.[3] The part of *d* which is reflected is denoted by *f*.

If the reflections from the wave dampener *f* are nonzero and propagate in opposite direction through the flume, these waves influence the wave heights at both positions in the flume. This is why the filtering methods are used to split the waves that propagate in opposite directions. Because *f* propagates in negative x-direction, back to the wave paddle, it is part of the filtered H_{r2} wave height. When it propagates further, the same physical processes that wave *a* encountered will happen to wave *f* as well, in opposite direction. It is assumed that the reflection from the object as well as the dissipation and thus transmission are independent of propagation direction. Thus, *f* will be split up into a reflected part (caused by the object) giving signal *e* and a transmitted part *c*.

Finally, the reflection parameter is now defined as the proportion of incoming waves that are being reflected by the structure

$$K_r = \frac{H_b}{H_a} \tag{4.2}$$

where H_b is the wave height of the reflections from the structure (denoted by *b* in Figure 4.4) and H_a the incident wave height (denoted by *a* in Figure 4.4).

The backward propagating signal in front of the system H_{r1} includes both the reflection from the object *b*, as well as the transmitted reflection from the end of the flume *c*. Therefore, H_b does not immediately

---

[3] The wave dampener at the end of the flume was not an active wave dampener but an artificial beach where the waves would break.

follow from the (filtered) wave height measurements. A system of equations is set up to find this unknown parameter *b* or *b/a*.

The system of equations to solve for K_r in the regular wave tests, equation (4.2), is defined as follows

$$a = H_{p1} \tag{4.3}$$

$$b + c = H_{r1} \tag{4.4}$$

$$d + e = H_{p2} \tag{4.5}$$

$$f = H_{r2} \tag{4.6}$$

$$\frac{b}{a} = \frac{e}{f} \tag{4.7}$$

$$\frac{d}{a} = \frac{c}{f} \tag{4.8}$$

The first equations (4.3) - (4.6) are simply the definitions of the filtered wave heights, where the assumptions are made that *g*=*h*=0. This means that the reflections at the front of the flume are assumed to be dampened out completely by the ARC of the wave paddle (*g*=0), and only first order reflections from the back of the flume are included (*h*=0). Equation (4.7) follows from the assumption that the reflection from the object is symmetric; the proportion of incoming waves which is reflected from the object is the same for waves propagating in both directions. This assumption is supported by the fact that the floating object and its mooring were completely symmetric. Equation (4.8) is based on a similar reasoning, namely that the proportion of a wave that is being transmitted through the structure is symmetric.

This system of 6 equations for the 6 unknowns *a* - *f* can be solved. The expression that follows for the transmission coefficient in terms of the measured wave signals H_{p1} - H_{r2} is

$$K_r = \frac{H_{r1}H_{p1} - H_{p2}H_{r2}}{H_{p1}^2 - H_{r2}^2} \tag{4.9}$$

The assumptions that form the basis of these equations are:

- No reflection from wave paddle
- Only first order reflection from back of the flume
- Reflection from the system is exactly the same at both ends of the floating object
- Transmission through the system is exactly the same for wave propagation in both directions

The validity of these assumptions can be doubted, especially omitting the higher order reflections from the wave dampener end of the flume while it is known that reflection is around 30%. These points of discussion are explained further in the discussion Chapter 6.

Irregular wave analysis
The irregular wave analysis starts with the comparison of the variance density spectra for the incident and transmitted waves. After that, the total wave energy transmission is studied by means of a global transmission coefficient. The final, frequency dependent, spectral transmission coefficient is defined by splitting up the spectrum into frequency intervals. Each step will be explained shortly in this section.

Variance density spectra
As explained in section 4.1.2, the 8 time series measurements are transformed into a forward and backward wave signal for each location in the flume. This analysis was done using the ELA separation method [3], explained in Appendix J.2. From the froward propagating time signals, H_{p1} and H_{p2}, the variance density spectra are obtained using a Fast Fourier Transform.[4] Thus for each test, an incident

---

[4] The analysis to obtain the variance density spectra were done by Deltares. I received the variance density spectra and the measurement time series, and worked with the former.

$(p1)$ and a transmitted $(p2)$ variance density spectrum are determined, which will be denoted by E_i and E_t respectively.

The variance density spectra were smoothened using 5-point triangular smoothing filter[5], which conserves area under the curve, which represents energy.

Energy density spectra and total energy
To see what proportion of energy is being transmitted by the floating object in North Sea test conditions, we look into the differences in the wave energy density spectra. This spectrum is obtained by multiplication of variance density spectrum with the additional factor $g\rho$ (see section 2.1.1, equation (2.3)). Therefore, the shape of the energy density curve is the same as the variance density curves. The energy density curve is integrated over frequency to compute the area under the energy density curve, which gives the total energy per unit water surface E in [kg/s^2], by equation (2.4). To recall,

$$\mathrm{E} = \int_0^\infty E_{energy}(f)df = \int_0^\infty g\rho E_{var}(f)df$$

The integration of the variance density curve is done numerically with the trapezoidal method.

Global transmission coefficient
From the values for the total energy per square meter water surface, a global transmission coefficient can be defined in the following manner

$$\bar{K}_{tn_{FL}} = \left(\frac{\mathrm{E}_{t,n_{FL}}}{\mathrm{E}_{i,n_{FL}}}\right)^{0.5} \tag{4.11}$$

where $\mathrm{E}_{t,n_{FL}}$ is the transmitted energy per surface area for the test with n_{FL} floater arrays, and $\mathrm{E}_{i,n_{FL}}$ is the same for the incident energy per suface area. The square root is taken in this definition as transmission coefficient is defined as ratio between wave heights (equation (1.1)), and the relation between wave energy and wave height is $\mathrm{E} \propto H^2$. $\bar{K}_t^2$ gives the percentage of wave energy that is transmitted.

Frequency dependent transmission coefficient
To investigate how the wave energy transmission depends on the frequency, the spectral transmission coefficient is defined over a number of frequency intervals. Its definition is shown in equation (4.12). This equation is similar to the global transmission coefficient, equation (4.11), but for a frequency interval j defined as $[f_{j-1}, f_j]$ for $j \in \{1, 2, ..., n_{bins}\}$. This analysis allows for comparison between the regular and irregular wave transmission results.

The spectral transmission coefficient K_t is defined for each interval j with a system setup of n_{FL} floater arrays

$$K_t(j, n_{FL}) = \left(\frac{\int_{f_{j-1}}^{f_j} \rho g E_{t,n_{FL}}(f)df}{\int_{f_{j-1}}^{f_j} \rho g E_{i,n_{FL}}(f)df}\right)^{0.5} = \left(\frac{\left[\mathrm{E}_{t,n_{FL}}\right]_j}{\left[\mathrm{E}_{i,n_{FL}}\right]_j}\right)^{0.5} \tag{4.12}$$

where f_j is the upper bound of the frequency interval, f_{j-1} is the lower bound of the frequency interval, $E_{t,n_{FL}}(f)$ is the variance density of the transmitted wave signal for the setup with n_{FL} floater arrays and $E_{i,n_{FL}}(f)$ is the same for the incident wave signal. In the second part of this equation, the total transmitted energy per unit ocean surface area in frequency interval j is denoted by $\left[\mathrm{E}_{t,n_{FL}}\right]_j$, the total incident energy by $\left[\mathrm{E}_{i,n_{FL}}\right]_j$.

The integration had to be done before the division because the variance density spectra of the incident and transmitted wave signal were not given for exactly the same frequencies.

---

[5] A triangular smoothing filter is a way to smoothen a curve while keeping the area under the curve constant. The implemented weighted smoothing function is as follows

$$s_j = \frac{y_{j-2} + 2y_{j-1} + 3y_j + 2y_{j+1} + y_{j+2}}{9} \tag{4.10}$$

4.2. Results

In this section, the results of the Scheldt flume model tests will be discussed. The time series measurements of the wave gauges were used to compute transmission and reflection coefficients for each regular wave test. The irregular wave test results were used to evaluate the variance density spectra and a frequency dependent transmission coefficient as well.

All results will be presented on full scale dimensions, unless stated otherwise. The regular wave test results will be discussed in section 4.2.1, the irregular wave tests in section 4.2.2.

4.2.1. Regular wave test results

In this section, the results from the regular wave tests will be presented. This constitutes of an analysis of the wave transmission and wave reflection in presence of the floating multi-body solar structure. The dependence of these parameters on the wavelength, wave height and system configuration are analysed one by one. Lastly, some remarks can be made on the influence of dissipation on wave attenuation.

Transmission

The transmission coefficient K_t for regular waves, equation (4.1), was computed for every regular wave test. The value of K_t varied strongly depending on the wave condition, as theoretically expected from floating breakwater literature (see section 3.2).

When the floating structure was present, 87% of the tests still showed a high transmission of $K_t > 0.9$. This gives a first indication that the structure acts as a wave follower and had little impact on the wave environment. Only the two tests with the highest frequency and shortest wavelengths within the testing programme (tests 15 and 32: see Table I.1) showed $K_t < 0.8$. To investigate the dependence of K_t on the wave properties further, the dependence on wavelength λ (and thus wave frequency f), wave height H and the number of floater arrays n_{FL} are considered below.

Wavelength dependence

To isolate the relation between transmission and wavelength, the tests with a constant wave height of $H = 1$ m (full scale) are considered. For these tests, the transmission coefficients are plotted in Figure 4.5 as a function of the dimensionless wavelength λ/L_f. Here, L_f the length of a rigid floater along the propagation direction. $L_f = 12$ m on offshore scale, and λ follows from the nonlinear dispersion relation (2.17).

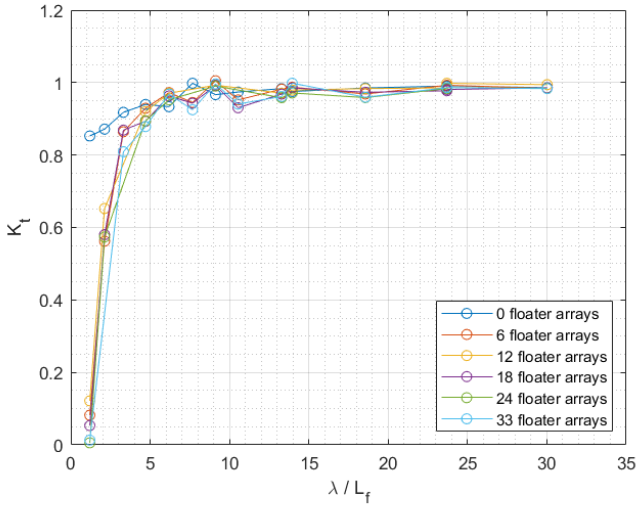

Figure 4.5: Transmission coefficient defined as in equation (4.1), as a function of the dimensionless wavelength λ/L_f (wavelength over floater length). Plotted for regular waves with constant wave height of $H = 1$ m on offshore scale, for different system sizes n_{FL}.

From this plot, it can be seen that for longer wavelengths, $\lambda/L_f \geq 3$, the transmission is almost 1 for all system configurations. The waves are thus able to pass through underneath the structure, and are not affected by the floating solar platforms. When the wavelength is long in comparison to the rigid parts of the structure ($\lambda/L_f > 3$), the system can follow along with the wave. This creates a motion where the floating multi-body structure moves as a 'patchwork' of blocks over the wave.

For the shorter wavelengths, $\lambda/L_f \leq 2$, there is a clear difference between the calibration test (shown in blue for the 0 floater arrays) and the other tests where the floating system was present in the flume. This confirms the hypothesis and rule of thumb introduced in Chapter 3, section 3.2, which states that the transmission is low for wavelengths shorter than $2L_f$ because of opposite forces acting on the rigid body. For $\lambda/L_f < 2$, the transmission could be a uniformly increasing function of λ/L_f. However, the amount of measurement points to support this possible relation is only 3 per configuration. All test showed a transmission of almost 0 for the test with $\lambda = 14$ m, $\lambda/L_f = 1.17$.

Notice the presence of fluctuations and variations in Figure 4.5 (and later in Figure 4.6 as well) in the the value of K_t over the desired parameter. These fluctuations are in the order of magnitude of 0.05, and will not be studied in detail. It could be that there are actual differences in physical behaviour between the tests that lead to a different transmission, such as a specified oscillation mode. However, it could also be that these fluctuations fit in the uncertainty interval around the transmission values or are caused by three dimensional effects. Therefore, conclusions for the regular wave tests are focused on the trends of the transmission, rather than on these smaller scale variations.

Wave height dependence
The dependence of the wave transmission on the wave height was tested by varying the wave height over the tests while leaving the wave period (and thus wavelength) constant. These tests showed no clear wave height dependence. Both for the regular tests with constant period $T = 7$ s ($\lambda/L_f = 6.2$) and the ones with $T = 10$ s ($\lambda/L_f = 10.5$) on full scale, the values of the transmission coefficient differed minimally between the tests. The transmission coefficients K_t were plotted over the dimensionless wave height H/H_f, which is defined as wave height over floater height. On full scale, the floater height was $H_f = 0.3$ m. The plots are shown in Figure 4.6.

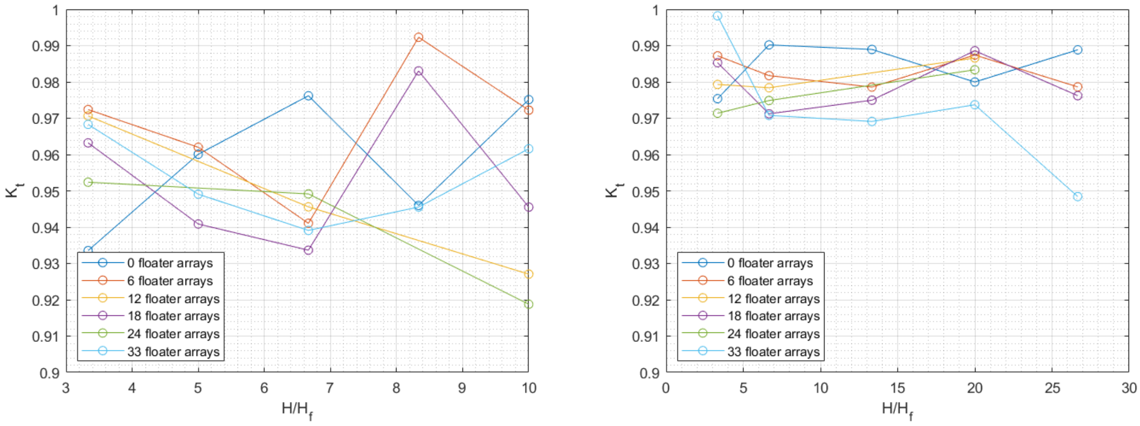

(a) Constant wave period $T = 7$ s

(b) Constant wave period $T = 10$ s

Figure 4.6: Transmission coefficient defined as in equation (4.1), as a function of the dimensionless waveheight H/H_f (wave height over floater height). Plotted for regular wave tests with constant wave period T, for different system sizes n_{FL}.

Note the scale of the transmission coefficient axis is in between $K_t \in [0.9, 1]$. Thus, the transmission was almost constant when the wave height was varied. The difference between the tests with various wave heights was maximally 5% for a certain number of floater arrays. Moreover, this was even the case for the calibration test as well. Therefore, any difference in transmission due to the changing wave height could be smaller than the impact of side effects such as flume friction (which were present in the calibration test).

To look more closely into wave height dependence, it might be better to look at tests with a (constant) period in the range where the transmission is actually lowered by the system. For the wave conditions tested with differing wave height, the transmission was almost full. Therefore, the influence of higher waves is maybe small because there is no impact of the system at all. In the irregular wave tests, steepness or wave height dependence can be studied by looking at the tests which had the same peak period but a different significant wave height. These results are discussed in section 4.2.2. //

System size dependence

All tests were repeated for the different configurations of floater arrays n_{FL}. In general, it was often true that the largest system configuration of 33×8 floaters had the lowest transmission value K_t per test. However, the difference in transmission values between these various system configurations is small.

In Figure 4.5, the lines that correspond with different n_{FL} lie relatively close together. This indicates that influence of the system size is limited, especially in comparison with the influence of the incident wavelength or wave frequency. The dependence on the wavelength is clearly much more dominant than the dependence on the number of floaters present. For the smallest wavelength where $K_t \rightarrow 0$, the difference between the floater configurations was largest (in the order of 0.1 or 10%).

In Figure 4.6, the difference in transmission for a different the number of floater arrays present $n_{FL} \in \{6, 12, 18, 24, 33\}$ was maximally 0.05. This difference is within the margins of the fluctuations between the tests and might therefore might lie within the uncertainty range of the results. Furthermore, when transmission is almost 1 it did also happen that smaller system configurations show lower transmission than the largest system configuration with $n_{FL} = 33$. An example can be seen in the values for K_t when $H/H_f \approx 3$ in Figure 4.6b (which corresponds to test-ID 6).//

In conclusion, the number of floating platforms included in the regular wave tests did not have a large impact on the wave transmission.

Reflection

The reflection coefficient K_r, as defined by equation (4.9), is plotted as a function of the dimensionless wavelength λ/L_f in Figure 4.7. Similarly to the transmission in Figure 4.5, only the tests with a constant wave height of $H = 1$ m were taken into account.

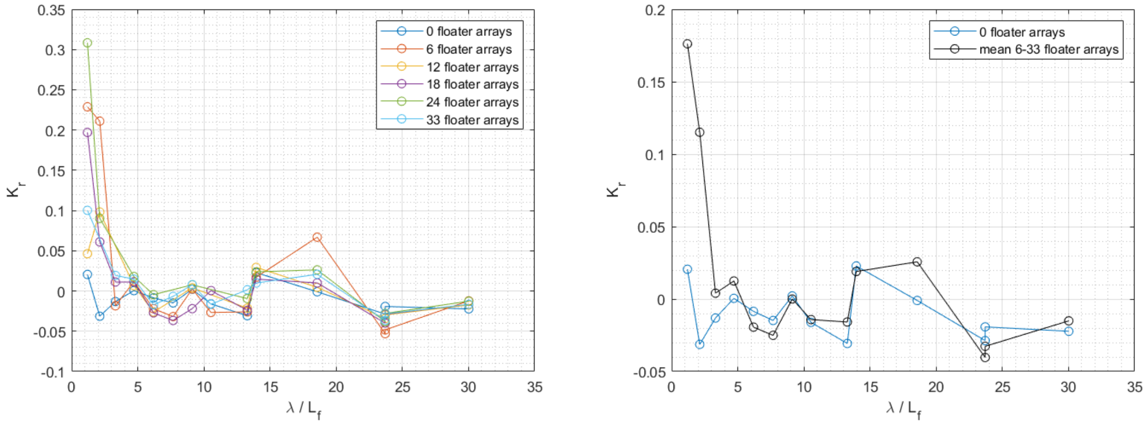

(a) All system sizes $n_{FL} = 0, 6, 12, 18, 25, 33$

(b) Calibration test and average over $n_{FL} = 6, 12, 18, 24, 33$ tests.

Figure 4.7: Reflection coefficient K_r as a function of wavelength over floater length λ/L_f, shown for tests with a different number of floater arrays and the calibration test. Tests had a constant wave height of $H = 1$m full scale.

Figure 4.7 shows that for the large wavelengths, $\lambda/L_f \geq 3$ the reflection is close to 0. That would mean the reflections from the front of the floating solar structure were negligible in relation to the incoming wave height. In this region, the transmission was close to one, $K_t \approx 1$, see Figure 4.5. Furthermore, for $2 < \lambda/L_f < 8$, the lack of transmission could also be partially explained by friction from the sides of the flumes. Therefore, it was indeed expected that the reflection coefficient K_r was relatively small in his range.

For short wavelengths, $\lambda/L_f \leq 2$, reflection increases to values up to $K_r = 0.3$. Transmission was lower in this region, and it can now be concluded that part of the wave energy attenuated has been redirected back in opposite direction. To visualise whether this reflection can explain the lack of transmission fully, the reflection and transmission coefficients have been plotted together with $K_t^2 + K_r^2$ in Figure 4.8.

The uncertainties in this reflection parameter K_r could be high in relation to the result values however, possibly in the order of ± 0.05, which is more than 25%. There are three reasons to be critical about the reflection results shown in Figure 4.7. First, the reflection takes negative values, which cannot be physically explained. Second, the reflection values for the calibration tests show fluctuations around its expected value $K_r = 0$. Third, there are quite some differences between the results for different floater configurations n_{FL} (more than in case of the transmission parameter results K_t). This might be explained by errors in the assumptions for filtering out the reflected waves from the back of the flume, and will be discussed in Chapter 6.

Energy conservation: transmission, reflection and dissipation
The reflection and transmission coefficients, K_r and K_t, have been shown as a function of the dimensionless wavelength λ/L_f in Figures 4.5 and 4.7. To complete the description of wave-structure interaction, the non-linear effects can be collected into a similar dissipation coefficient K_d. From energy conservation in presence of a passive system, it follows that the sum of squared coefficients should add up to one $K_t^2 + K_r^2 + K_d^2 = 1$. Namely, all incident energy had to be either transmitted, redirected (reflected) or dissipated. Therefore, the amount of wave energy dissipation can be derived from the transmission and reflection results.

The analysis should be compensated for the friction by the flume however, which can be found from the calibration tests. When there was no system present, the transmission coefficient was decreased up to $K_{t0} = 0.9$ already for the high-frequent waves, which indicates a significant decrease in wave energy of 19% between the two sets of wave gauges. To include this effect in the energy analysis, an additional parameter $K_{d,f}$ is defined from the transmission results, as $K_{d,f} = \sqrt{1 - K_{t0}^2}$. This dissipation term, which was not caused by the floating structure, has to be considered in the energy conservation equation as well.

Finally, the dissipation effects caused by the system can be defined as the rest term $K_d = \sqrt{1 - K_t^2 - K_r^2 - K_{d,f}^2}$. All coefficients K_t, K_r, $K_{d,f}$ and K_d have been plotted as a function of the wave frequency f in Figure 4.8.

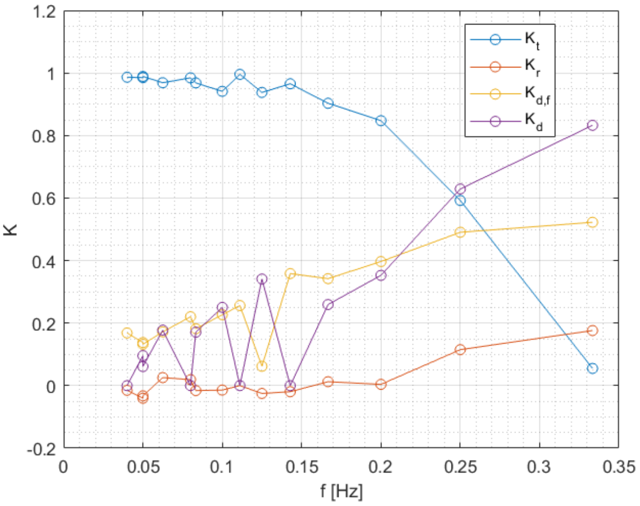

Figure 4.8: Transmission K_t, reflection K_r, flume dissipation $K_{d,f}$ and structure dissipation K_d coefficients, as a function of incident wave frequency f [Hz]. Plotted for regular waves with constant wave height of $H = 1$ m on offshore scale, averaged over the different system size configurations n_{FL}.

From Figure 4.8, it can be observed that the low frequency range $f \leq 0.15$ Hz (which is equal to $\lambda/L_f \geq 6$) shows almost full transmission. For frequencies higher than this value, the transmission coefficient decreased uniformly in f. This decrease in transmission is explained by an increased reflection, an increased flume dissipation as well as an increased dissipation by the floating model. The measured flume dissipation and wave reflection did not add up to the total decrease in wave energy. In fact, the regular wave results indicate that frequency dependent dissipation effects might be dominant over the linear effects in the cause for wave energy attenuation. This is an important conclusion with respect to the model approach as well, as linear wave theory can only describe the redirection of waves and not the dissipation due to higher order effects.

The fluctuations in the dissipation coefficient for $f \leq 0.15$ Hz reflect the high uncertainty of this method, as dissipation is not assumed vary so much over a small difference in incident wave frequency. Any errors in K_r and $K_{d,f}$ will automatically show in the rest term K_d as well. Especially the reflection coefficient is likely to have included errors, which will be discussed in Chapter 6. These could have lead to an underestimation of K_r, which translates to an overestimation of K_d.

Some dissipative effects could indeed be observed during the regular wave tests. Overtopping was visible: the waves splashed over the first arrays of floaters, leaving these wet. Friction effects and turbulent flows might have therefore dissipated some of the incident wave energy. Also, the gaps in between the floaters filled and emptied when waves passed by. Thirdly, the structure itself and the mooring springs were deformed slightly over the test runs.

4.2.2. Irregular wave test results

In this section, the results from the irregular wave tests will be presented. These consist of the analysis of the variance density spectra first, followed by an analysis on energy transmission. Again, especially the frequency dependence of this transmission is looked into. Short observations are presented on the system size and wave height dependence as well.

In Figure 4.9, the variance density spectra $E(f)$ are shown for all irregular wave tests with wave conditions $H_s = 1$ m and $T_p = 5$ s (full scale, corresponds to test-ID 25). Each subfigure shows the spectrum for one of the system configurations, with n_{FL} the number of floater arrays. For each test, the incident and transmitted spectra are plotted. The incident spectrum is the forward propagating spectrum in front of the system, from wave gauges 1-4 (previously denoted as $p1$). The transmitted spectrum is the forward propagating spectrum behind the system, from wave gauges 5-8 (previously denoted as $p2$). The JONSWAP curve at which the test was initialised shows in the plots as well.

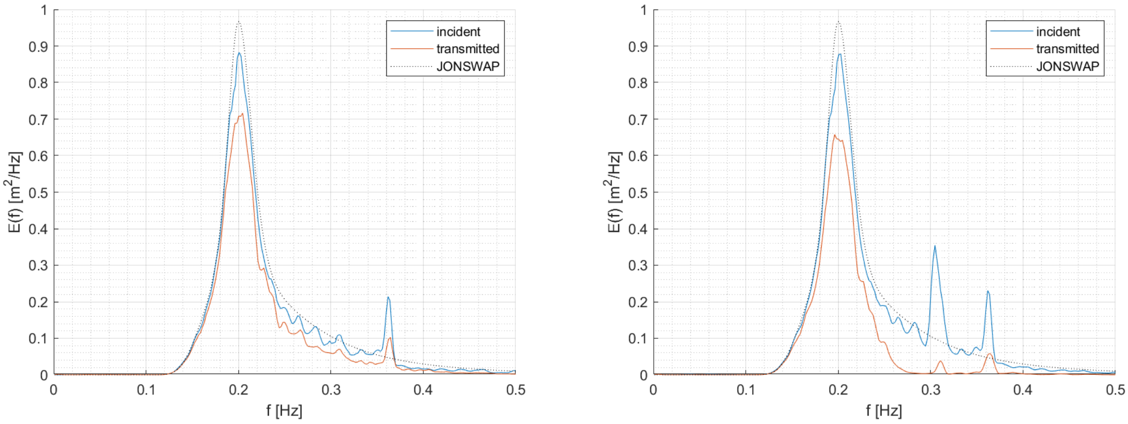

(a) Calibration test $n_{FL} = 0$

(b) System size $n_{FL} = 6$

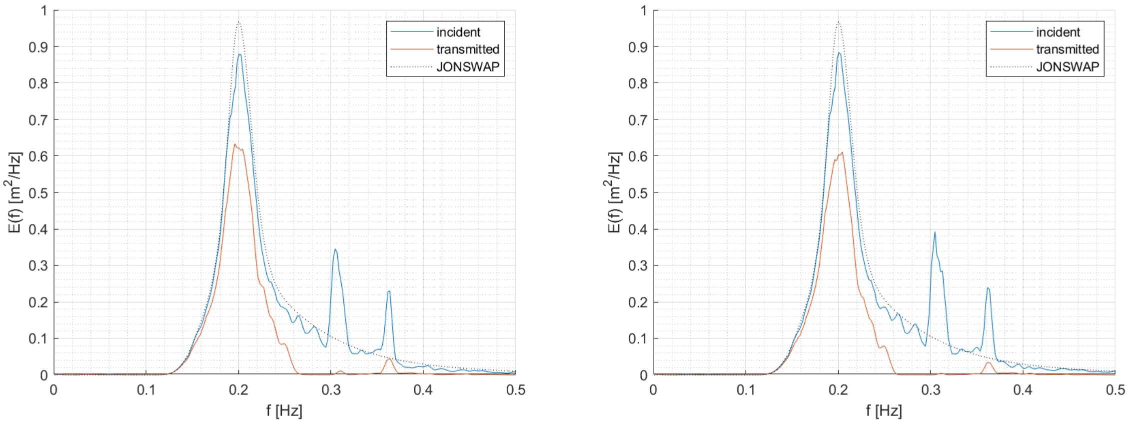

(c) System size $n_{FL} = 12$

(d) System size $n_{FL} = 18$

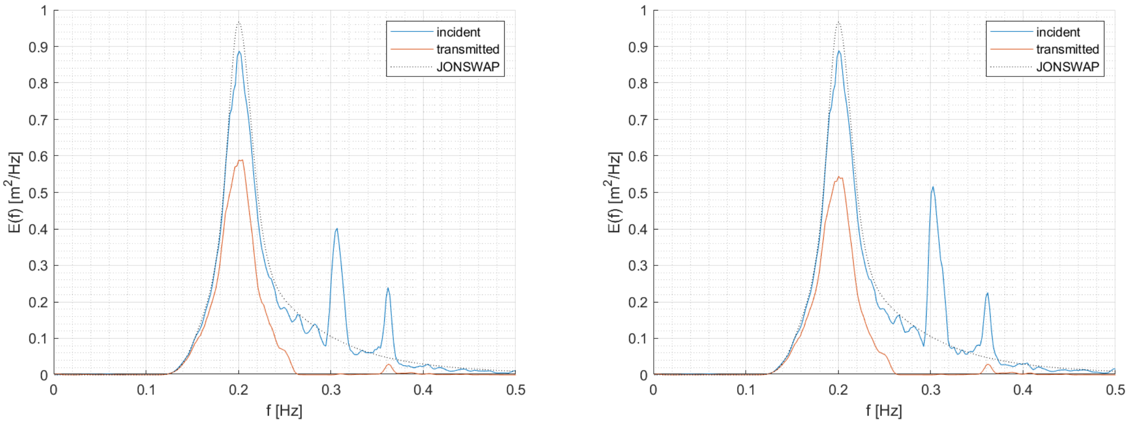

(e) System size $n_{FL} = 24$

(f) Maximum system size $n_{FL} = 33$

Figure 4.9: Smoothed variance density spectra E as a function of the wave frequency f for irregular wave test 25 ($H_s = 1$ m, $T_p = 5$ s at offshore scale). Variance density is plotted for the incident wave spectrum (first 4 wave gauges) and transmitted wave spectrum (last 4 wave gauges), as well as the theoretical JONSWAP spectrum that the test was initialized at.

Note that the spectral plots have been cut off at $f = 0.5$ Hz. Higher frequencies were included as well, but the variance density was low. Observations on the calibration test results in 4.9a will be discussed first, followed by the effects of the floating solar structure by looking at Figures 4.9b-f.

Calibration test

A couple of observations can be made on the calibration test variance density spectrum shown Figure

4.9a. Firstly, the incident and transmitted spectrum do not overlap perfectly. For the peak frequency $f_p = 0.2$ Hz and the higher frequencies the transmitted variance density is a bit lower. Thus, when propagating through the flume the (shorter) waves lose a bit of energy, due to friction by the flume boundaries (which was also observed in the regular wave tests). This could also be the reason for the difference with the intended JONSWAP spectrum for $f \geq 0.2$ Hz.

What can furthermore be observed is the peak at $f = 0.36$ Hz in both the incident and transmitted spectrum, corresponding to a wavelength of $\lambda = 12$ m. This higher variance density was also visible in the (calibration) tests 26 (with a JONSWAP spectrum for $H_s = 2$ m and $T_p = 6$ s). For the other irregular tests, additional peaks in incident (and transmitted) calibration spectra were found at $f = 0.25$ Hz ($\lambda = 25$ m), and $f = 0.29$ Hz ($\lambda = 18$ m). Notice that the additional peaks also show in the tests with floating systems present. Because the higher values in the variance density spectra show up consistently, it is unlikely that this is a random error. The presence of additional incident waves at certain frequencies will be discussed further in Chapter 6.

Effects of floating object

When comparing the tests with a floating solar system present (Figure 4.9b-f) to the calibration test spectrum discussed before (Figure 4.9a), there are differences in the incident wave spectrum as well as the transmitted wave spectrum.

The most important observation is that for higher frequencies ($f > 0.26$ Hz, which translates to $\lambda < 23$ m) the variance density of the transmitted wave is decreased almost fully to 0. Thus, there are very few waves left in the resulting signal for these higher frequencies. The floating system shows to work as a low-pass filter: low frequencies ($f \leq 0.26$ Hz) are not really affected by the object whereas the high frequencies ($f > 0.26$ Hz) are attenuated completely. The transition frequency corresponds to the wavelengths $\lambda/L_f = 2$ m, which is in accordance with the literature (section 3.2) and the regular test results (section 4.2.1).

The only exception in this low-pass filter is the frequency $f = 0.36$ Hz, where $\lambda/L_f = 1$, which shows up in the transmitted spectrum for all tests with varying system size. This peaks is the same as the incident spectrum peak, but is not dampened out entirely whereas the other (peak) frequencies are. Therefore, this could indicate a frequency that fits the system well and might easily be transmitted. However, a system mode which generates waves with $\lambda = L_f$ is not an intuitive motion.

Effects of system size

For same wave spectrum but different system sizes (number of floater arrays), the incident and transmitted variance density spectra look very much alike. The effect of a floating solar system of 6×8 floaters on the waves is similar to the effect of a 33×8 floater system. The conclusion that can be taken is that the wave attenuation does not scale one-to-one with the number of floaters / system size.

The three differences that can be seen when increasing the number of floaters were the following. Firstly, the transmitted variance density for the peak frequency $f_p = 0.2$ Hz decreases further when the system is enlarged. Secondly, the peak in transmitted spectrum at $f = 0.3$ Hz, which is present for $n_{FL} = 6$, fully disappears for the larger system. Thirdly, the peak in the incident wave spectrum at this frequency increases further when more floaters were present.

Different wave conditions

Apart from the irregular wave test 25 ($H_s = 1$ m and $T_p = 5$ s) discussed previously, six other irregular wave conditions were tested. These were four more severe North sea conditions as well as two additional tests with less wave steepness (higher T_p with same H_s). The plots of all variance density spectra obtained from the irregular basin tests are given in Appendix K.

In general, similar behaviour to Figure 4.9 could be seen for the other irregular wave tests. For higher wave frequencies, the spectra are changed visibly whereas the part of the spectrum with the lower frequencies remains unchanged. The difference between incident and transmitted spectra was largest for test 25 (in percentages): a lower proportion of the variance density (or wave energy) was attenuated in the other tests. This is in accordance with expectations because all other irregular tests had their spectra distributed around a lower peak frequency (as the peak wave period was longer). As higher frequencies are affected more, the impact of the floating object is smaller when these are less present in the incident wave spectrum. Additionally, extra peaks in both the incident and transmitted spectra showed to be smaller.

To summarise the observations from the variance density spectra, the most important conclusion is that the higher frequency waves are attenuated by the system whereas the low frequency waves are not influenced as much. For the wavelengths smaller than twice the floater length, the transmitted variance density goes to zero. Only when the wavelength is equal to the floater length, these high frequent waves still show in the transmitted wave spectrum. The effect of enlarging floating solar system to a higher number of floaters was small, as the transmitted spectra were almost identical. For the different wave conditions tested, the overall behaviour showed the same. The percentual difference between the incident and transmitted wave spectrum was smaller for the rougher sea states, thus the impact of the floating solar structure seemed smaller.

Energy transmission

The values for the total energy per unit ocean surface area E are computed for each incident and transmitted wave spectrum, and are given in Table 4.4.

TestID	E_{i0}	E_{i6}	E_{i12}	E_{i18}	E_{i24}	E_{i33}	E_{t0}	E_{t6}	E_{t12}	E_{t18}	E_{t24}	E_{t33}
25	0.56	0.59	0.59	0.61	0.60	0.63	0.44	0.34	0.32	0.30	0.29	0.27
26	2.45	2.57	2.59	2.62	2.62	2.67	2.09	1.84	1.77	1.71	1.67	1.58
27	5.78	5.95	5.90	5.95	5.99	6.00	5.24	5.06	4.98	4.86	4.79	4.69
28	10.06	10.17	10.11	10.18	10.18	10.24	9.28	9.00	8.74	8.63	8.43	8.30
29	15.58	15.65	15.66	15.73	15.76	15.74	14.38	14.12	13.80	13.67	13.46	13.18
30	0.66	0.68	0.67	0.68	0.68	0.68	0.60	0.58	0.57	0.56	0.56	0.55
31	2.55	2.56	2.55	2.56	2.57	2.58	2.38	2.34	2.31	2.28	2.28	2.26

Table 4.4: Total wave energy per m^2 water surface, for the irregular wave tests. Each test-ID stands for a wave condition tested as defined in Table I.2. The energy values for the incident wave field with n_{FL} floater arrays present are shown as $\mathrm{E}_{in_{FL}}$, and for the transmitted wave field as $\mathrm{E}_{tn_{FL}}$. The energy per unit surface is given in [kg/s^2]. Note that these values have been derived from the forward propagating wave spectrum, so all reflection propagating in opposite direction has been filtered out.

For all irregular wave tests, the transmitted wave energy $\mathrm{E}_{tn_{FL}}$ is lower than the incident wave energy $\mathrm{E}_{in_{FL}}$. Therefore, we can again conclude that the waves are attenuated, even in the calibration tests. Also, for all tests there is a (positive) difference between the incident wave energy for the test with a floating object present $\mathrm{E}_{in_{FL}}$ for $n_{FL} = 6, 12, 18, 24, 33$ and the incident wave energy for the calibration tests E_{i0}. This means that there is more incident wave energy for the tests with a system present, whereas the wave paddle was sending out waves with exactly the same steering file. This phenomenon is observed previously and will be discussed in Chapter 6.

The values of this global transmission coefficient, see equation (4.11), for all irregular wave tests are shown in Table 4.5. The square of this transmission coefficient gives the amount of wave energy that is being transmitted.[6] Clearly, the transmission percentage for the total wave energy was lowest for the first two irregular wave tests. These were tests with lower (significant) wave heights and shorter (peak) wave periods ($H_s = 1$ m, $T_p = 5$ s and $H_s = 2$ m, $T_p = 6$ s for test 25 and 26 respectively). This conclusion was also drawn from the variance density spectra, and was explained by the fact that these tests had more waves in the region where wave attenuation is present ($\lambda_f < 2$).

---

[6] For example, with the maximum system and North sea wave conditions of test 25 ($H_s = 1$ m, $T_p = 5$ s), a calculation of $1 - \bar{K}_{t33}^2$ gives that 57% of the total wave energy is attenuated. Note that this includes approximately 21% of wave energy dissipation by friction in the flume, $1 - \bar{K}_{t0}^2$.

TestID	$\bar{K}_{t0}$	$\bar{K}_{t6}$	$\bar{K}_{t12}$	$\bar{K}_{t18}$	$\bar{K}_{t24}$	$\bar{K}_{t33}$
25	0.89	0.76	0.74	0.71	0.69	0.65
26	0.92	0.85	0.83	0.81	0.80	0.77
27	0.95	0.92	0.92	0.90	0.89	0.88
28	0.96	0.94	0.93	0.92	0.91	0.90
29	0.96	0.95	0.94	0.93	0.92	0.91
30	0.95	0.93	0.92	0.91	0.91	0.89
31	0.97	0.96	0.95	0.94	0.94	0.94

Table 4.5: Global transmission coefficients $\bar{K}_{tn_{FL}}$ for each irregular wave test with n_{FL} floater arrays present. Defined from the total transmitted over total incident total wave energy shown in Table 4.4. Each test-ID stands for a wave condition tested as defined in Table I.2.

For the tests where transmission was lowest, the differences between the various number of floater arrays were also largest. The differences between $\bar{K}_{t6}$ and $\bar{K}_{t33}$ are largest for tests 25 and 26. It is intuitive that if the system of 6 floater arrays has a nearly negligible effect on the waves, enlarging the system will not change the results as much. On the other hand, if the transmission is significantly lower because of the small system, the dependence on the number of floaters is higher.

The exact dependence of the global transmission coefficient on the system size is shown in Figure 4.10.

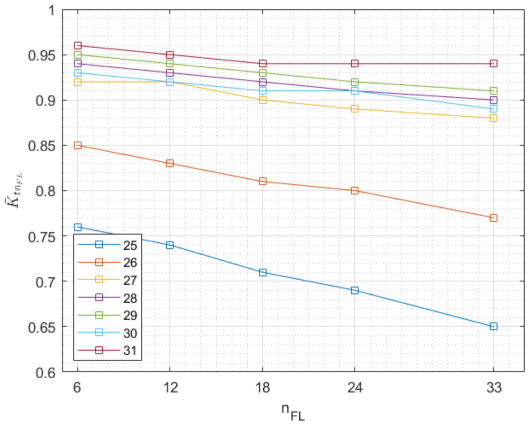

Figure 4.10: Global transmission coefficient $\bar{K}_{tn_{FL}}$ as a function of the number of floater arrays present n_{FL} shown for all seven irregular wave tests 25-31 (with wave conditions shown in I.1).

In this plot of the global transmission coefficients (Table 4.5), it can be seen that the transmission of the total wave energy is linearly dependent on the number of floaters. However, the slope of this relation differs per wave condition and is maximally 0.004. If the impact on the waves is large (test 25), the transmission is more dependent on the number of floaters.

To investigate further whether the difference in the global transmission coefficient among the irregular tests was indeed caused by the difference in wave periods or frequencies that were present in the spectrum, the frequency dependence of the energy transmission is discussed in the next section.

Frequency dependence

In Figure 4.11, the transmission coefficients as defined by equation (4.12) are plotted against the frequency. The transmission coefficient for the irregular calibration tests are given in subfigure (a) and the irregular tests with the largest floating system present (33×8) in subfigure (b). The number of bins taken for this computation was $n_{bins} = 60$ distributed over the interval $f \in [0.1, 0.3]$ Hz. The transmission coefficient plots for the other floating system configurations ($n_{FL} = 6, 12, 18, 24$) are included in Appendix L.

Only the frequency interval between $f = 0.1$ Hz and $f = 0.3$ Hz is looked at, as these are the values for which the incident variance density or energy density values were not too close to zero for the irregular tests 25-31. In other words, these are the frequencies where the energy was present. When one would look at the transmission coefficient over a larger frequency interval, the K_t values differ a lot per test and can lie far from 1 (e.g. $K_t = 3$). This can be explained by the small values of $E_i(f) \approx 0$ for $f > 0.3$ Hz. From the definition of the transmission coefficient it follows that one will then divide by a small number, which gives rise to large errors. In this part of the spectra there is not that much energy present; the number of waves with these frequencies were limited and thus a large error can occur in computation based on these values.

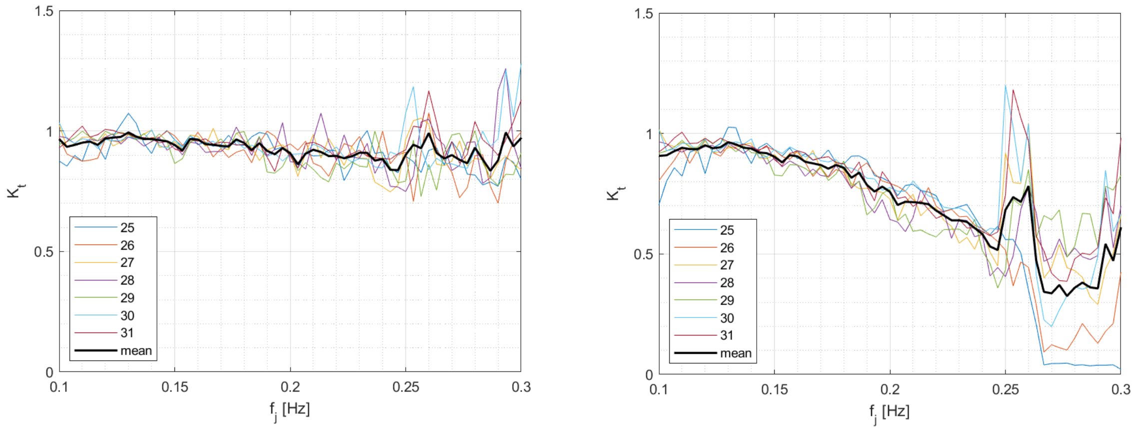

(a) Calibration tests, $n_{FL} = 0$

(b) Maximum system size, $n_{FL} = 33$

Figure 4.11: Transmission coefficient K_t computed in each frequency interval with upper bound f_j for the irregular wave tests. Values for each irregular wave test are shown, with test-IDs 25-31 corresponding to the wave conditions given in Table I.2. The mean over these transmission values is shown in black.

In Figure 4.11a, the transmission coefficient is relatively close to $K_t = 1$ for all frequencies. When no floating object was present in the flume to influence the incoming wave spectrum, it was expected that all wave energy is being transmitted.

In Figure 4.11b, the transmission curve shows for the tests with the floating model present. It can be concluded that for the low frequencies, thus large wavelengths, the transmission is close to one as well; the system does not decrease wave energy. For the higher frequencies, as discussed before, the transmission does go down.

The peak in transmission around $f = 0.25$ Hz ($\lambda = 25$ m) is caused by additional peaks in the transmitted energy spectrum around this frequency. This increased transmission can be seen in all spectra of Appendix K as an exception to the high frequency wave attenuation. With a corresponding wavelength of $\lambda = 25$ m, this frequency matches the system motion of 2 floaters that fit into a single wavelength. This movement was also observed in regular wave test 15, and can be visualised as in Figure 4.12. When the wave height and thus the angle between the floaters is small, the two floaters will fit into one wavelength. With this motion, the full system of connected rigid floating bodies is able to follow the wave well. Therefore, the wave transmission is not reduced to 0.

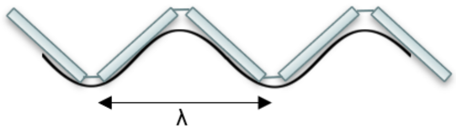

Figure 4.12: Schematic diagram of the movement of the floaters when $\lambda \approx 2L_f$.

In Figure 4.11, the mean value shows the average over all 7 irregular wave tests that were done. The spread of the other lines plotted gives an insight in the uncertainty present in this average value. When the spread between the other lines is large, it could be that either something physically different happens for the various wave conditions, or there is a larger uncertainty in the the computation of the transmission coefficient. The latter option is likely to happen for the larger frequency values; for some wave tests the spectra did not have much incoming wave energy for frequencies larger than 0.2 Hz. This is also why, even in the calibration test, the spread around the average line is more than 10%.

For the higher frequencies, more confidence can lay in the transmission information of test 25 and 26, as these tests included more waves with these frequencies in incident spectrum [7]. The same reasoning holds for test 28 - 31 for the lower frequencies, as these tests included more waves with these longer wavelengths. Taking this into account, the transmission coefficient is likely to be closer to 0 for the frequencies $f > 0.26$ Hz, as the transmitted wave energy is close to 0 for tests 25 and 26, where incident wave energy in this part of the spectrum was nonzero. Taking a weighted average per frequency, with respect to the amount of incident energy present in the spectrum for the respective test, could be an improvement in further analysis.

System size dependence
For the other system configurations ($n_{FL} = 6, 12, 18, 24$), the plots of the transmission coefficient over the frequency are very similar to Figure 4.11b where $n_{FL} = 33$. These plots have been included in Appendix L, Figure L.1. The full length of the system thus does not have that much impact on the shape of the transmission curve. This indicates that the influence of only 6 floater arrays is comparable to the influence of systems with a larger number of floaters connected together, for this (2D) irregular wave test setup. This is in agreement with the results presented for the regular wave tests.

Wave height dependence
A short note on the comparison between tests 27 and 30 (both $T_p = 8$ s) or tests 29 and 31 (both $T_p = 10$ s) can be made, which have the same peak period but different wave heights. There was not really an observable difference in the transmission of waves between these tests. The global transmission coefficients were approximately the same (see Table 4.5), and the transmission curves in Figure 4.11 lie close together. Therefore, the influence of the significant wave height of the spectrum seems limited.

4.2.3. Comparison to regular and irregular wave test results

From the regular wave test results shown in section 4.2.1, it could be concluded that the wave transmission was mainly dependent on the wavelength or frequency of the waves. This dependence was also studied in section 4.2.2 for the irregular wave results. To make a comparison between these results, Figure 4.7 is adapted to show the transmission coefficient K_t as a function of the frequency f, similarly to the plots in Figure 4.11 and Figure L.1 in the appendix. That way, a comparison could be made whether the irregular wave tests indeed showed the same physical behaviour as the regular wave tests. The irregular lines show the transmission coefficient for the calibration test, $n_{FL} = 0$, and the test with maximum system size, $n_{FL} = 33$, averaged over the 7 spectral tests that were carried out. The regular lines show the transmission coefficient for the various system sizes that were tested. Each point thus represents a regular wave test with $H = 1$ m and the frequency $f = 1/T$.

---

[7] See total overview of variance density plots in Appendix K for the spread of the variance density spectra over the frequency.

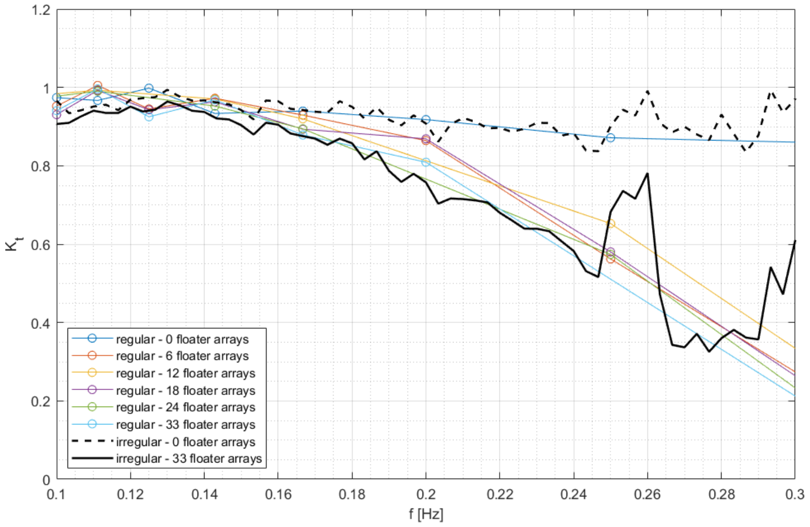

Figure 4.13: Transmission coefficient K_t as a function of frequency f at offshore scale. Both regular and irregular wave test results are shown.

In this plot, the transmission coefficients for the regular and irregular wave tests are shown to overlap quite well. The calibration test stays close to one, whereas the tests with floaters present show a decrease in transmission when the frequency is higher. The only difference between the regular and spectral transmission shows for the frequency $f = 0.2$ Hz; the basin test results show a higher transmission than the spectral results.

In both regular and irregular results presented, the dependency on the wave height and the number of floaters was small with respect to the influence of wavelength or frequency.

4.3. Result summary

The basin tests showed that the effect of the floating solar structure ranges from almost full transmission to almost full attenuation. The wave attenuation was highly dependent on the wave frequency f and thus the wavelength λ.

From the regular and the irregular wave tests, it was shown that there is almost full transmission for the long wavelengths and low wave frequencies. From a wavelength larger than six times the floater length onwards, $\lambda \geq 6L_f$ the transmission with the floating solar model present was almost the same as the transmission in the calibration tests. For shorter wavelengths and higher frequencies, the transmission decreased linearly in f. In the tests where the highest frequencies were present, where $\lambda < 2L_f$, the transmission even became close to 0, which meant the waves are fully blocked by the system. The floating solar system thus acts as a low pass filter: it lets the waves of low frequency pass through (or actually underneath), whereas the waves with higher frequency are being attenuated by the structure. This is in accordance with the literature findings on floating breakwaters.

The only exception for the decrease in transmission for wavelengths smaller than twice the floater length showed for a frequency of $f = 0.25$ Hz, $T = 4$ s, $\lambda = 25$ m (on offshore scale). In the irregular wave tests, the transmitted forward propagating wave spectra showed a peak for this frequency. This can be explained by the movement of the floaters; the rigid bodies can follow the waves quite well when two floaters fit into one wavelength exactly.

In the regular wave tests where the incident wave height was varied and the wave period was kept constant, the transmission coefficient showed to be nearly constant when the wave height was varied. This was also true a comparison was made between the irregular wave tests which had the same peak period but a different significant wave height. However, all these tests were done in the frequency range where the transmission was close to 1 and the system did not have as much effect on the waves. Therefore, looking into wave height dependence in a range where the waves are attenuated more could give more information on the wave height dependence and might give rise to a different conclusion.

The transmission coefficient showed to depend on the number of floater arrays slightly. In both the regular and the irregular tests, the different system configurations showed to have similar transmission percentages. The transmission curves for the regular wave tests overlapped quite well, and the variance or energy density spectra for the irregular wave tests looked very much alike. In general, when looking at a frequency regime where waves were attenuated, the largest system size did show the most wave attenuation. The global transmission coefficient, defined as the square root of the total transmitted over the total incident wave energy, showed to be linearly dependent on the system size, with a slope that depended on the amount of attenuation. For a test where the waves were attenuated more, the transmission decreased more as a function of the number of floater arrays.

The reflection analysis showed that the reflections from the floating object did increase with the wave frequency f, but could not explain the decrease transmitted of wave energy. Moreover, frequency dependent dissipation effects might be dominant over the linear effects in the cause for wave energy attenuation. This is an important conclusion with respect to the model approach as well, as linear wave theory can only describe the redirection of waves and not the dissipation due to higher order effects. The filtering method to obtain the reflected wave height could be questioned however, therefore possible underestimation of the reflection could have lead to an overestimation of dissipation contributions.

5

Numerical diffraction model

This chapter will discuss the numerical diffraction model and its scattering solution. The theory section 5.1 will explain how a boundary element method diffraction model works in general and gives a short introduction of Capytaine, which is the model that was used. Also, it explains how the surface elevation, transmission coefficient and reflection coefficient can be obtained from the usual Capytaine output. After that, section 5.2 will state the model method, followed by the results in section 5.3. Lastly, a summary of the obtained results is given in section 5.4.

5.1. Theory

5.1.1. Panel method

The mathematical description of wave-structure interaction in linear potential theory consists of the scattering and radiation problem, as explained in sections 2.4.1 and 2.4.2. The Laplace equation, with the appropriate boundary conditions, can be solved numerically using an integral, boundary element method approach, also known as the panel method. In general, a boundary element method approximates the solution of a partial differential equation by looking at the solution on the boundary, found from an integral equation using Green's functions. This surface boundary solution can then be used to find the solution inside the domain [33].

The boundary value problem for $\phi(x, y, z)$ introduced in section 2.4 can be rewritten into an integral equation problem using Green's second identity [37]. This can be done for the diffracted velocity potential ϕ_D and for the radiation potential in each degree of freedom, $\phi_{R,j}$ for $j \in \{1, 2, ..., 6\}$. Remember that the incident wave velocity potential ϕ_I is a given function, which is equal to (2.15).[1] Because this integral equation has to be solved on the wetted surface of an object only, the numerical domain changes from an (infinite) three dimensional water volume to a two dimensional object surface. The approach to convert the boundary value problem into a the integral equation for the velocity potential is explained in more detail in for example [36, 39, 50, 58].

These integral equations can be solved analytically in some cases, for example diffraction around an infinite cylinder [40] or the wave interaction with a rectangular long floating structure over a horizontal seabed [58]. The numerical approach to solve the diffraction and radiation problem in integral form uses the 3D panel method, with the source-sink technique [15, 30, 36].

The velocity potential ϕ at a point (x, y, z) on the mean wetted surface of the object S_B can be represented by a continuous distribution of single sources on the body surface [30, 34]. This gives

$$\phi(x, y, z) = \frac{1}{4\pi} \int_{S_B} \sigma(\hat{x}, \hat{y}, \hat{z}) \cdot G(x, y, z, \hat{x}, \hat{y}, \hat{z}) dS \qquad \text{for } (x, y, z) \text{ on } S_B \qquad (5.1)$$

---

[1] The exact definition of for example the propagation direction might differ per model, but Capytaine uses exactly this expression in case the problem is solved for intermediate water depth. In infinite water depth, the incident velocity potential will be different because the boundary conditions for the free surface wave change.

for $\phi = \phi_{R,j}$ or $\phi = \phi_D$. In this equation, $\sigma(\hat{x},\hat{y},\hat{z})$ is the source strenght at point $(\hat{x},\hat{y},\hat{z})$ on the mean wetted surface S_B and $G(x,y,z,\hat{x},\hat{y},\hat{z})$ is the Green's function, which shows the influence of a pulsating source σ at $(\hat{x},\hat{y},\hat{z})$ on the potential ϕ at location (x,y,z), and is singular for $(\hat{x},\hat{y},\hat{z}) = (x,y,z)$. This function satisfies the Laplace equation, the linearised boundary conditions on the free surface and the seabed, and the radiation condition at $\pm\infty$. The exact expressions for the Green's functions are stated in Journée & Massie (2008) [30].

The differentiation of (5.1) can give the water velocities normal to the object surface, which have to satisfy the boundary conditions at S_B. This gives the following expression

$$\frac{\partial\phi}{\partial n_B} = -\frac{1}{2}\sigma(x,y,z) + \frac{1}{4\pi}\int_{S_B}\sigma(\hat{x},\hat{y},\hat{z})\cdot\frac{\partial G(x,y,z,\hat{x},\hat{y},\hat{z})}{\partial n_B}dS \tag{5.2}$$

where $\partial/\partial n_B$ is defined as the gradient in direction normal to the body surface.
To solve for the velocity potential numerically, the wetted surface of the floating body is converted into a mesh consisting of N_p quadrilateral panels or grid cells. On these panels, the source strengths are assumed homogeneous, which leads to the following discretised version of (5.2):

$$-\frac{1}{2}\sigma_m + \frac{1}{4\pi}\sum_{n=1}^{N}\sigma_n\frac{\partial G_{mn}}{\partial n_B}\Delta S_n = n_m \qquad \text{for } m = 1,...,N_p \text{ and } n \neq m \tag{5.3}$$

This equation expresses the interaction between a source strength σ_m on panel m and the sources σ_n on all other panels n. The normal velocity requirement can only be met at a single point on the panel, called the collocation point. This is chosen to be the centroid of the quadrilateral.

The discretised equation (5.3) can be transformed into an $N_p \times N_p$ linear system (for each problem ϕ_D or $\phi_{R,j}$), to find the unknown complex source strengths $\sigma_n, n \in \{1,2,...,N_p\}$. These source strengths can then be translated to a velocity potential at each location (x,y,z) on S_B.

The solution methods for this linear system will be discussed in section 5.1.3. The mesh that is used to describe the floater surface is discussed in section 5.2.2. First, the different numerical diffraction models available will be discussed.

5.1.2. Diffraction models & Capytaine

Diffraction models solve for wave-structure interactions using a boundary element method, introduced in section 5.1.1. A selection of numerical diffraction models that use this panel method to compute wave loads on offshore structures are Capytaine [2], Nemoh [15], WAMIT [36], Diffrac [46] and Ansys Aqwa [4]. Comparison studies between the various models show good agreement between the codes, for example [15, 31, 52, 54]. One of the large differences is that WAMIT and Ansys Aqwa offer the inclusion of second order wave effects, whereas the other models are purely linear. Furthermore, Nemoh might have difficulties with very thin elements [54].

Both Nemoh and Capytaine were initially explored, as they are the only open source diffraction codes. The models showed comparable results for various floater configurations: their mutual differences were smaller than the influence of further mesh refinement. Capytaine was selected for the rest of the work, as it is still commonly used and supported at this moment, unlike Nemoh. It was developed by rebuilding the open source BEM solver Nemoh in Python.[2] Documentation on Capytaine is quite extensive but informal, often referring to Nemoh documentation as it started as an exact copy of this code.

5.1.3. Solving the linear system

The linear system that solves the velocity potential functions for each of the grid cells (as explained in section 5.1.1) is defined with an $N_p \times N_p$ full matrix, where the value N_p denotes the number of panels

---

[2] "Capytaine is a Python package for the simulation of the interaction between water waves and floating bodies in frequency domain. It is built around a full rewrite of the open source Boundary Element Method (BEM) solver Nemoh for the linear potential flow wave theory." More information and documentation can be found on `https://ancell.in/capytaine/latest/` and `https://github.com/mancellin/capytaine`.

or grid cells the mesh consists of. Namely, the matrix describes the interaction between each grid cell and all other grid cells. In the floater configuration described in section 5.2.1, with mesh described in section 5.2.2, N_p was approximately $6{\cdot}10^3$.

This linear problem can be solved using a direct method, such as the LU decomposition (matrix form of Gauss elimination method). In this case, a computational effort of $\mathcal{O}(N_p^3)$ is required [30, 41]. The other option that Capytaine provides is using an iterative method; the generalised minimal residual (GMRES) solver. This can reduce the effort to $\mathcal{O}(N_p^2)$, which is especially faster if the number of panels exceeds 500 [30] and will therefore be used in this study.

5.1.4. General output: hydrodynamic coefficients

The usual output for a boundary element method diffraction model are the hydrodynamic coefficients A, B and F_e of the object(s) considered, which have been previously introduced in sections 2.3.2 and 2.4.3. These parameters represent physical properties of the floating body which are needed to solve for the motion of the object (in frequency domain) by equation (2.19).

The exciting force F_e [N] is derived from the incident wave velocity potential ϕ_I and the panel method solution for the diffracted velocity potential ϕ_D, through equation (2.32). The added mass A [kg] and the radiation damping B [Ns/m] are derived from the panel method radiation solutions $\phi_{R,j}$ in each degree of freedom $j \in \{1, 2, ..., 6\}$, through equation (2.33). Recall that for a single wave frequency f, and if all 6 degrees of freedom j are considered, we have matrices $A, B \in \mathbb{R}^6 \times \mathbb{R}^6$ and exciting force vector $F_e \in \mathbb{C}^6$, as this latter coefficients includes a phase. Therefore, the general Capytaine output is a real $n_{DOF} \times n_{DOF} \times n_f$ array for A and B, and a complex $n_{DOF} \times n_f$ array for F_e.

5.1.5. Obtaining the surface elevation

The general diffraction model output described in the previous section is focused on

These are not the quantities of interest for this research however, as the objective is to determine the influence of the floating solar platforms on the waves. The physical quantities of interest are wave height and wave energy of the surrounding water surface area. These can be used to determine the breakwater-like performance of the floating solar structure by means of a transmission coefficient.

In case of a regular harmonic wave, the surface elevation of the free surface gravity waves is described by $\eta(x, y) \in \mathbb{C}$ (see section 2.2). The amplitude of this complex surface elevation $|\eta(x, y)|$ shows the oscillation amplitude of the water surface at a certain position in the water surface domain. The real part $\mathrm{Re}|\eta(x, y)|$ shows the surface elevation at $t = 0$. The surface elevation η is thus the quantity that gives insight in the wave height and wave energy in the environment around the floating object.

In order to compute the surface elevation, the velocity potential solution $\phi = \phi_I + \phi_D (+\phi_R)$ is used. To get from the diffraction or radiation result to the surface elevation, two steps have to be taken.

1. $\phi|_{S_B} \rightarrow \phi(x, y, z)$
   Whereas the general output of a diffraction model gives the hydrodynamic coefficients A, B and F_e, the model first solves for the (complex, position dependent) velocity potential for the diffraction or radiation problem considered on the wetted surface of the object , $\phi_D|_{S_B}$ or $\phi_R|_{S_B}$. This was explained previously in section 5.1.4. To obtain the velocity potential in an arbitrary position $\phi(x, y, z)$, part of the integral problem can be solved again with the known results on the wetted surface as extra input parameters. In Capytaine, one can define a mesh on which $\phi(x, y, z)$ will be calculated from a previously obtained result. A free surface mesh is chosen, such that the velocity potential at $z = 0$ is computed for a certain (x, y)-domain. This procedure is done with the function `get_potential_on_mesh`, which needs the desired mesh and a diffraction or radiation result as input. It will then give the complex potential on the given mesh.

2. $\phi(x, y, z = 0) \rightarrow \eta(x, y)$
   From the velocity potential on this free surface mesh, the surface elevation $\eta(x, y)$ can be computed by using the free surface boundary condition (2.10). The relation between the surface

elevation $\eta \in \mathbb{C}$ and the velocity potential $\phi \in \mathbb{C}$ is as follows

$$\eta = i\omega g\phi \tag{5.4}$$

with g the gravitational acceleration constant, ω the angular frequency considered and $i = \sqrt{-1}$. This is the case for harmonic waves, where the oscillations are described with a complex exponential $e^{-i\omega t}$. The Capytaine function `get_free_surface_elevation` can perform both steps at once, such that the complex surface elevation is found at a given mesh from a previously obtained diffraction or radiation result.

Because the wave theory is assumed to be completely linear, surface elevations η_I and η_D can simply be added together to form the complete description of the diffraction problem. Furthermore, all motion amplitudes η are freely scalable. Thus, if the incident wave surface elevation amplitude $|\eta_I| \neq 1$, a scaling factor can be introduced to obtain the total result $\eta_I + \eta_D$.

The free surface mesh chosen in the first step determines on what domain the surface elevation will be computed. When a large domain in x and y is chosen, and split up in grid cells, the 3D results of the floating object can be visualised. When interested in the 2D effects only, one can look at a mesh defined at $y = 0$, for a range in x.

For this surface elevation mesh, a resolution or grid size has to be chosen again. Here, a larger number of grid cells will give a more accurate visualisation of the resulting wave field, but also increases the computation time. Especially for the meshes that show the 3D effects, a high number of cells in both x and y direction can lead to long calculations. The grid size for the visualisation (the water surface mesh) was always chosen to be larger or equal than the grid size used for the object surface in the computation of the initial results (which is discussed in section 5.2.2).

5.1.6. Definition transmission and reflection coefficients

When the resulting surface elevation amplitude $|\eta_I + \eta_D|$ from the scattering solution is known, this will be used to define the transmission coefficient $K_t = H_t/H_i$. The incident wave height is fixed, and the resulting wave height H_t is derived from the resulting surface elevation amplitude $|\eta_I + \eta_D|$ behind the object. This is not trivial, because the wave amplitude is not constant over the water surface (x, y) due to the interference of incident and reflected or diffracted waves. The wave height behind the floater is not constant (in position), because nodes and anti-nodes are present in the wave environment.

The transmitted wave height is derived from the surface elevation amplitude by taking the average over the sheltered wave area of interest. Because the objective is to look at approximate two-dimensional attenuation performance, surface elevation at $y = 0$ is considered. The average surface elevation amplitude $|\eta_I + \eta_D|$ over the interval $0.5L_f < x < 100$ m is taken as a measure for H_t. This interval is chosen as close to the floater as possible, such that the impact of possible three-dimensional effects are reduced. Taking the average over a sheltered area of interest to measure global transmissibility was also done in [49, 55] for floating breakwater performance. This choice will be reviewed in the discussion section 6.

The reflection coefficient $K_r = H_r/H_i$ requires a reflected wave height, which is also position-dependent due to the interference of the incident and reflected waves. H_r is defined as first local maximum of the surface elevation $|\eta_D + \eta_I|$ in front of the structure, minus the incident wave amplitude $|\eta_I| = 1$. The anti-node which is located closest to the floating object is taken as a representative for H_r, because the three-dimensional effects caused by limited floater width in y-direction are smallest.

5.2. Method

The first order boundary element method diffraction model Capytaine is used to determine the surface elevation and wave transmission in presence of a floating solar platform. The scope is limited to the approximately two-dimensional scattering problem, with a horizontal seabed at intermediate water depth and incident waves parallel to the structure length. This was chosen such that the results could be compared to the basin test results presented in section 4, which were two-dimensional. Because the diffraction model is based on a 3D panel method, 2D results were approximated by increasing the floater width.

The floater configuration and mesh choice are described in sections 5.2.1 and 5.2.2. After that, the wave conditions chosen for the incident waves are stated in section 5.2.3.

5.2.1. Floater configuration

To test the wave transmission through a fixed submerged floater, the floater configuration shown in Figure 5.1 was used. The floater dimensions are $12 \times 200 \times 0.5$ m. This size was based on replication of the offshore floater with a length of 12 m and a height of 0.5 m. The large width was chosen to approximate a two dimensional setup. In the central $y = 0$ axis, the velocity potential or surface elevation profile will approximate the response of an infinitely long floater.

The object's gravitational centre was located at $(0, 0, -0.083)$ m. The floater draft was taken two third of the floater, which is realistic for Oceans of Energy's offshore floating solar platforms [31]. This lead to a centre slightly below the equilibrium water surface level $z = 0$.

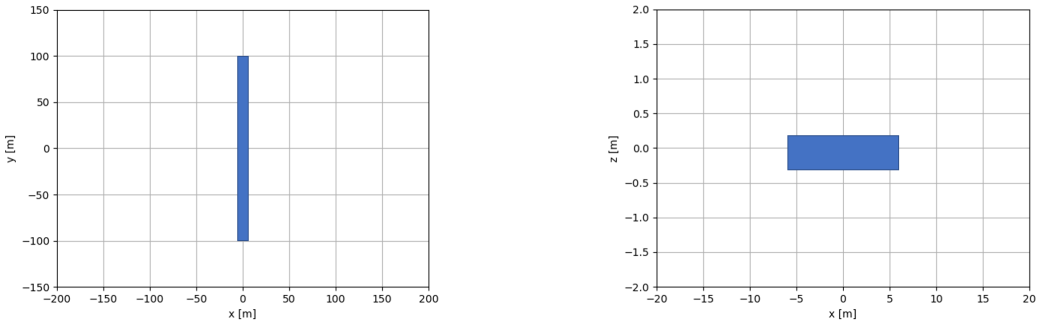

(a) Floater dimensions in x, y: top view

(b) Floater dimensions in x, z: side view.

Figure 5.1: Configuration of the floater for the BEM diffraction model.

The water depth was taken $h = 24$ m, to simulate the offshore water depth at the North Sea site location. Overall, the floater dimensions and water environment were similar to the basin test setup. The only large difference in the configuration is the floater width to simulate the 2 dimensional setup, and the number of floaters included in the tests.

5.2.2. Mesh & resolution

The floater described in section 5.2.1 had to be converted into a mesh for the numerical BEM computation method, as explained in section 5.1.1. A minimum amount of panels or grid cells per wavelength is needed to describe a wave properly. For linear quadrilateral elements, the maximum size of a grid cell is $^1/_{10}\lambda$, where λ is the incident wavelength [56]. The range of wavelengths investigated is in between 17 and 129 m, see Table 5.1. This means that theoretically, a mesh size of 1.5 m or less should be sufficient to solve the integral problem numerically.

The mesh was chosen as fine as possible, with the following restrictions:

- Memory
  Capytaine has to save the full matrix in $\mathbb{C}^{N_p} \times \mathbb{C}^{N_p}$ that constitutes the linear problem (see section 5.1.3), where N_p is the number of panels or grid cells that the floater mesh consists of. From a certain number of panels onwards, $N_p \approx 10^4$, the model will give a memory error.[3] This does depend on the memory available on the PC that is used.
- Running time
  The higher the number of grid cells used, the longer the computation time τ needed to solve the

---

[3] $N_p = 10^4$ requires a memory of $10^4 \cdot 10^4 \cdot 2 \cdot 64 \approx 10^{10}$ bytes, thus 10GB. A lower float precision could have been used to represent the complex values however, to reduce to 1GB.

BEM diffraction problem. Running times were kept at less than 15 minutes per diffraction computation, for a single wave frequency f. This restriction was often similar to the limit of the memory available.

To study how wave transmission depends on the wave frequency or wavelength, the diffraction computations have to be repeated for different wave conditions. Furthermore, the derivation of the surface elevation amplitude on a desired (water surface) mesh took additional computation time τ_η, especially for the three-dimensional results. This depended on the visualisation mesh used, but was in the order of one hour for the finest three-dimensional surface elevation. Therefore, the total computation time needed was longer: $n_\omega \cdot \tau$ to solve the diffraction problems and $n_\omega \cdot \tau_\eta$ to solve for the surface elevation.

The final computations for the floater configuration in Figure 5.1 were done with grid cell dimensions of 0.75 m, 1.25 m and 0.033 m in x, y and z directions respectively. Therefore, the $12 \times 200 \times 0.5$ m floater was divided into 16 grid cells in x-direction, 160 in y-direction and 15 in z-direction. Because the diffraction problem only requires the wetted surface area below the equilibrium water level $z = 0$, the body surface above $z = 0$ is removed. This leaves 6080 panels in total for the diffraction computation. Some illustrations of the floater mesh are given in Figure 5.2. The differences in grid size dimension relate to the floater configuration and the wave propagation in x-direction, and were based on error analysis in a mesh sensitivity study (see section 5.3.4).

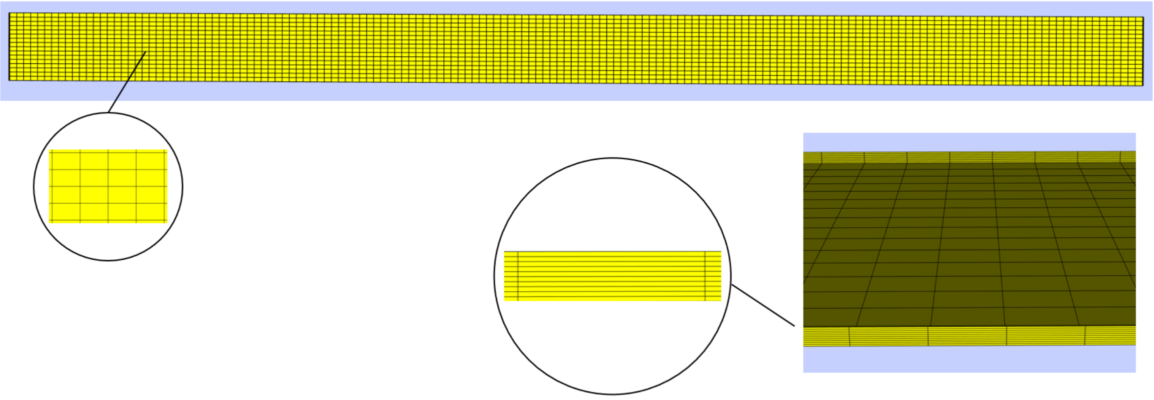

Figure 5.2: Illustrations of the floater mesh used for the BEM diffraction model. Top view and side view are shown.

Because the object is meshed first and then divided into a part above and below the equilibrium water level, the number of grid cells in z-directions should be chosen carefully to ensure an integer amount of grid cells are used to compose the submerged body mesh. Because the floater draft was set to $^2\!/_3 H_f$, the amount of grid cells used to describe the floater in z-direction had to be a multiple of 3. If this were not the case, the numerical errors in the surface elevation increased (in the order of $\pm$5%).

A convergence study was done to see the relation between the mesh resolution and the numerical errors. These results will be presented in section 5.3.4.

5.2.3. Wave conditions

The diffraction model assumes harmonic incident waves with a specified (angular) frequency $\omega = 2\pi f$ and scaled wave amplitude A, described by velocity potential (2.15). Thus, a separate scattering problem is solved for each wave frequency considered.

The incident wave amplitude is chosen $A = |\eta_I| = 1$ m, because of easy normalisation. Notice that this does not yield the same wave height as in the basin tests, becuase $H_i = 2$ m and the regular basin tests with varying frequency had $H_i = 1$ m on offshore scale (see wave conditions in Appendix I). The diffraction results can always be scaled by a factor $^1\!/_2$, because the model is entirely linear.

The incident wave frequencies f were chosen in the range $f \in [0.1, 0.3]$ Hz, thus $T \in [3.33, 10]$ s. These conditions are similar to offshore North Sea wave conditions, which have $T_p \in [3, 10]$ s for 95% of the time [1]. Furthermore, this was the range in which the regular and irregular wave tests were chosen for the basin test, see section 4. Because linear wave theory is used, the wavelength λ can be computed from the wave period T and water depth $h = 24$ m with the linear dispersion relationship, equation (2.17). The five main wave conditions tested are shown in Table 5.1, with the corresponding wavelength.

f [Hz]	T [s]	λ [m]
0.1	10	129
0.15	6.67	68
0.2	5	39
0.25	4	25
0.3	3.33	17

Table 5.1: Wave conditions for numerical BEM diffraction model in $h = 24$ m water depth, incident wave amplitude $A = 1$ m.

5.3. Results

5.3.1. Approximate 2D diffraction results single floater

The two-dimensional diffraction surface amplitudes $|\eta_I + \eta_D|_{y=0}$ for wave frequencies $f = 0.1, 0.15, 0.2, 0.25, 0.3$ Hz are included in Appendix E. The surface elevation for the longest wave, $f = 0.1$ Hz and $\lambda = 129$ m, is shown in Figure 5.3 as a function of the position x. Remember that the incident wave height amplitude was set to $|\eta_I| = 1$ everywhere.

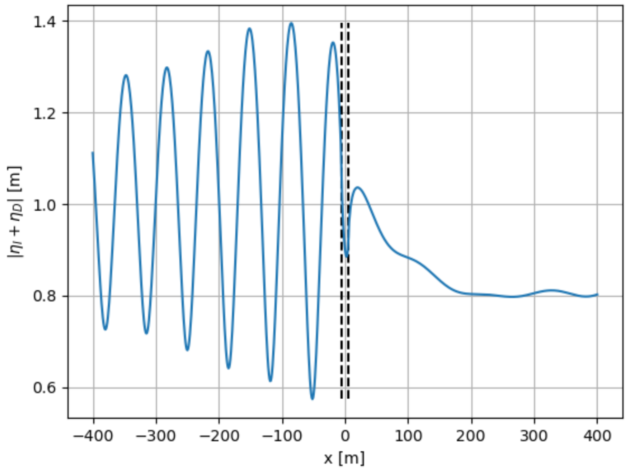

Figure 5.3: Amplitude of surface elevation $|\eta_I + \eta_D|$ for the 2D diffraction model as a function of x at $y = 0$. The dotted lines show the edges of the submerged body. The incoming waves had a frequency $f = 0.1$ Hz, wavelength $\lambda = 129$ m, wave height $H = |\eta_I| = 1$ m. The water depth was $h = 24$ m.

This figure shows a standing wave in front of the floating object ($x < -6$ m), and a decreased wave amplitude behind it ($x > 6$ m). This also showed for the other wave frequencies tested.

Standing waves in front of structure

The resulting surface elevation amplitude $|\eta_I + \eta_D|$ for the approximate 2D scattering problem showed an oscillation around $|\eta_I + \eta_D| = 1$ m in front of the floating structure ($x < -6$ m). This shows the surface elevation at a specified location $(x_1, 0)$, oscillates in time between different values in comparison to another location $(x_2, 0)$. The minima in surface elevation amplitude correspond to the nodes of a standing wave, the maxima to the anti-nodes. This standing wave pattern can be explained by interference of the incident and reflected waves; waves that reflect from the object surface have the same wave frequency and opposite propagation direction in comparison to the incident ones.

In Figure 5.3, the node closest to the structure shows that the surface elevation oscillates in between 0.55 and -0.55 m at this given location $(x, y) = (-52, 0)$. The anti-node closest to the structure shows that the surface elevation oscillates in between 1.37 and -1.37 m at this location $(x, y) = (-19, 0)$. Notice that the distance between two consecutive nodes (or anti-nodes) is indeed exactly $\lambda/2$, as expected for a standing wave.

Notice that the standing wave pattern is not constant over the domain in front of the structure, which is shown over a larger distance as well in Figure 5.5. This is likely the result of 3D diffraction effects, which causes the standing waves to diffract wave energy to the sides, $y > 100$ m and $y < -100$ m. If the problem would be entirely two-dimensional, the nodes and anti-nodes would have a constant value over the whole domain $x < -6$ m, because only reflection and transmission are modelled. Because dissipation is disregarded in linear wave theory, the incident and reflected waves have a constant wave height over their propagation path, and would thus add up to a constant interference pattern. To confirm the three dimensional effects, Figure 5.9 in section 5.3.3 shows surface elevation over a large domain in (x, y).

Decreased wave amplitude behind structure

The surface elevation amplitudes behind the floater ($x > 6$ m) have values $|\eta_I + \eta_D| < 1$ everywhere, except just behind the floating object for the waves with lowest frequency (and thus largest wavelength). To look further into wave transmission, the surface elevation amplitudes behind the floater are plotted for various wave frequencies f in Figure 5.4.

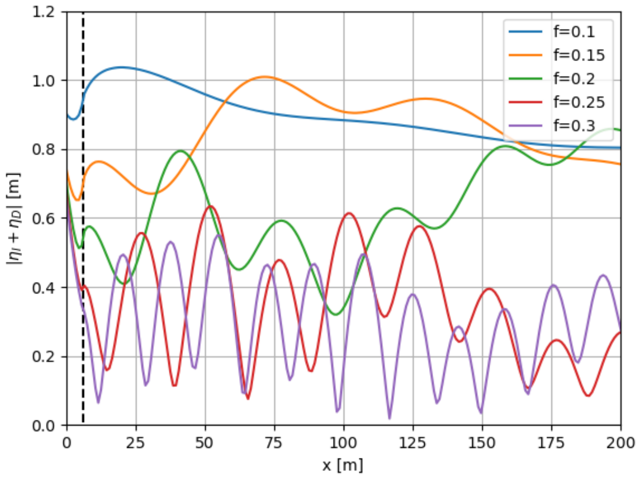

Figure 5.4: Surface elevation $|\eta_I + \eta_D|$ for the 2D diffraction model as a function of x at $y = 0$ for various incoming wave frequencies and thus wavelengths. The dotted line shows the edge of the floater.

The decreased surface elevation amplitude $|\eta_I + \eta_D| < 1$ for $x \in [6, 200]$ m indeed shows for the other wave conditions plotted. Scattering of the incident wave for a fixed rigid barge thus leads to a decrease in wave transmission for all wave conditions, as expected.

From the transmitted surface elevation amplitude for these five wave conditions it already seems that the surface elevation amplitudes decrease more for the higher wave frequencies. Namely, both the maxima and minima are generally lower for $f = 0.25$ and $f = 0.3$ Hz. Thus, the impact of the submerged object is different for the short and long waves, as theoretically was expected from studies on floating breakwaters (see section 3). Namely, length floater $L_f = 12$ m stayed constant, and the wavelength λ varied between 129 and 17m according to table 5.1. Long waves are reflected less (see also the standing wave patterns in front of the structure in Appendix E) and transmitted more, in comparison to the shorter ones. This relation will be examined further in section 5.3.2.

The observation that the wave surface amplitude just behind the floater was greater than the unit incident amplitude for $f = 0.1$ Hz was also observed in [51] for the long waves, and is likely explained by 3D diffraction effects from the two ends of the object at $y = -100$ and $y = 100$ m. This will be discussed further in section 5.3.3 and the discussion in Chapter 6.

Oscillations in surface elevation behind structure

The surface elevation amplitude is not constant in x in the region behind the floater. As ripples on the generally decreased surface elevation, oscillations show behind the structure. In Figure 5.4, this is visible for the higher frequencies. For the long waves, $f = 0.1$ Hz and $\lambda = 129$ m, the oscillations are present as well but over a longer distance in x and further away from the object. This can bee seen in Figure 5.5, where the surface elevation amplitude is shown over a larger range in x.

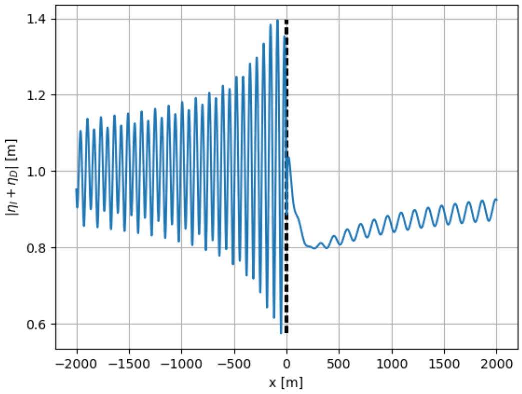

Figure 5.5: Surface elevation amplitude $|\eta_I + \eta_D|$ for the 2D diffraction model as a function of x at $y = 0$. The dotted lines show the edges of the submerged body. The incoming waves had a frequency $f = 0.1$ Hz, wavelength $\lambda = 129$ m, the water depth was $h = 24$ m.

The oscillations in $|\eta_I + \eta_D|$ have a period (node-to-node distance) that corresponds exactly to the incident wavelength $\lambda = 129$ m. Thus, this oscillation has a period which is twice as long as the standing wave in front of the object. These ripples at $y = 0$ are part of a three-dimensional interference pattern behind the floater, which is shown in section 5.3.3 and Appendix F. In these sections, the oscillations will be discussed in further detail.

5.3.2. Parameter study: K_t and K_r

To investigate the parameter dependence of the wave transmission and wave reflection further, the transmission coefficient K_t, and reflection coefficient K_r were studied. The main parameter of interest was the incident wave frequency f. After these results, short remarks will be made on the dependence on the number of floaters included n_{FL} and the incident wave height H.

Frequency dependence

The transmission and reflection coefficients K_t and K_r were defined as introduced in section 5.1.6, and computed for the scattering solutions with different incident wave frequencies f. These are plotted Figure 5.6, together with the quadratic sum of the two $K_t^2 + K_r^2$.

From this figure, it can be seen that the wave transmission decreases as a function of the incident wave frequency, whereas the reflection increases. This was expected, as the lack of wave transmission can be caused by either reflection or diffraction in a BEM diffraction model. From a frequency of 0.13 Hz onwards, reflection increased and transmission decreased. This corresponds to a wavelength to floater length ratio of $\lambda/L_f \approx 7$.

What can be seen is that the sum $K_t^2 + K_r^2$, which was theoretically expected equal to one, is not constant over the frequencies and shows quite a lot of values $K_t^2 + K_r^2 > 1$ for both low and high frequent waves. This gives a perspective on how well the transmission and reflection were defined, and will be discussed further in the discussion, Chapter 6, also in relation to the basin test results.

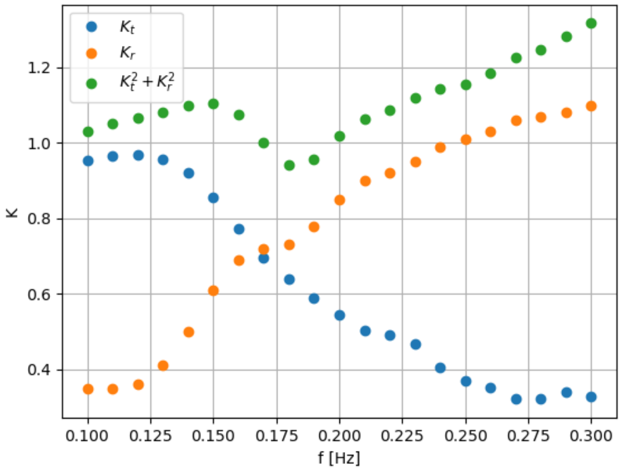

Figure 5.6: Transmission coefficient K_t, reflection coefficient K_r and quadratic sum $K_t^2 + K_r^2$ as a function of incident wave frequency f for the approximate 2D diffraction problem.

System size dependence

To investigate the dependence of wave transmission K_t on the system size, n_{FL}, one would like to increase the number of floaters included in the configuration and compute the scattering results again. However, it could be seen that increasing the number of floaters to n yielded approximately the same results as enlarging the floater length to nL_f. This is because the spacing between the floaters was small in comparison to the floater length (only 0.3 m whereas L_f was 12 m). As the objects are not able to move in the scattering problem considered, the incident waves encounter these separate floaters as if it were one large platform which the water has to move around or underneath. Therefore, in the approximately two-dimensional scattering model, the dependence of K_t and K_r on n_{FL} was approximately the same as the dependence on the floater length L_f for a single floater. This latter approach has a lower computational cost, and avoids possible gap resonance effects (see for example [8, 18, 44]) in the solutions.

The system size dependence n_{FL} was first investigated with the frequency analysis results that were already available. Because the problem is entirely linear, the wave transmission depends specifically on the relative floater length L_f/λ in the propagation direction of the waves [18, 32]. By changing the frequency and thus wavelength of the incident wave, the parameter dependency on L_f/λ was found. The dependence of K_t on the dimensionless floater length L_f/λ is plotted in Figure 5.7 for the typical floater configuration, where $L_f = 12$ m, in blue.

Adapting L_f would theoretically yield the same results in terms of this dimensionless parameter (if the problem were entirely two-dimensional), but requires more memory and longer computation times as more grid cells are needed to model a larger floater in the same mesh resolution. The similarity with results for $L_f = 24$ m (simulating 2 floaters) and $K_f = 36$ m (simulating 3 floaters) was checked by computing the transmission coefficient for these floater configurations as well. These results are also shown in Figure 5.7.

As expected, the transmission is shown to decrease with increasing relative floater length L_f/λ. Translating this back to the dependence on the number of floaters included n_{FL} (in parallel to the wave propagation direction), Figure 5.7 shows that a larger number of floaters will cause an approximately linear decrease the wave transmission for $L_f/\lambda \in [0.2, 0.8]$. Notice that for example for $\lambda = 100$ m, the number of floaters considered in Figure 5.7 would be 10 to 100, so the range $L_f/\lambda \in [0.1, 1.0]$ is more justified for the smaller wavelengths. This high number of floaters is not expected to be well simulated by the scattering around a single (fixed) rigid floater.

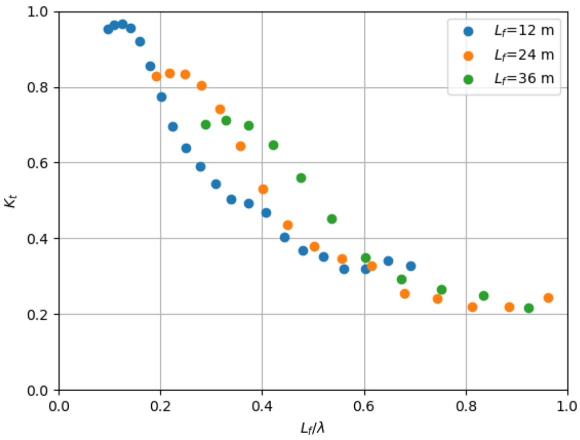

Figure 5.7: Transmission coefficient K_t as a function of the floater length over wavelength L_f/λ for the approximate 2D diffraction problem, computed with various floater lengths $L_f = 12, 24$ and 36 m.

Because the problem was not entirely two-dimensional however, the scalability of the results in Figure 5.7 is not entirely valid. The diffraction from the ends of the floater cause differences in transmission between the two possible approaches for varying the dimensionless parameter L_f/λ. Using a different floater length will lead to an altered object shape, as the floater width was kept $W_f = 200$ m. The differences between the results for various values of L_f show that computing the transmission coefficient by decreasing the wavelength or by increasing floater length indeed gives different results.

5.3.3. 3D effects

The setup for the diffraction problem, described in section 5.2, was approximately two dimensional. The results in section 5.3.1 showed oscillations in the surface elevation amplitude behind the structure at $y = 0$, which indicated an interference pattern to be present because of oscillations in the wave heights behind the floater. Thus, the 200 m wide floating structure used to approximate an infinitely long object in y-direction, still has three dimensional diffraction effects present around the structure.

To investigate the 3D effects that were present in these simulations, the surface elevation was computed on a two dimensional mesh in the (x, y)-plane. The three dimensional effects in the resulting surface elevation at are given over the domain $(x, y) \in [-50, 200] \times [-125, 125]$. This is shown for five wave frequencies tested for $f \in [0.1, 0.3]$ Hz (see Table 5.1) in Appendix F. The plots for incident wave conditions $f = 0.1$ and $f = 0.25$ are shown in Figures 5.8a and 5.8b respectively.

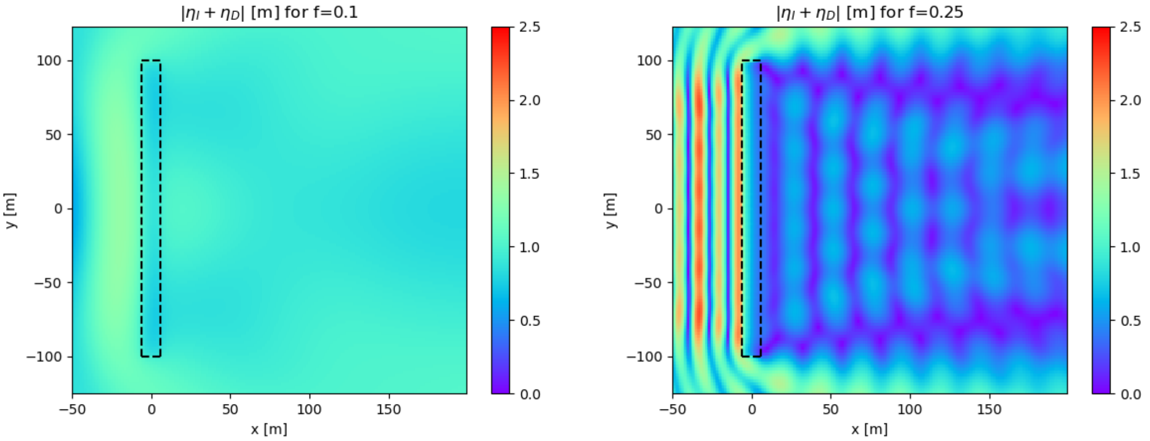

(a) $f = 0.1$ Hz, $\lambda = 129$ m

(b) $f = 0.25$ Hz, $\lambda = 25$ m

Figure 5.8: Amplitude of complex surface elevation $|\eta_I + \eta_D|$ for the diffraction model over the domain $(x, y) \in [-50, 200] \times [-125, 125]$ for incident waves with frequency f and wavelength λ. The dotted lines show the edges of the submerged body.

The results show that interference patterns are present behind the structure for both wave conditions, which can explain the oscillations in surface elevation behind the structure at $y = 0$, see Figure 5.4. The diffraction patterns show agreement with results for diffraction around 200 m wide floating breakwaters in [5, 51].

The main result that the overall transmission decreases as the ratio L_f/λ increases holds in general for the area behind the floating object. Remember that the normalised wave elevation amplitude reflects the transmission coefficient, and therefore shows the transmission coefficient is spatially dependent, as introduced in 5.1.6.

When the wavelength decreases further (see Figure F.1e for $f = 0.3$ Hz, $\lambda = 17$ m, Appendix F) the interference pattern shows less variation in wave surface amplitude. The shadow zone behind the floater is more uniform the in (decreased) transmission when W_f/λ increases, because waves can diffract around the structure less. This is confirmed by for example the Sommerfeld diffraction solution around a semi-infinite breakwater [28] and was already observed in [51]. It indicates that the high-frequency results will be closer to the theoretical two-dimensional solutions, in case the floater width is kept constant.

To demonstrate the far field diffraction effects, the surface elevation is determined over a larger domain $(x, y) \in [-1000, 1000] \times [-200, 200]$. These results are shown in Figure 5.9, for incident wave frequency $f = 0.25$ Hz..

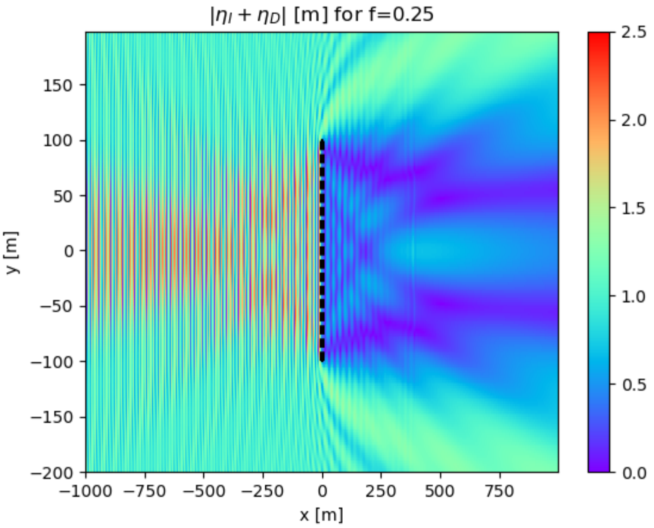

Figure 5.9: Amplitude of complex surface elevation $|\eta_I + \eta_D|$ for the diffraction model over the domain $(x, y) \in [-1000, 1000] \times [-200, 200]$ for incident waves with frequency $f = 0.25$ Hz and wavelength $\lambda = 25$ m. The dotted lines show the edges of the submerged body.

Indeed, the wave energy in the standing wave front seems to spread out to the sides of the floater $y < -100$ m and $y > 100$ m, which leaves a standing wave pattern which is less wide than the floater ($W_f = 200$ m). This likely caused the standing wave amplitudes further in front of the structure to decrease.

The implications of the three-dimensional diffraction on the approximate two-dimensional transmission analysis will be discussed further in the discussion, Chapter 6.

5.3.4. Mesh sensitivity

To study the numerical errors that might be present in the model, the mesh sensitivity of the diffraction solutions is looked into. Remember that the wetted surface of the floating object is meshed into rectangular grid cells, as presented in section 5.2.2. The total number of grid cells used is restricted by the memory needed for the linear problem, as well was the computation time required.

The effect of grid refinement on the surface elevation amplitude is visualised in Figure 5.10. In these plots, $|\eta_I + \eta_D|$ at $y = 0$ is plotted as a function of x in Figure 5.10 for different body mesh sizes. Here, the combined effect of refining the grid in all three x, y, z directions is visualised for $f = 0.1$ Hz and $f = 0.3$ Hz waves. In both cases, the curves lie closer together for the finer mesh choices, thus the solutions indeed seem to converge.

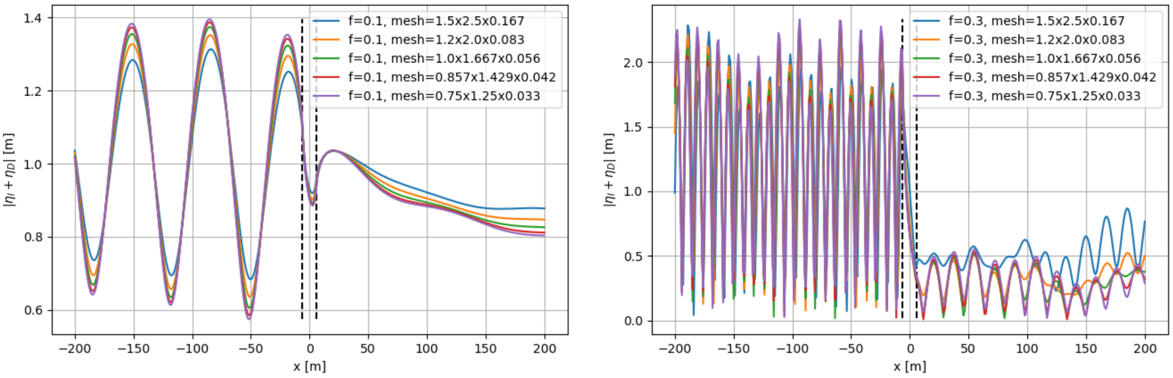

(a) $f = 0.1$ Hz, $\lambda = 129$ m

(b) $f = 0.3$ Hz, $\lambda = 17$ m

Figure 5.10: Surface elevation amplitude $|\eta_I + \eta_D|$ at $y = 0$ as a function of x for various mesh sizes. The dotted lines show the edges of the submerged body.

The difference in surface elevation for the coarser grid sizes are larger for $f = 0.3$ Hz, shown in Figure 5.10b. This larger error for the higher frequency wave condition was expected, as the number of grid cells in comparison to the wavelength λ determines the accuracy. Notice that from a grid size of 1.0 m × 1.667 m × 0.056 m onwards, it is difficult to distinguish the solutions for $f = 0.3$ Hz. This is in accordance with the rule of thumb to use grid sizes smaller than ${}^{1}\!/_{10}\lambda \approx 1.7$ m.

The grid size h is defined differently for each of the three directions, based on the floater configuration (section 5.2.1) and the propagation of the incident wave in x-direction. The effect of refinement in each of these three directions separately will be studied below.

To quantify the mesh sensitivity of the diffraction solution, the normalised root mean square error (NRMSE) is studied, which is defined as

$$NRMSE = \frac{1}{\gamma_{max} - \gamma_{min}} \sqrt{\frac{\sum_{n=1}^{N} (\hat{\gamma}_n - \gamma_n)^2}{N}} \tag{5.5}$$

In this equation, $\hat{\gamma}_n$ is the estimate of γ_n, for each point $n \in \{1, 2, ..., N\}$ in the domain considered. γ_{max} and γ_{min} are the maximum and minimum value that γ attains in this dataset.

The differences in surface elevation amplitude results are quantified using this error measure. The surface elevation amplitude solution obtained with the finest body mesh resolution is used as the reference solution γ. The normalised root mean square errors are thus defined with respect to this finest-grid solution. The surface elevation $|\eta_I + \eta_D|$ was computed for the domain $x \in [-200, 200]$, $y = 0$. This region is divided into a water surface mesh of $N \times 1$ grid cells. The squared error $(\hat{\gamma}_n - \gamma_n)^2$ for the surface elevation at positions x_n, $n = 1, 2, ..., N$, was thus computed for the solutions $\hat{\gamma}$ with a coarser object grid.

The normalised root mean square error with respect to the finest grid solution for the wave surface elevation is plotted as a function of the grid size h in Figure 5.11. For each plot, the grid size is refined in one direction (h_x, h_y or h_z), while the grid size in the other two directions is kept constant. The figure shows the error for the two wave frequencies $f = 0.1$ and $f = 0.3$ Hz. Wave conditions with lower frequencies ($f = 0.1$ Hz) have a smaller normalised mean square error compared to the high frequent waves ($f = 0.3$ Hz) because the amount of grid cells per wavelength is larger.

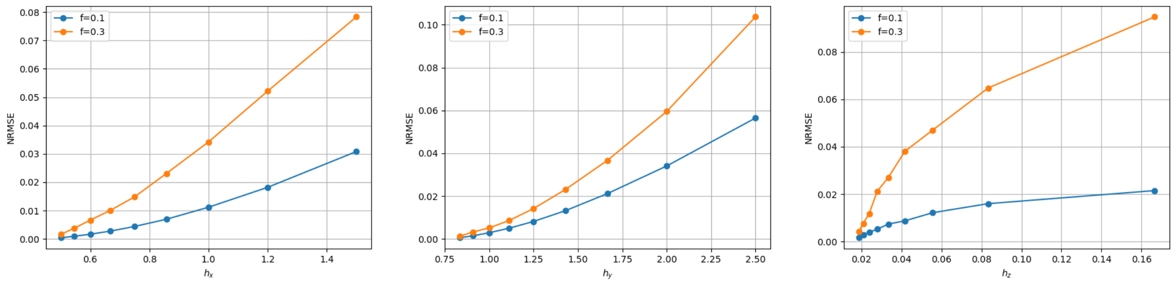

(a) Resolution refinement x (b) Resolution refinement y (c) Resolution refinement z

Figure 5.11: Plots of the normalised residual mean square error as a function of the grid size h [m] when refining the mesh in a single direction. Constant grid size values were 0.75 m in x-direction for subfigures b and c, 1.25 m in y-direction for subfigures a and c, 0.033 m in z-direction for subfigures a and b.

From Figure 5.11 it can be concluded that refining the mesh will give a more accurate result for all three directions. The solutions converge to the finest-mesh solution as the grid size h decreases. There is a difference in the shape of the curve for h_z and the curves for h_x and h_y. To investigate the convergence rates of these numerical errors, a (double) logarithmic plot is shown in Figure 5.12.

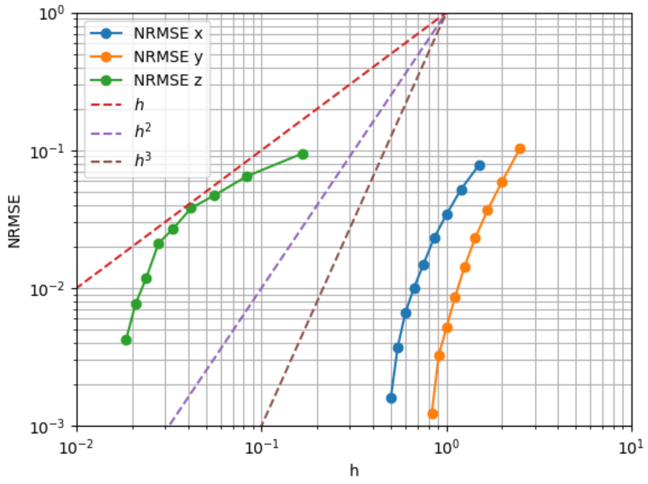

Figure 5.12: Logarithmic plot of the normalised residual mean square error as a function of the grid size h [m] for refinement in the x, y and z direction. The reference lines h, h^2 and h^3 are shown as well.

From this figure, it looks as if the normalised root mean square errors show super-linear convergence in all three directions, because the slopes of the NRMSE curves are steeper than the reference line h. Notice that the errors have not converged yet to the numerical precision error of 10^{-6}. The boundary element method is expected to converge in second order because the basis functions for ϕ are linear.

The final grid sizes used to obtain the results of sections 5.3.1-5.3.3 were h_x=0.75 m, h_y=1.25 m and h_z=0.033 m. The normalised root mean square errors for these mesh choices were less than 1% for the longest waves with $f = 0.1$ Hz, and 2% for the shortest waves with $f = 0.3$ Hz. Because this error is averaged over the domain locations x_n, the error could locally be higher. Because the model has not converged yet, and the error is computed with respect to a numerical approximation as well, no guarantees can be given for the error bounds in mathematical sense.

With respect to the objective of this research, a numerical error of 2% is workable. Firstly, the general wave attenuation behaviour is of interest, thus the exact surface elevation values for a specified position are less important. Moreover, the effect of other errors in the model approach are expected to be larger. The model assumptions, such as the small angle approximation and the ideal properties of the fluid, will likely contribute to an error in the estimations with a larger order of magnitude.

Even for the finest resolutions possible for this floating object due to the restrictions in memory, the order of magnitude of the normalised root means square error is still 10^{-3}. This gives an indication for the numerical error bounds for the 2D diffraction results, when applied to an object of these dimensions.

5.4. Result summary

This thesis investigates a proof of concept for applying a linear boundary element method diffraction model to a floating solar structure, restricted to scattering only. The near-field wave environment of the solar structure, for constant intermediate water depth $h = 24$ m, was investigated in an approximate two-dimensional setting in this chapter.

The BEM diffraction model could be applied to the shallow floating solar structure to compute the linear diffraction solution. Then, the surface elevation amplitude $|\eta_I + \eta_D|$ could obtained from the incident and diffracted velocity potential solutions. The results were in accordance with the expectations, as the surface elevation showed an overall decrease in amplitude behind the object and standing waves in front of the floating object. Therefore, the diffraction solutions demonstrated a decreased wave transmission due to the reflection of waves in opposite direction.

By simulating different wave conditions, the wave transmission coefficient K_t showed to decrease as a function of the incident wave frequency f (and thus for decreasing wavelength λ). This relation was approximately linear in the region $f \in [0.13, 0.27]$ Hz, thus from $\lambda/L_f \approx 7$ onwards. The transmission dependence on the number of floaters parallel to the propagation direction, n_{FL}, was investigated by enlarging the floater length L_f. The results showed a decrease in wave transmission as a function of the relative floater length L_f/λ.

The wave reflection K_r increased as a function of the incident wave frequency f (and thus for decreasing wavelength λ). The quadratic sum relation $K_t^2 + K_r^2 = 1$ that was theoretically expected from wave energy conservation reasoning did however not hold for most of the wave conditions tested. The observation $K_t^2 + K_r^1 > 1$ gives an indication that the definitions of K_t and K_r in this approximately two-dimensional setting might not be an accurate representation, mainly because of three-dimensional diffraction effects.

A mesh sensitivity study showed that the results had not been numerically converged yet. Even when the maximum resolution was used for this model setup, numerical errors were of the order 10^{-3}. Memory restrictions limited further mesh refinement for the wide object, leaving the obtained results with an average numerical error of 2% over the surface elevation domain. This still leaves the obtained results workable, as the model assumptions are assumed to have a larger impact. The influence of high aspect ratios for the grid cells should be looked into, as mesh convergence in x and y-direction showed to be different from the z-direction.

6

Discussion

In this chapter, the discussion points for the basin test and the numerical model will be presented first, in sections 6.1 and 6.2 respectively. After that, these results are compared in 6.3 to see how well wave transmission can be predicted by the numerical diffraction model. The implications of this research for offshore floating solar and multi-use will be discussed in 6.4, followed by suggestions for further research in 6.5.

6.1. Basin test

For the basin test results, presented in chapter 4, the most important points of discussion are:

- Uncertainty in the results for the short wavelengths ($\lambda < 6L_f$) due to a limited amount of tests and resonance effects
- Additional incident wave energy in the irregular wave tests with a floating system present
- Possible errors in the time series analysis for regular wave surface elevation measurements
- Possible errors in reflection analysis

These effects will be discussed one by one in sections 6.1.1-6.1.4. Further discussion points and recommendations for improving the basin test procedure are given in Appendix M.

6.1.1. Uncertainty in short wavelength regime

From the basin test results, it was concluded that transmission decreased for the short wavelengths (from $\lambda < 6L_f$ onwards). In this regime however, only a limited amount of tests were performed, which leads to an increased uncertainty in both the transmission and reflection coefficient.

For the wavelengths $\lambda/L_f < 2$ (thus $f > 0.25$ Hz), where attenuation decreased to zero, only two regular wave conditions were tested and could give information on the decreased wave transmission. These results showed some time-dependency in the wave surface elevation, which does not show in the wave height results H_{p1}, H_{r1}, H_{p2} and H_{r2}. It is difficult to quantify the possible error this could have brought in the transmission coefficient, but it can be noted that the error bounds are likely to be larger for the high frequency regime. An estimate is made at $K_t \pm 0.1$, which was also based on the spread between the repeated tests for different system sizes.

One of these regular wave tests, test 15 with $H = 1.0$ m, $T = 4$ s and $\lambda = 25$ m at full scale, could not be used in transmission results for the full system size with $n_{FL} = 33$ floaters due to resonant behaviour. The surface elevation signal varied over time, shown in Figure 6.1. Also, there was a difference in wave amplitude between the four wave height meters within a set.

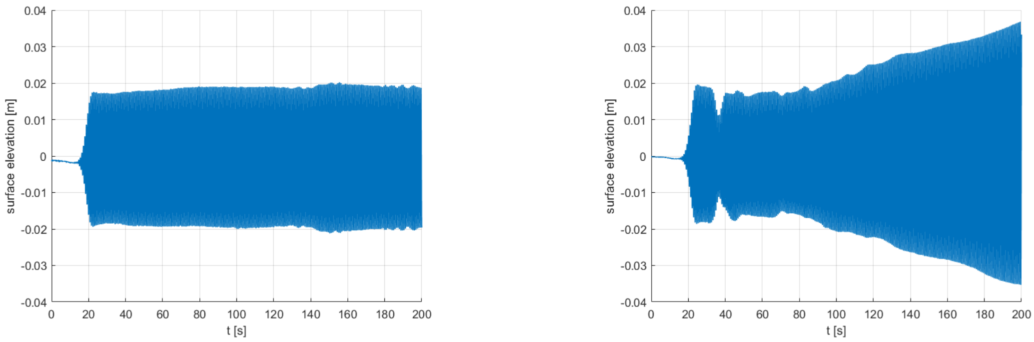

(a) Calibration test $n_{FL} = 0$

(b) System size $n_{FL} = 33$

Figure 6.1: First 200 seconds of the surface elevation measurements in [m] at basin test scale, measured by WHM 4 for regular wave test 15. Test conditions were $H = 0.04$ m on basin scale, $H = 1$ m full scale, $T = 0.8$ s on basin scale, $T = 4$ s full scale.

Figure 6.1b shows a surface elevation which increased over time when the largest floating system ($n_{FL} = 33$) was present. Upon repetition of test 15, approximately the same results were found, which makes a coincidental (measurement) error improbable. The calibration test did not show a variation in surface elevation, see Figure 6.1a. It is therefore unlikely that the increase in wave amplitude was caused by standing waves over the total length of the flume. Linear resonance seems to occur in front of the floating object, likely caused by wave reflections between the wave paddle and the floating system. The wave paddle's Active Reflection Compensation (ARC) might not have picked up the short waves, therefore reflecting them back as additional incident waves. This could occur especially for short waves, because these are present at the upper part of the water column only. The wave paddle can only compensate reflected waves by moving the whole water column, and might therefore have difficulties with the dampening out high frequent waves.

In future research, more regular wave tests with shorter wavelength would be a valuable addition to the testing programme. This was not possible within the setup used in this thesis however, as the steepness restrictions constrained the wave conditions with short periods for the minimally required wave height of $H = 1.0$ m and water depth $h = 21.25$ m (both full scale). A possible solution to overcome these restrictions would be choosing a smaller scaling parameter, and thus enlarging the length of the floaters in the model such that $\lambda < 2L_f$ could be tested more.

6.1.2. Additional incident wave energy

The irregular wave spectra showed an increase of incident wave energy in comparison to the calibration tests, especially around $f = 0.3$ Hz (see Figure 4.9 and Appendix K). This increased wave energy has an influence on the transmission results, because K_t is defined with the ratio of the incident and transmitted wave energy, see equation (4.12). The transmission coefficient still shows the proportion of transmitted waves correctly, also if the floating system is present, but the incident wave spectrum did not match the intended JONSWAP spectrum properly.

The difference between the incident wave variance density spectra is shown in Figure 6.2. When this difference in incident variance density is strictly positive for a certain frequency f, $E_{33}(f) - E_0(f) > 0$, this implies that more waves with this frequency were measured in the incident wave spectrum when the floating object was present.

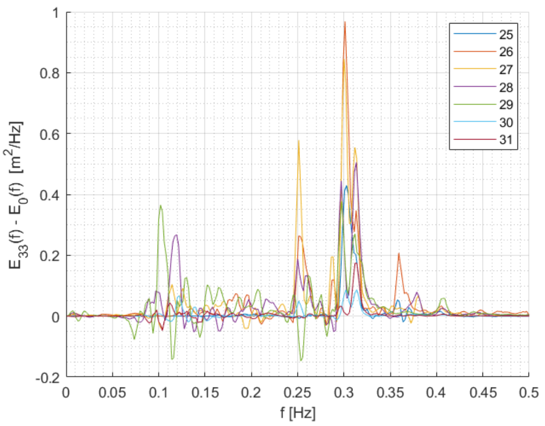

Figure 6.2: Difference in variance density $E(f)$ for the incident wave spectra of the calibration test E_0, and the tests with the full system of 33 floater arrays present E_{33}, as a function of the frequency f. Shown for all 7 irregular wave conditions tested; each test-ID in the legend corresponds to the different irregular wave characteristics tested, given in Table I.2.

The additional incident wave energy $\mathrm{E}_{33} - \mathrm{E}_0$ was between 7% and 13% of the total incident wave energy E_0, and shows to be present especially around $f = 0.3$ Hz and $f = 0.25$ Hz (which correspond to $\lambda/L_f \approx 1.45$ and $\lambda/L_f \approx 2$). These extra waves in the forward propagating wave spectrum cannot be explained by the resonance frequency of the mooring system, as the wave frequencies for which the spectrum showed an increase did not match the resonance frequency ($f_r \in [0.05, 0.12]$ Hz, depending on the size and therefore mass of the floating system). Neither did the wavelengths correspond to possible radiation modes of the floating structure (because for $f = 0.3$ Hz, $\lambda/L_f \approx 1.45$, $\lambda/W_f \approx 0.9$).

The additional waves might have been caused by the ARC, which performed active dampening incorrectly, causing the reflected waves to propagate back towards the structure. In this explanation, it might seem peculiar that the additional wave energy shows for certain frequencies only. This could be explained by frequency-dependence of the system reflection, rather than the reflection from the ARC. Namely, if waves with $f = 0.3$ Hz are often redirected backwards towards the wave paddle, and the ARC is not able to dampen them out, they will show up in the spectra as additional incident wave energy.

6.1.3. Time series analysis

For the regular wave tests, the time series analysis was done with the least squares method as explained in Appendix J, based on [29]. This analysis could have included errors, resulting in different values for the wave heights H_{p1}, H_{p2}, H_{r1} and H_{r2}.

The harmonic modes which are fitted to the surface elevation data are defined for a fixed frequency ω and its higher harmonics. If the wave phase does not propagate with the initialised ω through the entire flume, the backward propagating signals H_{r1} might be out of phase with the forward propagating signal H_{p1}, such that the least squares method does not work accurately. This could happen if the wavelength and thus frequency is not constant along the flume, for example because it is deformed when passing underneath the structure. This could be checked by adding pressure sensors in the flume underneath the structure.

The choice of the time interval for which the surface elevation data was analysed and the possible wave amplitude variations between the wave height meters could have had influence on the wave height results as well. Variations in time interval did not lead to different results however, and the difference in surface elevation between the wave gauges was estimated at maximally 1.1%.

6.1.4. Reflection analysis

To see whether redirection of waves by the floating system could explain the decreased wave transmission, the reflected waves from the front of the floating structure were filtered out (see section 4.1.2).

The definition of the reflection coefficient K_r that followed could be questioned based on the following three observations. Firstly, in around half of the regular wave tests analysed, slightly negative values $K_r \in [-0.04, 0]$ were found, which does not have a physical interpretation (see Figure 4.7). Secondly, the reflection parameter K_r showed variations of ± 0.03 with respect to the expected value $K_r = 0$. These values seem small, but when considered as a minimal error bar in comparison to the values $K_r \in [-0.04, 0.18]$, the error percentage is quite significant. Thirdly, the reflection coefficient showed not to explain the lack of wave transmission, as energy analysis gave $K_t^2 + K_r^2 < 1$ for the higher frequencies especially (see Figure 4.8). This would indicate the dissipation coefficient $K_d = \sqrt{1 - K_t^2 - K_r^2}$ to be highly frequency dependent, which is questionable to this extent. The shorter waves might indeed suffer more from friction effects, as also showed for the friction from the sides of the flume. However, the long waves would have $K_d \approx 0$, which shows a large range of difference between $K_d \approx 0.84$ for the shortest wave condition tested.

Therefore, one could reconsider the definition and derivation of the reflection coefficient, given in equation (4.9). Because the reflections from the floaters H_r might be small, the errors made in the assumptions might not be negligible in comparison to the wave signal of interest. The two contributions that should be looked at critically are the reflections from the wave paddle and the second order reflections from the back of the flume.

1. The reflections from the back of the flume were known to be around 30%, thus in second order maximally 9% (if the reflected waves are redirected fully again towards the wave dampener). This is a significant value in comparison to the reflections from the floating solar system, as these are of the same order of magnitude. In future research, addition of these second order effects could give a more accurate expression for K_t, but would require a larger system of equations to be solved. Notice that the reflections have to be truncated at some point, but that the effect of increasing the order of reflections included could be investigated.
2. The reflections from the wave paddle were minimised by using the wave paddle's ARC: the reflected waves are measured and actively dampened out. This device might not have worked perfectly however, especially for the short waves. For example, it took around five minutes for the water to become still again after a (regular) wave test was performed, so the waves had to pass through the flume a number of times until they disappeared.

Both of these contributions were assumed to be negligible and thus set to 0 in the system of equations that was solved for K_r. However, if they are of the same order of magnitude as the variable of interest, this could have caused errors.

Another way of filtering out the reflections from the floating object is by looking at the time series data for $t < t_{ref}$, where t_{ref} is the time it takes for the waves to travel towards the end of the flume and back to the first set of wave gauges. This time window is therefore free from reflections from the back of the flume and shows reflections from the object only. When this method was applied, the calibration tests already showed a backward propagating wave of the same order of magnitude as the tests with a floater present, which was not expected. The reflected wave heights were all in the order of millimetres, thus small in comparison to the incident wave height $H_i \geq 0.04$ m. Possibly, errors in the time series analysis could make it difficult to filter out the reflected waves. It should be noted that this approach would not measure the wave response of the equilibrium state of the system, because the oscillation movement of the floaters still changes in time.

Besides the uncertainty in the reflection parameter, it should be noted that all backward propagating waves were now defined as reflected waves. However, waves that propagate in opposite direction can also be caused by radiated waves from the oscillations of the structure. No distinction has been made between these possible causes for the redirected waves, as both are caused by linear effects and could therefore potentially be captured in a linear BEM model. It would however be interesting to see what the transmission would be when considering reflection only, because only scattering is implemented in the numerical model at this point. The distinction between radiative and reflective effects is difficult to measure, but analysis on the movement of the floating structure could be helpful in distinguishing radiative modes.

6.2. Numerical model

For the transmission analysis from the numerical model, presented in chapter 5, the most important points of discussion are:

- Numerical errors and memory limitations
- The influence of three-dimensional diffraction effects
- Definition of transmission and reflection coefficient for space-dependent surface elevation

The numerical errors and memory limitations are effects that are inherent to the BEM diffraction model, whereas the other two are discussion points regarding the approximate 2D transmission analysis. These three effects will be discussed sections 6.2.1-6.2.3.

6.2.1. Numerical errors and memory limitations

From the mesh sensitivity study, it could be concluded that the wave surface elevation results still included a normalised root mean square error of 1-2%, depending on the incident wavelength. This indicates that the model has not yet converged numerically, and choosing a higher resolution would lead to more accurate results. However, the ratio between the (large) wetted surface area and the (small) grid size resolution needed brought large memory and computation costs. Especially when trying to approximate a two-dimensional setting by using a very wide floating object, the number of grid cells increases. For the finest resolutions possible in a single direction, numerical errors cannot decrease further than the order of magnitude of 10^{-3} due to memory restrictions. This gives an indication for the numerical error bounds on the 2D diffraction results when a floating object of these dimensions is considered.

These mesh resolutions were compared to other studies that modelled wide floating breakwaters.

- Biesheuvel (2013) [5] modelled a floating barge with the dimensions $2 \times 350 \times 0.67$ m (below the equilibrium water level) using the linear BEM diffraction model Ansys Aqwa. In total, 5862-17550 panels were used to describe the 1171.68 m^2 wetted surface area. This translates to grid cells of 0.07-0.20 m^2, which were enough to describe waves with $\lambda \geq 8$ m.
- Nguyen et al. (2021) [51] modelled a floating barge with the dimensions $20 \times 10 \times 200$ m (below the equilibrium water level) using a non-commercial linear BEM diffraction model. Grid cells of 4 - 25 m^2 were used to describe waves with $\lambda \geq 30$ m. In this study, eight-node linear serendipity elements were used in discretization.

The average mesh size used to describe the 2D floating solar body in this study was 0.42 m^2, where the largest mesh cells in the x, y-plane had a surface area of 0.93m^2 to describe wavelengths up to $\lambda \geq 17$ m. This shows the grid cells were larger than the ones used in Biesheuvel (2013) and might therefore include more numerical errors. The maximum amount of panels is 18000 in Ansys Aqwa, which indicates that the commercial Aqwa code has less memory limitations than Capytaine. Nguyen et al. (2021) used different a different type of grid cells, which likely allowed for faster convergence. It was difficult to compare numerical errors however, as the studies only included plots that showed the transmission coefficient for different mesh sizes to show that the solutions had converged. In future studies, other numerical diffraction models could be considered, as they can either include more grid cells in the computations or use higher order elements. This will be discussed further in section 6.5.

A difference in comparison to the floating breakwater studies was the shape of the grid cells. These were not chosen to be square shaped, due to the small height of the floating object. Dividing the floater draft into a fine mesh lead to grid sizes in z in the order of 10^{-2} m, whereas the grid size in x and y were chosen in the order of 1 m due to the large object dimensions and memory restrictions. Therefore, the grid cells were rectangular shaped, with a high aspect ratio. It should be researched further whether a high aspect ratio could lead to additional numerical errors, as the mesh convergence in x and y-direction showed different from the z-direction. Indications that problems might arise for thin elements in Nemoh were found in for example [54]. In general, problems related to thin BEM elements arise in research on acoustics or elasticity theory when the thickness-to-length ratio is in the order of 10^{-6} or 10^{-9} . For the floating structure, as well as the grid cells for its mesh, the thickness-to-length ratio is always larger or equal to 10^{-4}, therefore not in the regime considered.

6.2.2. Three-dimensional diffraction effects

Results in section 5.3.3 and Appendix F showed that there were three dimensional effects present in the surface elevation, whereas a two dimensional situation was aimed at. The waves diffract around the structure, which causes a different wave amplitude pattern behind the floater compared to a fully two-dimensional simulation. Also, the standing waves in front of the structure will diffract wave energy to the sides, leading to a decrease in standing wave amplitude in comparison to a fully two-dimensional situation. Note that these 3D effects might be undesired in this research, they would be essential in describing a realistic offshore situation. This discussion should therefore not be regarded as inherent to applying a numerical BEM method to an offshore floating solar system, but reflects on the two-dimensional transmission analysis performed.

Especially the long waves will bend around the structure, because the width-to-wavelength ratio W_f/λ is smaller. However, increasing the width of the floater would require a larger number of grid cells to obtain the same resolution. Therefore, a balance was chosen between the memory and computation costs on the one hand and the width of the floater on the other hand.

For the wave conditions considered, the floater width to wavelength ratio was $W_f/\lambda \in [1.6, 11.8]$. The Sommerfeld solution for diffraction around a semi-infinite breakwater can give an indication of the amount of diffraction influence on the resulting wave height. Figure 6.3 shows the diffracted wave height around and behind a breakwater. Note that this breakwater is not floating but fixed over the entire water depth, and thus fully blocks the incident waves.

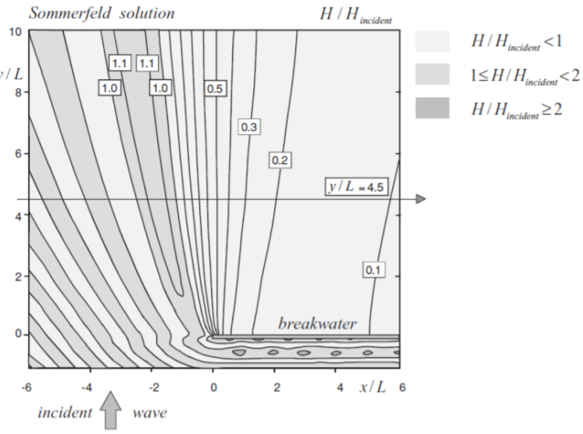

Figure 6.3: Sommerfeld solution for the diffracted wave height over incident wave height around a semi-infinite breakwater. [28]

The Sommerfeld solution shows that the diffracted wave height that bends around the structure is below 20% of the incident wave height for $W_f/\lambda > 1$. However, the floating object in this thesis has diffraction around both ends, and could therefore have a diffracted wave height that is up to 40% of the incident wave height. For the longer waves where $W_f/\lambda > 5$, it follows that the diffracted wave height is maximally 20% at the centre of the floater (for $y = 0$). Indeed, the differences in surface elevation between nodes and anti-nodes behind the object were largest for the longer waves, in the order of 0.25 m. It can be concluded that for the swell waves with large wavelengths (for example $T \approx 20$ s, $f \approx 0.05$ Hz, $\lambda \approx 280$ m), a very wide floater (W_f in the order of 10^4 m) is required to minimize the diffraction effects to 20%, which is still a high contribution.

The three-dimensional effects influence the surface elevation, and therefore the transmission and reflection coefficients, up to around 20%. This was estimated from the surface elevation differences in the interference patterns behind the floater. The values for the nodes and anti-nodes can become more extreme when waves from different directions interfere and add up, causing the surface elevation amplitudes in front of the floater to be larger than 2, $|\phi_I + \phi_D|_{x<-L_f} > 2$, or behind the floater to be larger than one $|\phi_I + \phi_D|_{x>L_f} > 1$.

6.2.3. Definition transmission and reflection coefficient

The chosen definitions for the transmission and reflection coefficient will be discussed separately first, after which the energy conservation $K_t^2+K_r^2$ is analysed to provide a reference for these choices. Again, this discussion reflects on the two-dimensional transmission analysis performed, and is not inherent to applying a numerical BEM method to an offshore floating solar system.

Transmission coefficient K_t

Because the surface elevation amplitude behind the object $|\eta_I+\eta_D|$ is dependent on the position (x, y), the definition of a valid transmission coefficient is not trivial. Using the average surface elevation value over an area of interest gave an adequate idea of the overall attenuation performance, and has been commonly used in breakwater studies, for example [49, 55]. Also, the undesired 3D diffraction effects were averaged out in this definition and therefore had a smaller impact on K_t. It should be noted however, that the transmission might only be smaller or equal to this value in a part of the area of interest.

The area of interest for the floating solar structure was defined as the first 100 m behind the object, in the direction of wave propagation. Only the wave height at $y = 0$ was considered, as a two-dimensional situation was approximated. The averaging domain was chosen as close to the floater as possible, to reduce the influence of three-dimensional diffraction effects. Still, there were variations in the surface elevation due to these interference patterns behind the floaters. The combination of a fixed area of interest and 3D effects which depended on the incident wavelength could thus have lead to an additional error in K_t, because the surface elevation oscillations were cut off at a fixed point. In future research, it might therefore be better to define the area of interest with respect to the incident wavelength λ.

Other definitions for a representative three-dimensional transmission coefficient were suggested by Nguyen et al. (2021) [51], for example using the maximum surface elevation value. This would yield an upper bound on the wave heights behind the object, which could be beneficial from a safety point of view. In a multi-use context, this seems like the value of interest for the possible limit state of the seaweed farm or harbour entrance. However, the 3D diffraction effects that caused the high-valued anti-nodes were not realistic, as a 2D setting was simulated. When a three-dimensional floating solar system is modelled, this could be a suggestion for defining K_t.

Reflection coefficient K_r

The reflected wave height H_r used in the definition for the reflection coefficient K_r was defined as local maximum of the surface elevation $|\eta_D+\eta_I|$ in front of the structure, minus the incident wave amplitude $|\eta_I|$. The anti-node closest to the floating object was taken as a representative for H_r because the three-dimensional effects were smallest. However, this choice could be reconsidered based on the following discussion points.

Firstly, the standing waves in front of the structure did not show constant values for the surface elevation at the anti-nodes. In fact, for the higher wave heights, the first standing wave amplitudes showed alternation between two values in the region close to the structure $x \in [-100, -L_f]$ (see Figure F.1e, Appendix F). The value closest to the object was often the higher peak value, which was then used as the measure for K_r (see section 5.1.6). This might have lead to an over-estimation of K_r. For the higher frequencies f, the difference in surface elevation between the first and second anti-node were largest, and might thus have caused a bigger error.

Secondly, the reflected wave height increased to $H_r > 1$ for the frequencies $f > 0.25$, which would never be observed in a two-dimensional basin test. It is unclear what exactly caused the high surface elevation $|\eta_D+\eta_I|$ near the object boundary. It could be that the translation from the velocity potential solution on the object surface to a grid cell near this surface creates errors.

Energy conservation $K_t^2+K_r^2$

Because the diffraction model is entirely based on linear wave theory, wave energy should be conserved. That is, the wave energy that was not transmitted had been reflected or diffracted in different propagation directions. When the problem would be entirely two-dimensional, only reflection would occur. The sum of the squared transmission and reflection coefficients, shown in Figure 5.6, did not show $K_t^2 + K_r^2 = 1$ as would be expected in a two-dimensional situation. Therefore, the numerical transmission and reflection results might not be one-to-one comparable to the 2D wave height measurements for basin tests. Within the frequency domain of interest, the values $K_t^2 + K_r^2 \in [0.9, 1.3]$ show a reference setting for the entire analysis. The fact that the sum is higher than one and also shows variability over the frequency domain f indicates one should be critical in using this method to predict two-dimensional transmission and reflection through a floating solar structure.

6.3. Comparison of results

To see whether the scattering solution of the linear BEM diffraction model can be used to predict two-dimensional transmission through the floating solar structure, the results from the basin test (chapter 4) and the diffraction model (chapter 5) will be compared in this section.

The transmission, reflection and flume dissipation coefficients, K_t, K_r and $K_{d,f}$, are plotted as a function of the incident wave frequency f [Hz] in Figure 6.4, for the basin test and the numerical diffraction model. Recall that these results are all determined with incident wave height $H = 1$ m on offshore scale, and a water depth of $h = 21.25$ m in the basin test and $h = 24$ m in the numerical model. The coefficients were determined for each frequency separately, for (approximately) linear waves. The basin test results were averaged over the different system size configurations n_{FL}, numerical results had $n_{FL} = 1$.

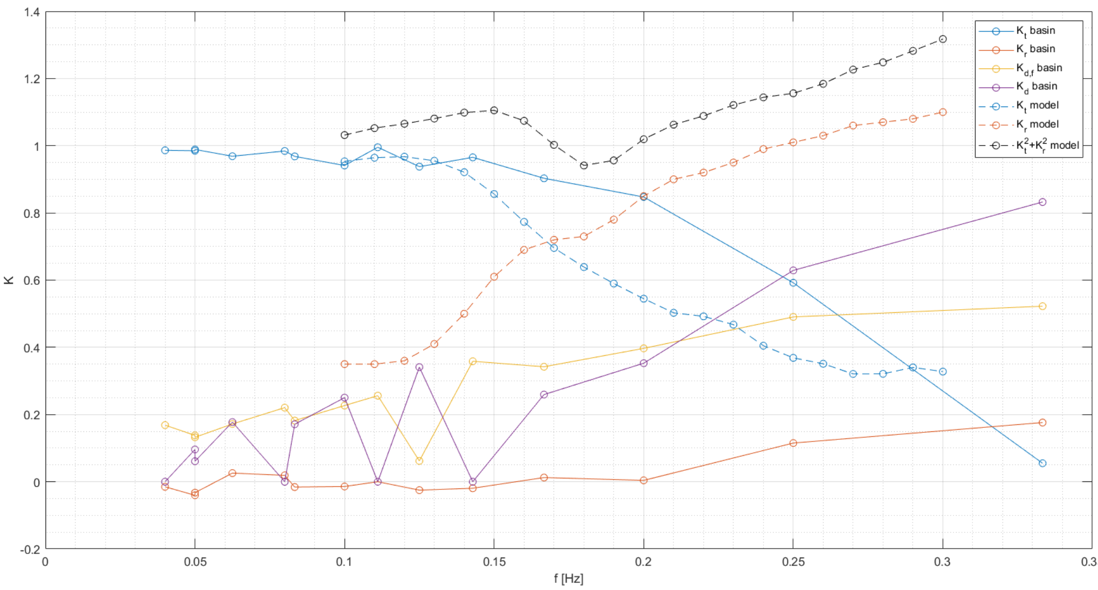

Figure 6.4: Transmission K_t, reflection K_r and flume dissipation $K_{d,f}$ and model dissipation K_d coefficients from the basin test, as a function of incident wave frequency f [Hz], shown with the solid line. Transmission K_t, reflection K_r, and squared sum $K_t^2 + K_r^2$ coefficients from the numerical diffraction model, as a function of incident wave frequency f [Hz], shown with the dashed line. Configurations and wave conditions as described in Figures 4.8 and 5.6.

Qualitatively, the overall trends for the transmission and reflection results do confirm frequency dependent behaviour: transmission decreases with f and reflection increases with f. Furthermore, a decrease in transmission seems to start around a similar frequency value $f > 0.14$ Hz.

Quantitatively on the other hand, the values for K_t and especially K_r show large differences between the basin test and model predictions. Reflection is overestimated by the diffraction model, whereas transmission is underestimated. It was not necessarily expected that the model and basin test results would show good agreement, as the model was limited to the scattering result only. The radiation and dissipation effects that were present in the flume are not included in the model simulations.

Dissipation showed to be accountable for the largest part of the decrease in transmission, based on the regular test results. Although there are errors in the reflection analysis, it is likely that the share of dissipation effects is not negligible. Therefore, a numerical boundary element method diffraction model might not be able to predict the exact wave transmission through an interconnected multi-body solar structure.

However, using the complete linear description of the wave-structure interaction by adding the radiation effects might bring the transmission predictions closer to the basin test observations. It is expected that adding radiation effects could increase transmission and reduce reflection in the model results, which would bring them closer to the test observations. Also, because the model results were influenced by three-dimensional effects and a space-dependent transmission, the values for K_t and K_r from the model results would shift quite a lot depending on the choices for floater configuration and coefficient definitions. A three-dimensional model approach might give results that resemble 3D test results or offshore observations more accurately.

The diffraction results could better be validated with other studies that compute the diffracted wave field, such as Nguyen et al. (2021) [51]. Although this study did include two plots where the diffraction results were isolated, there were no numerical transmission values that could be taken as a reference solution. Also, the draft of the floating breakwater was incomparable with the floating solar platform used in this study. Similarly to most other floating breakwaters studies, mostly the results for the combined diffraction and radiation solutions are presented. The diffraction results available showed similar interference patterns and surface elevation values to the results presented in this study. Therefore, the overall effects are confirmed.

6.3.1. Model assumptions

Remember that the assumptions which underlie the linear potential flow theory, stated in section 2.2, should hold for the diffraction model. If these assumptions differ significantly from the basin test setting, this can be a cause for the differences between the obtained results. In this light, especially the validity of the small amplitude approximation could be questioned. This assumption implies airy waves as well as no overtopping over the freeboard or air gaps below object.

Airy waves

The computations of the linear diffraction model are based on the small amplitude approximation: the wave amplitudes should be small compared with their wave length λ as well as the water depth h. Because the model is linear, the surface elevation results can be scaled to match any input value for the incident wave height (in case of the scattering problem) or the radiation amplitude of the object (in case of the radiation problem). Therefore, the model solutions might not give an appropriate description of the physical waves for the incident wave amplitude A=1 m that was used because offshore or basin-test waves might not be airy in this regime, especially for the smaller wavelengths.

Because the diffraction model assumes linear waves, a better comparison can be made if the basin test conditions were also chosen as airy as possible. The ratios H/λ and H/h were kept as small as possible for the regular wave tests, but were restricted by the minimal wave height in the Scheldt flume of $H = 0.04$ m. To verify how well these waves can be approximated with linear wave theory, the validity regimes of different wave theories are shown in Figure 6.5 [27, 35]. The dimensionless parameters H/gT^2 and h/gT^2 were calculated for the regular wave test conditions and have been plotted as red '+' marks.

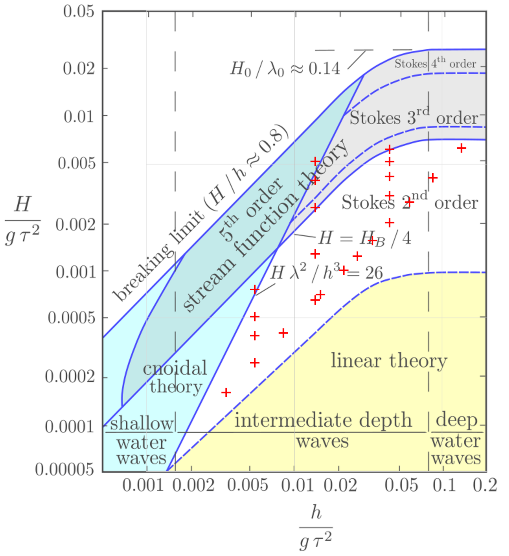

Figure 6.5: Regions of validity for various theories which describe periodic water waves. Defined in terms of dimensionless wave height parameter H/gT^2 and depth parameter h/gT^2. [35] Regular wave test conditions are plotted as red '+'. Tests 10 and 15 have been indicated with a square and circle respectively, their wave spectra are shown in Figure 6.6.

From this figure, it is clear that most of the wave conditions that were tested are best described with second order Stokes theory and are therefore weakly non-linear. When spectral analysis was performed on the regular wave measurements, the wave spectrum only showed a non-zero variance density for the desired frequency f in most cases. Therefore, the presence of the higher harmonic modes was limited. As an example, the wave spectrum for test 15 (encircled in Figure 6.5) is shown in Figure 6.6a below. Only for the wave conditions with increased wave height, small excitations for the higher harmonics showed as well. Figure 6.6b shows an example of a variance density spectrum that did include the first and second higher harmonics, for test 10 (shown with a square in Figure 6.5). Notice that the higher harmonics are indeed located at $2f$ and $3f$, with f the main incident wave frequency.

Recall that only the tests with constant wave height $H = 1.0$ m (offshore scale) were used in the calculations of $K_t(f)$ and $K_r(f)$. Because these all lay in the Stokes second order regime and show almost no higher order excitations in the wave spectrum, the basin test waves were close to airy and can therefore be used as comparison for the linear numerical results.

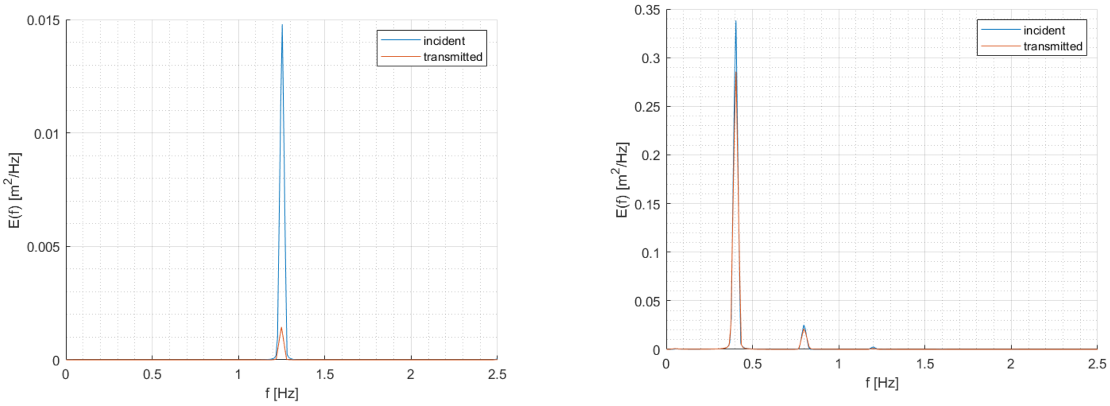

(a) Regular wave test 15: $H = 1$ m, $T = 4$ s, $\lambda = 25$ m at offshore scale

(b) Regular wave test 10: $H = 8$ m, $T = 12.5$ s, $\lambda = 156$ m at offshore scale

Figure 6.6: Incident and transmitted variance density spectra E [m^2/Hz] as a function of the wave frequency f [Hz] for two regular wave tests, with the largest system size $n_{FL} = 33$.

It can also be observed from this figure that there is no frequency spreading present caused by the floating solar system. The incident variance density is decreased, but there are no waves of different frequency formed in the transmitted spectrum. The absence of physical effects that spread incident wave energy over different frequencies does show agreement with a linear diffraction model, which considers one frequency at the time.

Overtopping and air gaps

Because the height of the floating solar platform is relatively small, scaling the wave amplitude to A=1 m might misrepresent the wave-structure interaction. The small amplitude approximation for linear wave theory implies that wave will not flow over the structure's freeboard or that no air gaps are formed underneath the structure. Namely, the velocity potential is calculated with a very small surface elevation displacement, therefore also small with respect to the object height. However, in the basin test and for the offshore wave conditions, the small freeboard would lead to overtopping and the limited draft will allow for air gaps underneath the floater. These effects are illustrated in Figure 6.7, and are examples of effects that cannot be described by the linear diffraction model.

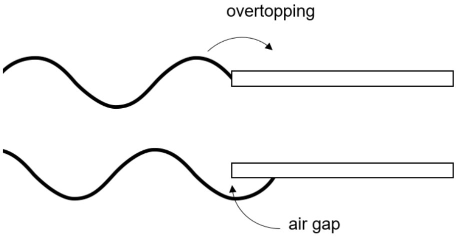

Figure 6.7: Illustration of two effects that are not simulated in a linear boundary element method diffraction model.

6.4. Implications for offshore floating solar

In the multi-use context, if would be beneficial if the floating solar structure has a wave attenuation effect such that other offshore activities can benefit from the possible shadow zone leeward of the structure. In short, the basin test results showed that the structure acts as a wave follower for the long waves. Therefore, the low frequent wave energy is transmitted. From a certain frequency onwards, $f \leq 0.15$ Hz, depending on the ratio between the wavelength and the rigid parts of the structure, the wave energy is attenuated.

Irregular wave tests that simulated the North Sea wave conditions showed wave energy attenuation between 37% and 9% when the largest floating system was present. This percentage depended on the wave conditions tested (T_p and H_s) and was corrected for the flume dissipation. The system has a large impact on the waves for very calm sea states with short wave period and low wave height. When a weighted average is computed with respect to the occurrence of the tested sea states at the North Sea location [1], the total amount of wave energy attenuation is approximately 27%. This is true if waves would always be propagating in parallel with the length of the rigid floaters and cannot move around the object on the sides. Therefore, the percentage can be interpreted as a maximal value for wave attenuation at the North Sea offshore location. The transmitted wave spectra will still have a lot of large waves however, and the smaller ones will be filtered out.

At the current North Sea location, for a water depth around 21 m, the structure might not have the attenuation performance that is desired for a breakwater to protect other offshore activities. Seaweed farms and harbours will have to be protected from the waves with largest wave heights especially, because these can cause most structural damage. As the wavelength and wave height are highly correlated in the North Sea conditions and the long waves were transmitted by the system, this means the roughest sea states will be influenced to less extent by the floating solar structure.

The structure's wave attenuation properties might however be well suitable for other locations, either offshore or on inland waters. If the most common wave spectrum consists of waves with shorter wavelengths, the attenuation performance would be better. The floating solar farm will likely have more impact on the wave environment in North Sea locations with a lower water depth, where the waves are shorter, or at for example Mediterranean seas where the smaller fetch also leads to smaller wavelengths. Furthermore, for applications where it would be convenient to filter out the short waves especially, the system would be well suitable for multi-use.

In addition, the wave-structure interaction also shows that the system itself will have to endure less structure loads in comparison to an actual floating breakwater. Namely, if the structure is able to move along the waves and does not decrease the wave energy as much, this indicates that forces on for example the mooring lines or the interconnectors that hold the platforms together are not increased by opposite forces acting on the system.

6.5. Further research suggestions

In this research, first conclusions were found on the wave attenuation by an interconnected multi-body solar structure. Now that the global effects are clearer, it would be beneficial to have a model which predicts the wave environment around an interconnected multi-body floating solar system accurately. It could especially be valuable for design purposes and the predictions for large-scale systems, which are difficult and time-consuming to test in a basin test for example. A numerical model would be easily adaptable for other system configurations and floater dimensions, as well as different incident wave characteristics and water depth. The first steps were done in this direction by showing a proof of concept for applying a linear boundary element method diffraction model to model the wave interaction with the floating solar structure. The scattering solution was used to obtain wave transmission in an approximately two-dimensional setting. The limitations that arose in this approach have been discussed previously and bring incentives for four main further research directions, which will be discussed below. Notice that the list of discussion points included in Appendix M gives a list of suggestions for research improvements as well.

Including the radiation solution

The first and foremost step in modelling the wave transmission more accurately, is by including the linear velocity potential radiation solutions in the model. This will complete the linear description of wave-structure interaction, such that all first order effects are included. Because this allows the floating object to move, the increased transmission for the structure's radiative modes could be simulated. Overall, including radiation effects will likely increase the transmission, as waves will be able to pass underneath the structure and resonant motion modes can be simulated. After these modification, the diffraction model results could perhaps be validated with the basin test wave transmission.

In order to include the radiation effect in the surface elevation amplitude, a Response Amplitude Operator is needed to combine the radiation and diffraction potentials into a total surface elevation field $\eta_I + \eta_D + \eta_R$. This RAO is an operator that represents the motion amplitude per unit wave amplitude and the phase difference between the object and the water motion. Capytaine can solve for this function in each desired degree of freedom, such that the body motion is simulated. The object's mass and hydrodynamic stiffness matrices are needed as additional input, see Appendix C. A stiffness matrix for mooring stiffness and an operational dissipation matrix may be added to the equation of motion as well. For a restrained object, the degrees of freedom could be limited. In case of the offshore floating solar structure, heave is expected to be the main oscillation mode and therefore the most important degree of freedom to add to the diffraction solution.

Solving the memory limitations

The second suggestion regards the numerical diffraction model limits due to the memory needed for the interaction matrix. New approaches that could be explored to minimise memory usage and decrease computation costs could be using a hierarchical matrix approximation, where the interaction between grid cells that are far apart will be disregarded, or using different boundary elements, such as higher order panel methods [51] or B-splines [13]. Some of the commercial software available (WAMIT, Ansys Aqwa) are likely to have one or both of these options available already, so it would be relevant to verify the diffraction results and see if they show better performance.

Solving this memory problem is relevant in the first place for simulating a wider floater or to include side walls, such that two-dimensional results can be approximated in a better way. It is also required to simulate a 3D offshore solar structure however, because increasing the number of rigid bodies within the structure will lead to a large number of grid cells as well. With the resolutions used in this research, modelling a floating solar structure with more than 40 platforms (sized $12 \times 2 \times 0.33$ m) is not possible. With respect to the 1MW system that Oceans of Energy is developing at the North Sea in the coming years, which consists of over 200 platforms, this limitation makes the diffraction model as it is unsuitable to predict the system's wave environment. Hierarchical Toeplitz matrices could be implemented in Capytaine, where the interaction between grid cells that are far apart will be disregarded. It can be assumed that the floaters that are very far apart will not be influenced by each other as much.

Determining the share of influence by reflection, radiation and dissipation
The third research suggestion would be to investigate the share of influence of reflection, radiation and dissipation on the wave transmission further. The cause for a decreased transmission is important to see whether a linear model will be able to capture the most important effects. It was difficult to indicate what the relative influence was from reflection effects versus the radiation and dissipation effects, which would have been helpful to give a reference frame or expectation for the numerical results. From the basin test results, it seemed as if dissipation effects were at least equally important as the linear wave-structure interaction and can therefore not be neglected. However, these results were not entirely conclusive because of possible errors in the reflection analysis and the small amount of tests that were done in the high frequency regime where $K_t < 1$. This analysis should therefore be improved, for example by choosing a different scale and setup such that the regime around $\lambda/L_f \approx 2$ can be tested extensively or deriving the reflection coefficient with a different method. If the influence of the higher order dissipative effects is similar to the linear effects, non-linear descriptions might be needed to model wave transmission. Implementation could be difficult within potential flow theory, but combining linear wave theory and dissipation effects is done before in research on wave energy converters, for example [7, 47].

Including diffraction model solutions into a spectral wave model
Finally, once the diffraction model results can provide an accurate description of the near-field wave surface elevation, it would be relevant to look how the effect of the floating solar structure could be implemented in a spectral wave model such as SWAN. This would enable the inclusion of far field effects for a large solar farm in a large North Sea wave model, such that possible effects on the sea and coastline environment can be predicted. The interaction between linear diffraction results and a spectral domain model will likely entail a redirection term for the wave energy that is frequency dependent, possibly in combination with a sink term to simulate dissipation effects.

7

Conclusions

The overall aim of this thesis was to research the effect of floating solar on the surrounding wave field. If waves would be attenuated by the solar structure, down-wave shadow zones could be useful for offshore multi use. The transmission of waves through an interconnected multi-body floating solar structure was studied in a two-dimensional setting, with a basin test and a numerical model. The two research questions that were posed will be answered in this conclusion.

To come back to the overall research aim first, the effect of an interconnected multi-body floating solar structure on the wave transmission showed to be large for short waves and small for long waves. The short waves are attenuated, which leads to a decrease in transmitted wave energy. Therefore, the floating solar system will form a down-wave shadow zone if the incident wave spectrum consists of waves with short wavelengths.

For the wave conditions at the North Sea location, with a water depth around 21 m, the average decrease in wave energy was found to be maximally 27% for a 400 m long system. Because the highest waves with largest wave loads are in the transmission regime however, the structure might not have the breakwater performance that is desired to protect other offshore activities at this location.

1. How do wave transmission and wave reflection depend on the incident wave frequency (and thus wavelength), the incident wave height and the number of rows of floaters the model consists of?

Wave transmission showed to be highly dependent on the wave frequency f and thus the wavelength λ in the basin test results. The floating solar system acted as a low pass filter: it lets the low frequency waves pass through, whereas the waves with higher frequency are attenuated by the structure. The system consists of multiple rigid floaters, which have a length L_f in parallel to the incident waves. From a wavelength smaller than six times the floater length onwards, $\lambda < 6L_f$, the transmission decreased linearly as a function of f. For the very short wavelengths $\lambda < 2L_f$, waves were almost fully attenuated such that $K_t \approx 0.1$. This behaviour was expected, as the structure is not able to follow the wave surface elevation if the rigid parts are large in comparison to the wavelength. Only if the wavelength was exactly twice the floater length, $\lambda = 2L_f$, there was an increased transmission in the wave spectra due to the oscillation mode of the floaters. In this case, the rigid bodies can follow the waves well and transmit a larger share of the incident wave energy.

The wave height and the number of floater rows the model consists of had less impact on the wave transmission. Transmission did not seem to depend on the incident wave height, but this was tested in the long wavelength regime only, where the floating system transmitted the waves regardless of their wave height. Transmission decreased linearly as a function of the number of floater arrays included parallel to the wave propagation, where the slope of this relation differed per wavelength tested.

Wave reflection showed to increase with frequency. In the basin tests, wave reflection showed for $\lambda < 2L_f$, but was more difficult to analyse because the reflections from the back of the flume had to be filtered out from the backward propagating wave signal. The diffraction model showed standing waves in front of the floating structure, caused by the interference of incident and reflected waves. Reflection increased for $\lambda < 7L_f$.

2. How well does the scattering solution of a linear boundary element method diffraction model describe the wave transmission through a multi-body floating solar structure?

Overall, the transmission and reflection analysis did show comparable, frequency dependent, qualitative results for the basin test and the numerical diffraction model. Quantitatively, the diffraction solution does not predict the transmission and reflection coefficients correctly.

(a) To what extent do linear effects, thus the redirection of wave energy, explain a decreased transmission?

This question was investigated by considering the energy conservation: the incident wave energy has to be either transmitted, redirected, which could be due to reflection or radiation, or dissipated by the floating structure. The basin test results showed that reflection did indeed increase when transmission decreased, but the transmitted and reflected wave energy were still smaller than the incident wave energy. If this difference is assumed to be caused by dissipation effects, dissipation showed to be dominant over the linear effects in the cause for wave energy attenuation.

The basin test results thus indicated that higher order dissipative effects are likely needed to describe the decrease in transmission accurately, especially for the higher wave frequencies. Therefore, a linear velocity potential diffraction model might not describe the wave transmission in an accurate manner. However, the reflected wave signal results which lead to this conclusion were questioned because the reflections from the back of the flume influenced the wave analysis. Therefore, an improved reflection analysis and further research on the dissipative effectswould be needed to conclude that wave transmission cannot be described with linear effects only.

(b) Can a linear boundary element method diffraction model be applied to a shallow multi-body floating solar structure?

The obtained solutions showed that the wave response around the shallow floating solar structure was in accordance with the physical expectations. When the mesh for the object was chosen correctly, the wave field around a simple floating object could be determined with the BEM diffraction model. However, two model limitations were found when applying the diffraction model to the floating solar structure.

Firstly, the ratio between the (large) wetted surface area and the (small) grid size resolution needed brought large memory and computation costs. With respect to the incident wavelength, the model setup required small grid sizes, to describe the surface elevation accurately and reduce numerical errors, and a large object width, to approximate a two-dimensional solution. For the final setup, there was still an average numerical error in the wave surface elevation of around 2%, which shows the diffraction results had not been fully converged. Memory requirements thus limit the resolution and object dimensions that can be simulated, because a maximum of 10^4 panels cells could be used to describe the object's wetted surface area. Possible solutions could lie in a hierarchical matrix approximation, where the interaction between grid cells that are far apart will be disregarded.

Secondly, the aspect ratio of the grid cells could have increased numerical errors when an object with small draft is considered. Dividing the small draft into a fine mesh lead to grid sizes in z in the order of 10^{-2} m, whereas the grid size in x and y were chosen in the order of 1 m, due to the large object dimensions and memory restrictions. This might have lead to numerical errors, as the mesh convergence in x and y-direction was different from the z-direction.

Using the scattering solution of a linear boundary element diffraction model as a prediction for wave transmission showed the following shortcomings in simulating the basin test results:

- Only first order effects are included, whereas higher order dissipation might be of similar or greater importance in decreasing wave transmission.

- Memory requirements limit the numerical accuracy and the dimensions of the object's wetted surface.
- The two-dimensional transmission results were influenced by thee-dimensional diffraction effects, in the order of 20%.
- The wave transmission was position dependent, because nodes and anti-nodes occur in the surface elevation. Therefore, converting the diffraction model results into a single transmission coefficient was not trivial and thus difficult for accurate comparison.
- When only the scattering solution is used, increased transmission due to the structure's oscillation modes will not be included. To describe the movement of the structure, the radiation part of linear velocity potential theory is needed as well.

Notice that the last three of these points are not shortcomings of the diffraction model, but of the two-dimensional analysis method.

A

Derivation of the wave spectrum

When analysing ocean waves, they are often described by a wave spectrum. The derivation of the variance density wave spectrum is given here, based on Holthuijsen (2007) [28].

An observation of the surface elevation is formally treated as a realisation of a stochastic process. Therefore, the realisation $\eta(t)$ at one specific location can be seen as a time series. This stochastic treatment is based on the random-phase/amplitude model.

Consider the moving surface elevation of an irregular sea state at a single location, $\underline{\eta}(t)$, which is a random variable.[1] In the random-phase/amplitude model, this surface elevation can be expressed in terms of a Fourier series; the sum of a large number of harmonic components. Each harmonic component has a constant amplitude and phase, which are chosen randomly for each realisation of the time record.

$$\underline{\eta}(t) = \sum_{i=1}^{N} \underline{a}_i \cos(2\pi f_i t + \underline{\alpha}_i) \tag{A.1}$$

where N is the total number of harmonic components, $\underline{a}_i$ is the amplitude, f_i the wave frequency and $\underline{\alpha}_i$ the wave phase. Each harmonic component describes an oscillatory motion with its frequency f_i. The amplitude spectrum and phase spectrum can be derived from Fourier analysis. When they are substituted into the Fourier series, the exact surface elevation record is reproduced.

The phase $\underline{\alpha}_i$ is assumed to be a uniform distribution over all phase angles in $(0, 2\pi]$. The amplitude spectrum is the one which characterises the wave record, and which will eventually lead to the energy density spectrum. It is assumed to be Rayleigh distributed.

$$p(\alpha_i) = \frac{1}{2\pi} \qquad \text{for } 0 < \alpha_i \leq 2\pi \tag{A.2}$$

$$p(a_i) = \frac{\pi}{2}\frac{a_i}{\mu_i^2}\exp\big(-\frac{\pi a_i^2}{4\mu_i^2}\big) \qquad \text{for } a_i \geq 0 \tag{A.3}$$

Here, the only parameter varying over the frequencies is the expected value of the amplitude $\mu_i = \mathbb{E}\{\underline{a}_i\}$. The statistical characteristics of the amplitude of harmonic component i are thus purely defined by this expectation. It can be approximated by taking the average over a lot of amplitude realisations of wave elevation records.

The amplitude spectrum is then defined as the expected value of the amplitude $\mathbb{E}\{\underline{a}_i\}$ as a function of frequency f_i. It is visualised in the upper graph of Figure A.1.

---

[1] Notation: an underscore will represent a random variable.

With the information of the amplitude spectrum, one can describe the sea-surface elevation realistically as a stationary, Gaussian process. However, the information can also be presented in a more relevant way. Namely, the statistical quantity of interest is actually the variance of this wave component amplitude $\mathbb{E}\{\frac{1}{2}\underline{a}_i^2\}$, shown in the second plot of Figure A.1. This is because of two reasons. Firstly, from the linear theory for surface gravity waves (see section 2.2) it can be concluded that the energy of the waves is proportional to the variance. Secondly, the variance is a quantity that can be added for various wave components; the sum of the variances of the wave components is equal to the variance of the sum of the wave components. Therefore, the variance spectrum will be considered instead of the amplitude spectrum.

Up to this point, the amplitude spectrum and the variance spectrum have been introduced as spectra based on discrete frequencies. At sea, the number of frequency components present will not be limited to N; all frequencies are present at sea. Therefore, a conversion has to be made from the discrete case to a continuous spectrum of frequencies. This is done in two steps. Firstly, the variance density is be defined by distributing the variance $\mathbb{E}\{\frac{1}{2}\underline{a}_i^2\}$ over the frequency interval Δf_i at frequency f_i:

$$E^*(f_i) = \frac{\mathbb{E}\{\frac{1}{2}\underline{a}_i^2\}}{\Delta f_i} \tag{A.4}$$

All frequencies are now included because they all fall into a frequency interval Δf_i, but the value is constant over this interval. In other words, the variance density is discontinuous from one frequency band to the next. A visualisation is given in the third graph of Figure A.1. The second step is therefore taking the limit of frequency intervals to zero, which makes the variance density spectrum continuous. The variance density spectrum is thus defined as

$$E(f) = \lim_{\Delta f \to 0} \frac{\mathbb{E}\{\frac{1}{2}\underline{a}^2\}}{\Delta f} \tag{A.5}$$

$E(f)$ describes the surface elevation of ocean waves in a statistical sense, as a function of time at one geographic location.

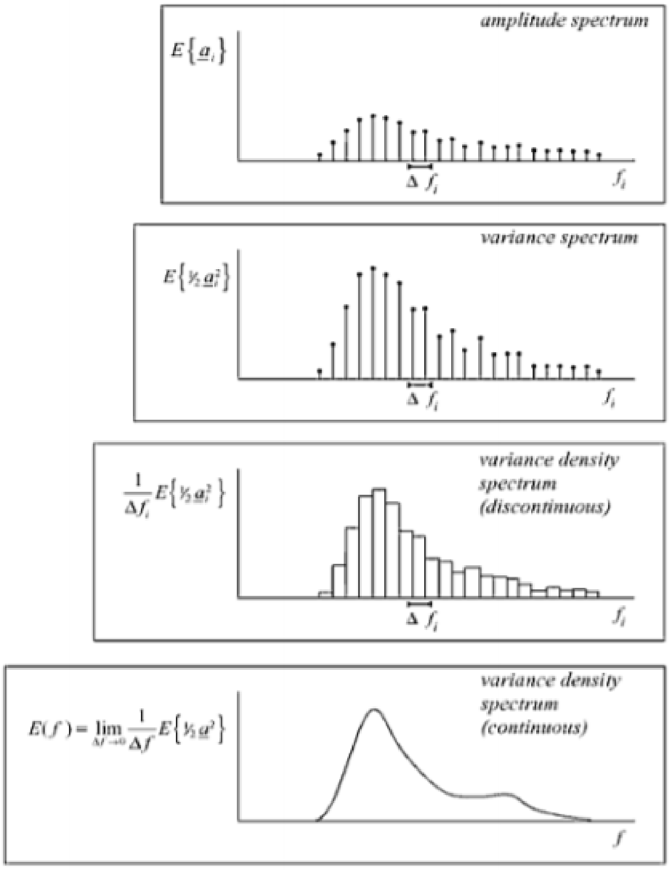

Figure A.1: Transformation of discrete amplitude spectrum of the random/phase amplitude model to the continuous variance density spectrum. [28]

The connection between the variance density spectrum and the actual wave characteristics can be made in two ways. Firstly, the connection between the variance density spectrum $E(f)$ and the total variance of the the surface-elevation $\overline{\underline{\eta}^2}$ is given by equation (A.6). This shows the degree of irregularity is determined by the width of the variance density spectrum. Namely, if $E(f)$ is a delta peak, the resulting surface elevation will be a harmonic wave. On the other hand, if the spectrum $E(f)$ is wide, the waves will show to be irregular, because they consist of a lot of harmonic modes together.

$$\overline{\underline{\eta}^2} = \int_0^\infty E(f)df \tag{A.6}$$

Secondly, the connection to a physical quantity can be made through the energy density spectrum. It is derived from the variance density spectrum by multiplying with ρg

$$E_{energy}(f) = \rho g E_{var}(f) \tag{A.7}$$

The assumptions of the random-phase/amplitude model and the cases for which these assumptions are justified are the following: [28]

1. The model generates a stationary [2] (Gaussian) process, which is only (approximately) true for real sea states when limited amount of time is considered.
2. Harmonic wave components are assumed to be independent from one another, which is not really the case for sea states because these components interact to some degree. If waves are not too steep and in not too shallow water, these interactions are weak enough to be ignored.

---

[2] A stationary process is a process for which all statistical characteristics are independent of time, but may still depend on time intervals. In other words, the a stationary process is a stochastic process whose unconditional joint probability distribution does not change when shifted in time.

Where the description of surface gravity waves above were for stationary, Gaussian surface elevation at one geographic location, three-dimensional moving waves can be described by adding an extra horizontal dimension. If the waves are not plane waves and the surface elevation depends on the angle of incidence θ as well, a frequency-direction spectrum can be defined. This spectrum includes the spread of waves over the frequencies and angles of incidence, but will not be needed in this thesis. For reading on the frequency direction spectrum, see Holthuijsen (2007) [28].

B

Derivation of the linear velocity potential theory equations

In order to describe surface gravity waves, two balance equations are central: the mass balance equation and the momentum balance equation. The linearised versions of these equations, together with boundary conditions, give a complete description of the waves in fist order. The linear wave theory, also known as the Airy wave theory, holds for waves where the amplitude is small in comparison with the wavelength and the water depth. The conservation equations are then expressed in terms of a velocity potential Φ to make computations easier, which results in the Laplace and the (linearised) Bernoulli equations. In this appendix, the derivations of these equations and their (linearised) boundary conditions are given, based on for example [28, 39].

It is important to first state the assumptions that linear velocity potential theory is based upon:

1. small amplitude approximation: the wave amplitudes should be small compared to their wavelength as well as the water depth
2. water is assumed to be an ideal fluid: incompressible, with constant density and no viscosity
3. water body is continuous, so there are no air bubbles in the water domain considered
4. free wave assumption: the only force acting on the water is gravity force (wind-induced pressure and surface tension are thus excluded)
5. water particles cannot leave the water surface, i.e. no splashing or wave breaking
6. water particles cannot penetrate the bottom of the sea

The equations for surface gravity waves in a finite (but deep) sea environment will be derived below.

The mass balance equation describes the mass conservation of an infinitesimally small water volume mathematically in the following way

$$\frac{\partial \rho}{\partial t} + \frac{\partial \rho u_x}{\partial x} + \frac{\partial \rho u_y}{\partial y} + \frac{\partial \rho u_z}{\partial z} = S_\rho \tag{B.1}$$

with ρ the water density, u_x, u_y and u_z the velocity of the water particles in x, y and z-direction. The first term on the left side of the equation shows the local rate of change in density, the other three terms show the effect of mass transportation. The term on the right hand side is called the source term, which would mean production of mass. Therefore, when assuming the density of the water is constant and there is no production of water ($S_\rho = 0$), the continuity equation follows from the mass balance equation:

$$\frac{\partial u_x}{\partial x} + \frac{\partial u_y}{\partial y} + \frac{\partial u_z}{\partial z} = 0 \tag{B.2}$$

Note that this equation is linear in the water particle velocities u_x, u_y, u_z.

The second equation considered is the momentum balance equation. Since momentum is a vector quantity, the momentum balance equation is composed of three equations, one for each direction. The momentum density is defined as $\vec{\mu} = \rho\vec{u} = (\rho u_x, \rho u_y, \rho u_x)$. The balance equation for the x-component will then become

$$\frac{\partial(\rho u_x)}{\partial t} + \frac{\partial u_x(\rho u_x)}{\partial x} + \frac{\partial(u_y \rho u_x)}{\partial y} + \frac{u_z \partial(\rho u_x)}{\partial z} = S_x = F_x \tag{B.3}$$

where S_x is the momentum source term in the x-direction. Production of momentum per unit time is by definition a force acting on the volume: force is the rate of change of momentum. Thus F_x is the body force in the x direction per unit volume (as momentum was also defined per unit volume as a density variable). Notice that the second to fourth terms on the left hand side of equation (B.3) are quadratic combinations of the water particle velocities and thus non-linear terms.

In order to make computations easier, the velocity potential function $\Phi(x, y, z, t)$ is defined such that:

$$u_x = \frac{\partial\Phi}{\partial x}, \qquad u_y = \frac{\partial\Phi}{\partial y}, \qquad u_z = \frac{\partial\Phi}{\partial z} \tag{B.4}$$

The assumption that the water is an irrational fluid is required for this auxiliary function Φ to exist. Now the conservation equations introduced above are translated in terms of this auxiliary function.

The continuity equation, Equation (B.2), stated the divergence of the velocity should be zero. This translates into the Laplace equation for Φ, which is

$$\nabla^2\Phi = \frac{\partial^2\Phi}{\partial x^2} + \frac{\partial^2\Phi}{\partial y^2} + \frac{\partial^2\Phi}{\partial z^2} = 0 \tag{B.5}$$

This equation can be solved for Φ when two kinematic boundary conditions are added (related to the motion of the water particles); Equations (B.6) and (B.7).

The surface elevation in vertical z direction is expressed by $\eta(x, y, t)$. For the free surface of water waves, the kinematic condition that particles cannot leave the water interface (assumption 5) is obtained by stating that the vertical speed of the free surface should be the same as that of the fluid particles

$$\frac{\partial\eta}{\partial t} + \frac{\partial\Phi}{\partial x}\frac{\partial\eta}{\partial x} + \frac{\partial\Phi}{\partial y}\frac{\partial\eta}{\partial y} = \frac{\partial\Phi}{\partial z} \qquad \text{at } z = \eta(x, y, t) \tag{B.6}$$

The second kinematic boundary condition follows from the impermeability of the sea bed (assumption 6). If the depth of the seabed is described by $h(x, y)$, the fluid flow normal to the bed must be zero by the following equation

$$\nabla\Phi \cdot \hat{\mathbf{n}} = \frac{\partial\Phi}{\partial n} = 0 \qquad \text{on } z = -h(x, y) \tag{B.7}$$

where where $\hat{\mathbf{n}}$ is the unit vector normal to the sea bed. Note that when the sea bed is assumed to be horizontal, this results in $\frac{\partial\Phi}{\partial z} = 0$.

The momentum balance equations, such as Equation (B.3) in x-direction, can be combined in all directions and expressed in terms of the velocity potential Φ. The only external forces were assumed to be the gravitation force (in z-direction). If furthermore the surface tension is neglected (which is valid for waves longer than a few centimetres), the pressure must be continuous across the water-air interface. At any point in the fluid, Bernoulli's equation must hold

$$\frac{\partial\Phi}{\partial t} + \frac{1}{2}|\nabla\Phi|^2 + \frac{p}{\rho} + gz = 0 \tag{B.8}$$

where ρ is the fluid density, g is the gravitational acceleration and p the pressure in the fluid (relative to atmospheric pressure). The air pressure along the interface is taken constant and equal to zero $p = 0$ on $z = \eta(x, y, z)$.

At the interface where $p = 0$, the following dynamic boundary condition follows

$$\frac{\partial \Phi}{\partial t} + \frac{1}{2}|\nabla \Phi|^2 + g\eta = 0 \qquad \text{on } z = \eta(x, y, t) \tag{B.9}$$

The complete description of the surface gravity waves is now given in Equations (B.5) - (B.9). These equations are non-linear however, and therefore difficult to work with. Therefore, linearisation is applied to simplify the non-linear equations and boundary conditions to first order.

For sufficiently small motions relative to the wavelength, the non-linear free surface conditions (B.6) and (B.9) may be linearised around the undisturbed state $\eta(x, y, t) = 0$. This linearisation is valid when the amplitude of the fluid motion is small compared to the wavelength throughout the fluid domain, including the amplitude of any structural motions. Note that the Laplace equation (B.5) and the dynamic seabed condition (B.7) are linear already. The other equations will be linearised, under the small angle approximation.

For the non-linear Bernoulli equation (B.8), linearisation around $\eta(x, y, t) = 0$ gives

$$\frac{\partial \Phi}{\partial t} + \frac{p}{\rho} + g\eta = 0 \tag{B.10}$$

because the second order term simply drops out. Also, because of this small amplitude in water surface, the terms with partial derivatives $\frac{\partial \eta}{\partial x}$ and $\frac{\partial \eta}{\partial y}$ drop out of the Kinematic boundary condition (B.6). This boundary condition then reduces to

$$\frac{\partial \eta}{\partial t} = \frac{\partial \Phi}{\partial z} \qquad \text{at } z = 0 \tag{B.11}$$

Dynamic boundary condition (B.9) becomes

$$\frac{\partial \Phi}{\partial t} + g\eta = 0 \qquad \text{at } z = 0 \tag{B.12}$$

These equations can be combined by differentiating the dynamic condition with respect to t and substitution of $\frac{\partial \eta}{\partial t}$ from the kinematic condition. This results in the linearised free-surface condition

$$\frac{\partial^2 \Phi}{\partial t^2} + g\frac{\partial \Phi}{\partial z} = 0 \qquad \text{at } z = 0 \tag{B.13}$$

The Laplace equation and the kinematic boundary conditions (B.7), which was linear already, and (B.11) are enough to solve for Φ. The Bernoulli equation and the dynamic boundary condition can be used, together with this solution Φ to obtain expressions for the dynamic aspect of the surface gravity waves.

C

Derivation body dynamics

To describe the dynamics of structures in water, a rigid body is the simplest structure to start with. A free rectangular floating rigid structure with appropriate dimensions can be seen as a simplified model of a floating solar structure. Therefore, it is relevant to start the study of rigid body dynamics in the first place.

C.1. Degrees of freedom

In order to describe the motion of a floating object, a combination of 6 degrees of freedom, or modes of motion, can describe every possible movement. The velocity of a point on the surface of the structure, measured normal to the surface, can be written in the following way

$$V_n = U \cdot n + \Omega \cdot (r \times n) \tag{C.1}$$

where r is the position vector of the point measured from the centre of rotation and n the normal vector to the structure's surface directed out of the fluid. The other vectors describe the translational $U = (U_1, U_2, U_3)$ and rotational $\Omega = (U_4, U_5, U_6)$ velocity of the body. In ascending order, these are called surge, sway, heave, roll, pitch and yaw as shown in Figure C.1.

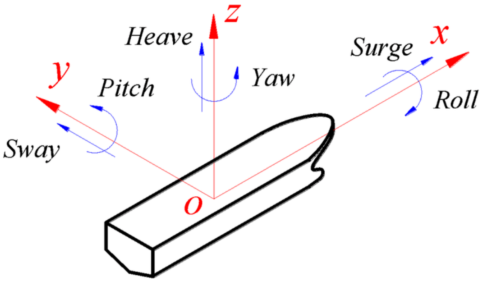

Figure C.1: The 6 degrees of freedom of the centre of gravity: roll, pitch, yaw, heave, sway and surge. [14]

Thus, all vectors are defined in a three dimensional Cartesian coordinate system. Note that V_n can be rewritten in terms of these modes of motion as

$$V_n = \sum_{j=1}^{6} U_j n_j \tag{C.2}$$

The factors $\{n_j, j = 1,2,3\}$ are the x, y, z components of the unit normal to the structure such that $n = (n_1, n_2, n_3)$. They are defined by

$$n_1 = \cos(n, x), \qquad n_2 = \cos(n, y), \qquad n_2 = \cos(n, z) \tag{C.3}$$

The resulting factors $\{n_j, j = 4, 5, 6\}$ are the components of $r \times n$. If (x, y, z) are the coordinates of a point on the structure's surface and (x', y', z') are the coordinates of the equilibrium position of the centre of rotation, this cross product results in

$$n_4 = (y - y')n_3 - (z - z')n_2 \tag{C.4}$$

$$n_5 = (z - z')n_1 - (x - x')n_3 \tag{C.5}$$

$$n_6 = (x - x')n_2 - (y - y')n_1 \tag{C.6}$$

If the oscillations are time-harmonic, each velocity component in equation (C.2) may be rewritten as

$$U_j = \mathrm{Re}\{u_j \mathrm{e}^{-i\omega t}\} \tag{C.7}$$

This way, u_j is the complex amplitude of the oscillations in mode j.

C.2. Equations of motion

The equation of motion in frequency domain is given by [30]

$$\{-\omega^2(M + A(\omega)) + i\omega B(\omega) + C\}U(\omega, \theta) = F(\omega, \theta) \tag{C.8}$$

where C is the structure stiffness matrix, $B(\omega)$ the hydrodynamic damping matrix, M the mass of the floating structure, $A(\omega)$ is the hydrodynamic added mass matrix and $F(\omega, \theta)$ is the hydrodynamic force vector. The force and the body motion matrix $U(\omega, \theta)$ are dependent on both wave frequency ω and wave direction θ.

In this frequency domain equation of motion, the mass matrix M and the stiffness matrix C are input parameters determined by the structure characteristics. The mass matrix is defined by the body mass and the radius of gyration of the structure. If all 6 degrees of freedom are considered, the mass matrix is given by

$$M = \begin{bmatrix} m & 0 & 0 & 0 & 0 & 0 \\ 0 & m & 0 & 0 & 0 & 0 \\ 0 & 0 & m & 0 & 0 & 0 \\ 0 & 0 & 0 & r_{xx}^2 m & 0 & 0 \\ 0 & 0 & 0 & 0 & r_{yy}^2 m & 0 \\ 0 & 0 & 0 & 0 & 0 & r_{zz}^2 m \end{bmatrix} \tag{C.9}$$

In this matrix definition, m is the mass of the floating body and r_{xx}, r_{yy} and r_{zz} are the radii of gyration with respect to the x, y and z axes respectively. The radius of gyration is determined by

$$r_{xx} = \sqrt{\frac{I_{xx}}{m}} \tag{C.10}$$

where I_{xx} is the moment of inertia regarding the x axis.[1] The definition is analogous in y and z direction. Note that the coupling terms between pitch and roll for example ($I_{xz} = I_{zx}$) are neglected because they are generally small. [30]

The hydrostatic stiffness matrix C contains the restoring terms which influence the heave, roll and pitch movements. With respect to the centre of floatation (at the waterline), the linearised hydrostatic

---

[1] The definition of the M matrix can thus also be

$$M = \begin{bmatrix} m & 0 & 0 & 0 & 0 & 0 \\ 0 & m & 0 & 0 & 0 & 0 \\ 0 & 0 & m & 0 & 0 & 0 \\ 0 & 0 & 0 & I_{xx} & 0 & 0 \\ 0 & 0 & 0 & 0 & I_{yy} & 0 \\ 0 & 0 & 0 & 0 & 0 & I_{zz} \end{bmatrix} \tag{C.11}$$

stiffness matrix $\tilde{C}$ can be defined as [31]

$$\tilde{C} = \begin{bmatrix} 0 & 0 & 0 & 0 & 0 & 0 \\ 0 & 0 & 0 & 0 & 0 & 0 \\ 0 & 0 & \rho g A & 0 & 0 & 0 \\ 0 & 0 & 0 & q_{xx}\rho g V & 0 & 0 \\ 0 & 0 & 0 & 0 & q_{yy}\rho g V & 0 \\ 0 & 0 & 0 & 0 & 0 & 0 \end{bmatrix} \tag{C.12}$$

where $q_{xx} = d_{kb} + \frac{I_{xx}}{V} - d_{kg}$ is the distance between the centre of gravity and the metacentre in x-direction and $q_{yy} = d_{kb} + \frac{I_{yy}}{V} - d_{kg}$ is the distance between the centre of gravity and the metacentre in y-direction. In the calculations for these distances, d_{kb} is the distance between the keel and the centre of buoyancy and d_{kg} is the distance between the keel and the body's centre of gravity. The other constants used are the density of the water ρ, the gravitational constant g, the horizontal surface area of the floating body A and the volume of the body V. The use of $\rho g A$ as first non-zero element is valid for small values of z, but when body is vertically walled it remains exact for larger values of z as well.

Note that this matrix is defined with respect to the centre of floatation, but all other motions are defined with respect to the centre of gravity. Therefore, a translation has to be performed using the following translation matrix

$$T = \begin{bmatrix} 1 & 0 & 0 & 0 & 0 & 0 \\ 0 & 1 & 0 & 0 & 0 & 0 \\ 0 & 0 & 1 & 0 & 0 & 0 \\ 0 & -\delta z & \delta y & 1 & 0 & 0 \\ \delta z & 0 & 0 & -\delta x & 1 & 0 \\ -\delta y & \delta x & 0 & 0 & 0 & 1 \end{bmatrix} \tag{C.13}$$

with the δx representing the difference between the location of the centre of floatation and the centre of gravity in x-direction and similarly in the other two directions. Then $T\tilde{C}T^*$ will represent the correct hydrostatic stiffness matrix with respect to the centre of gravity, thus with the same origin as the other motions in the equation.

$$C = T\tilde{C}T^* = \begin{bmatrix} 0 & 0 & 0 & 0 & 0 & 0 \\ 0 & 0 & 0 & 0 & 0 & 0 \\ 0 & 0 & \rho g A & \delta y \rho g A & -\delta x \rho g A & 0 \\ 0 & 0 & \delta y \rho g A & q_{xx}\rho g V + (\delta y)^2 \rho g A & -\delta x \delta y \rho g A & 0 \\ 0 & 0 & -\delta x \rho g A & 0 & q_{yy}\rho g V & 0 \\ 0 & 0 & 0 & 0 & 0 & 1 \end{bmatrix} \tag{C.14}$$

Notice that when the body is axially symmetric in the x- and y-axis, this results in $C = T\tilde{C}T^* = TCT^*$.

The hydrodynamic coefficients $A(\omega)$, $B(\omega)$ and $F(\omega, \theta)$ are parameters to be determined numerically by a boundary element solver in frequency domain. Their analytical definitions are given in section 2.4.3. The physical properties that these quantities stand for can be explained as follows.

The added mass $A(\omega)$ can be explained as the mass of the water that is forced to move along with the motion of the object considered. Thus, when an object oscillates in still water, the surrounding water volume that is caused to move due to acceleration of the body is considered to be the added mass. It is a virtual hydrodynamic force term included in the equation of motion (C.8). When the object considered is not symmetrical, the added mass will be different for movement in each degree of freedom. For example, if the object performs a heaving motion, the water around it will also move in heaving mode. However, the water might be forced to perform movement in other degrees of freedom as well. This depends on the object characteristics such as its dimensions and draft. The added mass matrix is therefore a kind of correlation matrix between degrees of freedom. The matrix element A_{ij} shows the effect of a unit amplitude motion of the object in degree of freedom i on the additional mass that has to be considered the equation of motion of mode j. Therefore, the total matrix has the size of $n_{dof} \times n_{dof}$

for a single frequency ω.

The hydrodynamic radiation damping $B(\omega)$ can be thought of as the damping due to the wave energy that radiates outward, away from a moving structure. Again, if the object is not symmetrical, this will be different for movement in the different modes. The matrix element B_{ij} shows the damping effect of a unit amplitude motion of the object in degree of freedom i on the movement of the object motion mode j. Again, the total matrix has the size of $n_{dof} \times n_{dof}$ for a single frequency ω.

Lastly, the hydrodynamic or exciting force $F(\omega, \theta)$ is the force due to wave loads of the incoming and reflected wave fields. It gives the force or moment generated by a unit amplitude wave with incoming angle θ. The vector element F_i gives this force (for $i \in \{1, 2, 3\}$) or moment (for $i \in \{4, 5, 6\}$) acting on the object in the direction of the degree of freedom i. Therefore, it is a vector with length n_{dof}.

D

Analytical solution diffraction problem

The diffraction problem can be solved analytically for a two-dimensional setup [24, 39, 59, 60]. The floating object is assumed to be infinitely wide, with no geometry variations in y-direction. Incident waves will be oblique waves propagating along the x-axis (in positive direction, thus $\beta = 0$). Figure D.1 shows part of the domain considered, with the appropriate definition of the Cartesian coordinates.

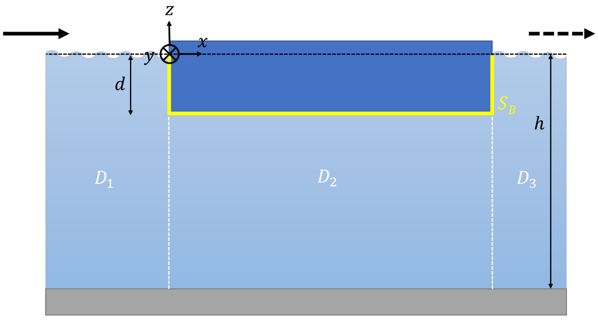

Figure D.1: Sketch of the domain for the rigid barge scattering problem. The origin of the coordinate system is located at equilibrium water level in the centre of the object. The domain will be split up in subdomains D_1, D_2 and D_3. The draft d, floater length L_f and water depth h are shown.

The linearised boundary conditions for this problem are the free surface boundary condition (2.13), the seabed condition (2.14), the body surface boundary condition (2.24) and the radiation condition (2.25). The domain will be split up into three subdomains D_1, D_2 and D_3, which will each have their own set of boundary conditions. The velocity potential solutions are matched across the boundaries of these domains, such that the fluid pressure and normal velocity across $x = 0$ and $x = L_f$, $z \in (-h, -d)$ are continuous. This implies continuity of ϕ and ϕ_x.

An overview of the locations for which the boundary conditions must hold is given in Table D.1.

Domain	Location	Boundary condition type	Linearised boundary condition equation
D_1	$x < 0, z = 0$	free surface	$\frac{\partial \phi_{D_1}}{\partial z} = K\phi_{D_1}$
	$x < 0, z = -h$	seabed	$\frac{\partial \phi_{D_1}}{\partial z} = 0$
	$x = 0, z \in [-d, 0]$	body surface	$\frac{\partial \phi_{D_1}}{\partial x} = -\frac{\partial \phi_I}{\partial x}$
	$x = 0, z \in [-h, -d]$	matching conditions	$\phi_{D_1} = \phi_{D_2}, \quad \frac{\partial \phi_{D_1}}{\partial x} = \frac{\partial \phi_{D_2}}{\partial x}$
	$x \to -\infty, z \in [-h, 0]$	radiation condition	ϕ_{D_1} outgoing, finite for $x \to -\infty$
D_2	$0 < x < L_f, z = -d$	body surface	$\frac{\partial \phi_{D_2}}{\partial z} = -\frac{\partial \phi_I}{\partial z}$
	$0 < x < L_f, z = 0$	seabed	$\frac{\partial \phi_{D_2}}{\partial z} = 0$
	$x = 0, z \in [-h, -d]$	matching conditions	$\phi_{D_1} = \phi_{D_2}, \quad \frac{\partial \phi_{D_1}}{\partial x} = \frac{\partial \phi_{D_2}}{\partial x}$
	$x = L_f, z \in [-h, -d]$	matching conditions	$\phi_{D_2} = \phi_{D_3}, \quad \frac{\partial \phi_{D_2}}{\partial x} = \frac{\partial \phi_{D_3}}{\partial x}$
D_3	$x > L_f, z = 0$	free surface	$\frac{\partial \phi_{D_3}}{\partial z} = K\phi_{D_3}$
	$x > L_f, z = -h$	seabed	$\frac{\partial \phi_{D_3}}{\partial z} = 0$
	$x = L_f, z \in [-d, 0]$	body surface	$\frac{\partial \phi_{D_3}}{\partial x} = -\frac{\partial \phi_I}{\partial x}$
	$x = L_f, z \in [-h, -d]$	matching conditions	$\phi_{D_2} = \phi_{D_3}, \quad \frac{\partial \phi_{D_2}}{\partial x} = \frac{\partial \phi_{D_3}}{\partial x}$
	$x \to \infty, z \in [-h, 0]$	radiation condition	ϕ_{D_3} outgoing, finite for $x \to \infty$

Table D.1: Boundary conditions for each subdomain D_1, D_2, D_3 to solve for $\nabla^2 \phi_D = 0$.

The velocity potential is solved in each domain with separation of variables and eigenfunction expansion. Separation of variables is used to split the velocity potential in a horizontal and a vertical expression, $\phi(x, z) = X(x)Z(z)$, such that substitution in the Laplace equation results in

$$\frac{1}{X}\frac{d^2X}{dx^2} = -\frac{1}{Z}\frac{d^2Z}{dz^2} = \lambda \tag{D.1}$$

where the separation constant, or eigenvalue, λ is to be determined by the boundary conditions. Both $X(x)$ and $Z(z)$ have their own general solutions which satisfy these boundary conditions. With $\lambda = k^2 > 0$, the general expressions are

$$X(x) = Ae^{kx} + Be^{-kx} \tag{D.2}$$

$$Z(z) = C\cos k(z + h) + D\sin k(z + h) \tag{D.3}$$

from which the eigenfunctions will follow. $\lambda = 0$ gives only the trivial solution and is therefore not an eigenvalue, $\lambda < 0$ does not fit the boundary conditions. The velocity potential solution for domain D_1 is a superposition of these possible eigenfunction modes:

$$\phi_{D_1}(x, z) = \sum_{n=0}^{\infty} A_n \mathrm{e}^{k_n x} \psi_n(z) \qquad \text{for } x < 0, z \in [-h, 0] \tag{D.4}$$

In this equation, $\psi_n(z)$ are the vertical eigenfunctions which fit the free surface and seabed condition, given by

$$\psi_n(z) = N_n^{-1} \cos k_n(z + h) \qquad \text{for } n = 0, 1, 2, ... \tag{D.5}$$

Here, h is the constant water depth, k_n are the eigenvalues of the problem and N_n ensures a normalised amplitude

$$N_n^2 = \frac{1}{2}\left(1 + \frac{\sin 2k_n h}{2k_n h}\right) \tag{D.6}$$

For the other subdomains D_2 and D_3, an eigenfunction expansion can be obtained in a similar manner using the other sets of boundary conditions. Notice that the separated Laplace equation gives to differential equations of standard Sturm Liouville type, thus has an infinite number of real eigenvalues $\lambda_n, n \in \{1, 2, ...\}$ which can be ordered in size. Each eigenvalue corresponds to a unique eigenfunction

ψ_n, which form a complete orthonormal set. The eigenvalues follow from the dispersion relation: the free surface condition is satisfied if k_n is a root of

$$K + k \tan kh = 0 \tag{D.7}$$

In this equation, $K = \omega^2/g$ and k the separation constant. The roots of this equation are either purely real or purely imaginary: $k_0 = -\mathrm{i}k$ is the imaginary root and k_n for $n = 1, 2, ...$ are infinitely many real roots for this equation. The negative values $-k_n, n \in \{0, 1, 2, ...\}$ would also satisfy the dispersion relation, but these give the same set of eigenfunctions. Notice that the imaginary eigenvalue corresponds to a propagating mode, whereas the real roots correspond to evanescent modes which decay to zero as $x \to \infty$ or $x \to -\infty$.

The analytical expression for $\phi_{D_1}(x, z)$ still includes the unknown complex coefficients A_n for $n = 0, 1, 2, ...$, which originate from the horizontal eigenfunction expansion. These can be solved by substituting the eigenfunction expansion, given in (D.4), and the similar expressions for ϕ_{D_2} and ϕ_{D_3} into the continuity conditions

$$\phi_{D_1} = \phi_{D_2} \qquad \text{for } x = 0, z \in [-h, -d] \tag{D.8}$$

$$\frac{\partial \phi_{D_1}}{\partial x} = \begin{cases} -\frac{\partial \phi_I}{\partial x} & \text{for } x = 0, z \in [-d, 0] \\ \frac{\partial \phi_{D_2}}{\partial x} & \text{for } x = 0, z \in [-h, -d] \end{cases} \tag{D.9}$$

These equations are a combination of the matching conditions for $z \in [-h, -d]$ and the body boundary equation for $z \in [-d, 0]$. A similar set of equation holds at the boundary $x = L_f$, with ϕ_{D_2} and ϕ_{D_3}.

These continuity conditions can be converted in a system of equations that can be solved numerically in various ways, as presented in for example [6, 24, 39, 60]. Zheng et al. (2004) [**?**]showed the continuity conditions are satisfied in a least-square sense over the z-interval by multiplication with the set of vertical eigenfunctions ψ_m, $m \in \{0, 1, 2, ...\}$ and integrating them over the appropriate range in z at the boundaries $x = 0$ and $x = L_f$. This leads to an infinite set of integral equations for A_n and the unknown complex coefficients for the eigenfunction expansions of ϕ_{D_2} and ϕ_{D_3}. The analytical solutions can be approximated by truncation of the infinite sum: the first N terms are taken into account, which results in a $4N \times 4N$ linear system of complex equations and an equal number of unknown coefficients. The exact expressions for this linear system are given in [60]. Alternatively, a Galerkin approach is suggested in [39], which expands the horizontal fluid velocity on $x = 0$ in terms of the orthogonal eigenfunctions ϕ_m, $m \in \{0, 1, 2, ...\}$. This might have better convergence characteristics in N and thus requires a smaller system of equations.

When multiple floating barges are included behind each other, the same method can be used [59]. In total, $2n_{FL} + 1$ subdomains will have to be defined, where n_{FL} is the number of floating objects included. With the appropriate matching conditions in between these domains, the diffraction problem can be defined as a linear system of $4N \times n_{FL}$ complex equations to obtain the same number of unknown coefficients.

E

Surface elevation results - 2D diffraction problem

The results for the two dimensional numerical diffraction problem, described in section 5.2, have been included in this appendix. The resulting surface elevation at $y = 0$ is given over the domain $x \in [-400, 400]$. This is shown for five wave frequencies tested, which were distributed in the range $f \in [0.1, 0.3]$ Hz.

The configuration of the (restrained) object is explained in section 5.2.1. The dimensions below the still water surface are $12 \times 200 \times 0.333$ m in x, y, z direction respectively. The object surface is meshed into 0.5×0.5 rectangular panels in the x, y plane and 0.5×0.167 m rectangular grid cells in x, z and y, z planes. This mesh is described more elaborately in section 5.2.2.

The visualisation mesh used to compute the surface elevation results has grid cells of 0.5×0.5 m as well, centered at $y = 0$. In x-direction, there are thus 1600 grid cells next to each other where the velocity potential and then surface elevation is computed. The surface elevation is plotted against x in Figure E.1.

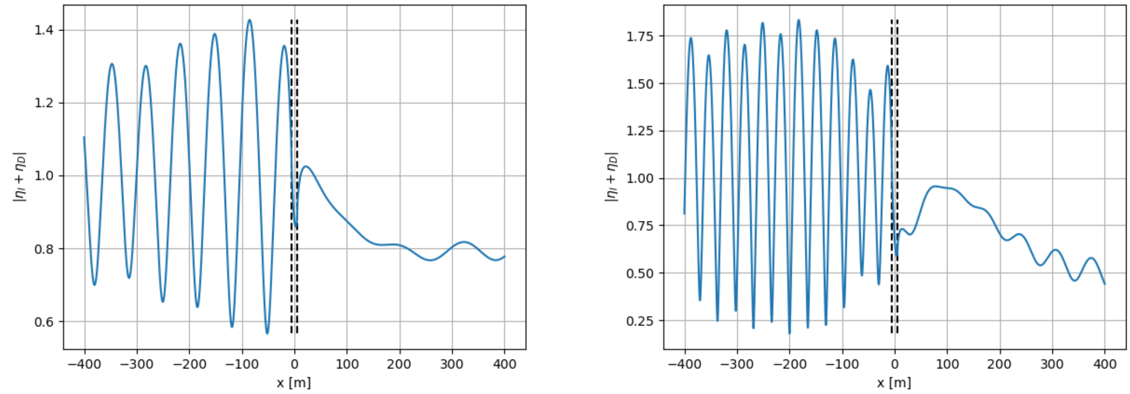

(a) $f = 0.1$ Hz, $\lambda = 129$ m

(b) $f = 0.15$ Hz, $\lambda = 68$ m

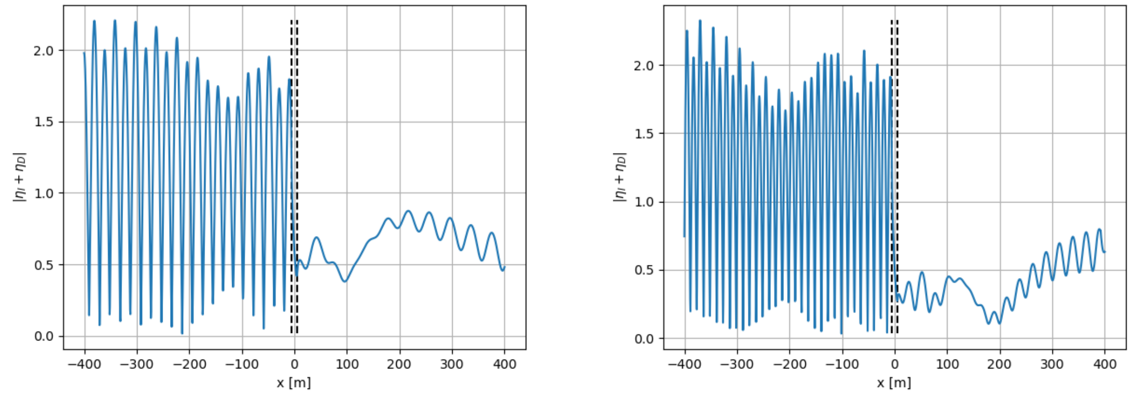

(c) $f = 0.2$ Hz, $\lambda = 39$ m

(d) $f = 0.25$ Hz, $\lambda = 25$ m

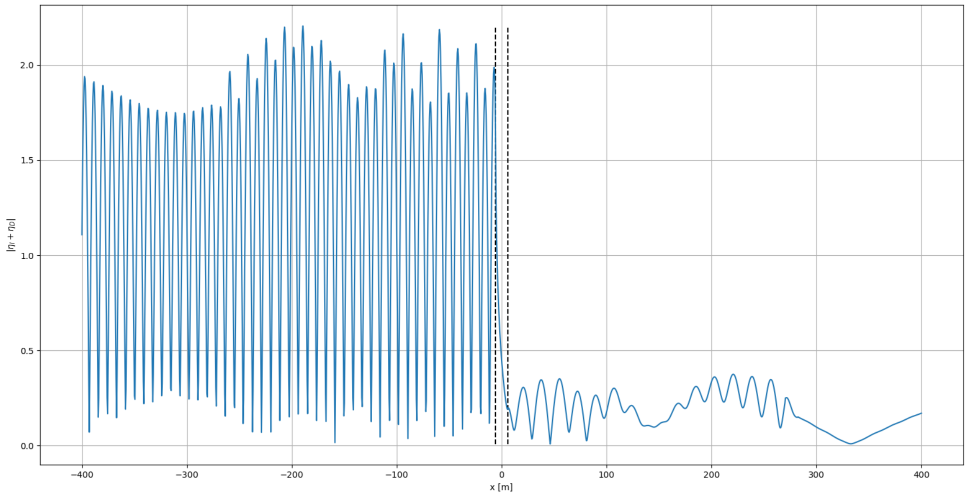

(e) $f = 0.3$ Hz, $\lambda = 17$ m

Figure E.1: Amplitude of surface elevation $|\eta_I + \eta_D|$ for the 2D diffraction model as a function of x at $y = 0$ for various incoming wave frequencies and thus wavelengths. The dotted lines show the edges of the submerged body.

F

Surface elevation results - 3D effects diffraction problem

The results for the diffraction problem, described in section 5.2, are not entirely two dimensional. The floating structure is 200 m wide to approximate an infinitely long object in y-direction, but this approximation does not entirely hold. The three dimensional effects in the resulting surface elevation are shown for the domain $(x, y) \in [-50, 200] \times [-125, 125]$. This is shown for five wave frequencies tested, which were distributed in the range $f \in [0.1, 0.3]$ Hz.

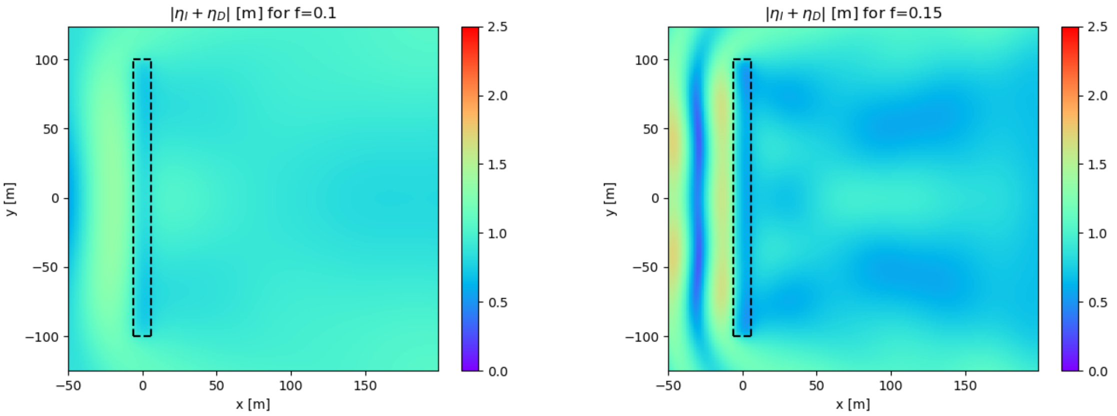

(a) $f = 0.1$ Hz, $\lambda = 129$ m

(b) $f = 0.15$ Hz, $\lambda = 68$ m

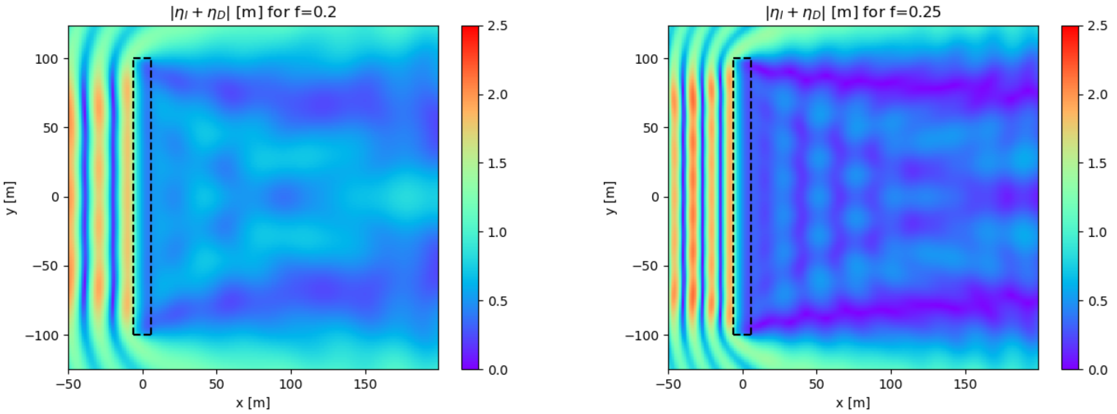

(c) $f = 0.2$ Hz, $\lambda = 39$ m

(d) $f = 0.25$ Hz, $\lambda = 25$ m

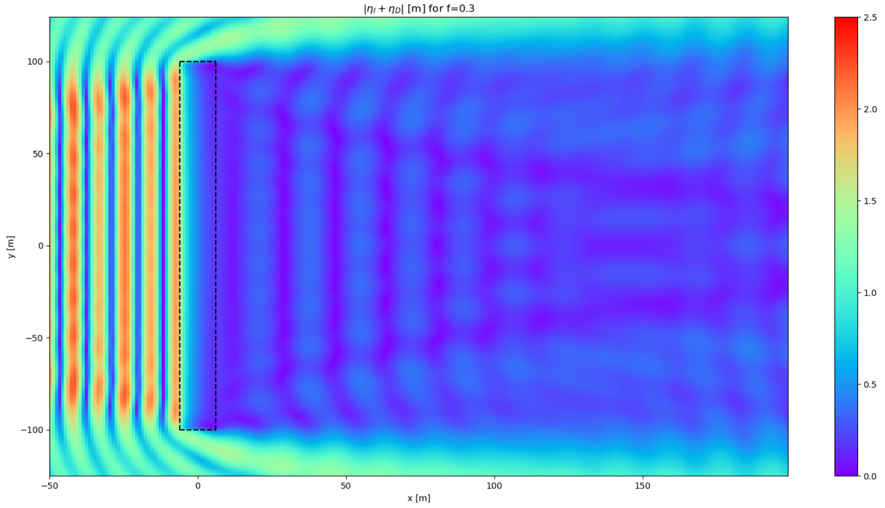

(e) $f = 0.3$ Hz, $\lambda = 17$ m

Figure F.1: Amplitude of complex surface elevation $|\eta_I + \eta_D|$ for the diffraction model over the domain $(x, y) \in [-50, 200] \times [-125, 125]$ for various incoming wave frequencies and thus wavelengths. The dotted lines show the edges of the submerged body; $L_f = 12$ m, $W_f = 200$ m.

The three dimensional surface elevation amplitude for a twice as long floater, $L_f = 24$ m, are given for the domain $(x, y) \in [-50, 200] \times [-125, 125]$ in Figure F.2. This is shown for $f = 0.1$ Hz and $f = 0.25$ Hz. The computed transmission coefficients for these results were $K_t = 0.84$ and $K_t = 0.25$ respectively.

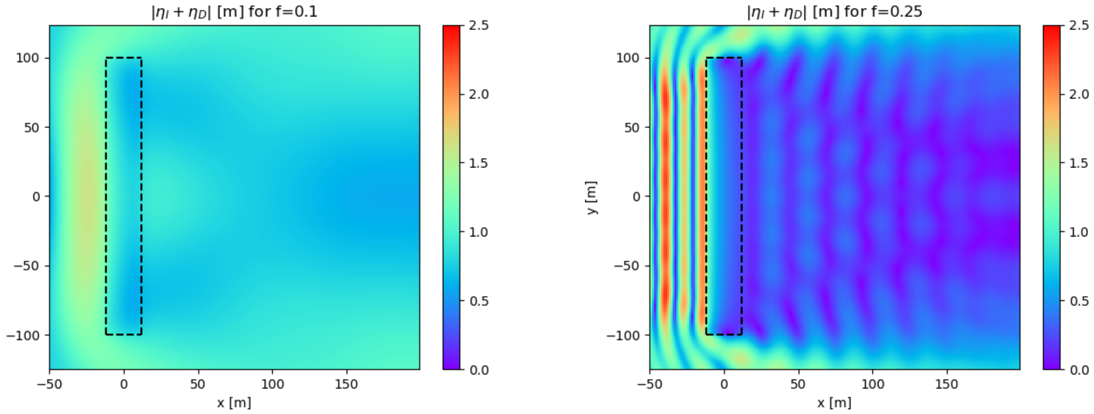

(a) $f = 0.1$ Hz, $\lambda = 129$ m, $L_f/\lambda = 0.19$

(b) $f = 0.25$ Hz, $\lambda = 25$ m, $L_f/\lambda = 1.04$

Figure F.2: Amplitude of complex surface elevation $|\eta_I + \eta_D|$ for the diffraction model over the domain $(x, y) \in [-50, 200] \times [-125, 125]$ for various incoming wave frequencies and thus wavelengths. The dotted lines show the edges of the submerged body; $L_f = 24$ m, $W_f = 200$ m.

G

Basin test scaling

When scaling between full scale (offshore) and model scale (basin) parameters, either the Froude number (G.1) or the Reynolds number (G.2) can be kept constant depending on the test setting.

$$Fr = \frac{u}{\sqrt{gl}} \propto \frac{F_i}{F_g} \tag{G.1}$$

$$Re = \frac{ul}{\nu} \propto \frac{F_i}{F_\nu} \tag{G.2}$$

Here u is the fluid velocity, g the gravitational accelleration constant, l the length concerned in fluid-solid interaction and ν the fluid viscosity. The Froude and Reynolds number are non-dimensional quantities which show the relative magnitude of the inertial, gravitational and viscous forces (F_i, F_g and F_ν respectively). In the ideal situation, the model test would be scaled in such a way that the balance between these forces is the same as in the full scale situation such that the same dynamic behaviour is ensured, which would imply the Froude and Reynolds number to have the same values in the basin test and offshore. However, this is an unattainable requirement on small scale due to the constant gravitational acceleration constant g and kinematic viscosity ν (when the same fluid is used). Therefore only one scaling number can be kept constant.

In the basin test, a geometric scaling parameter $s = 25$ was chosen. Froude scaling was applied to scale the physical quantities, because the inertial effects were assumed to be more important in the floater dynamics than the viscous effects.

This assumption can be questioned, because the floating object had a relatively small mass to volume ratio due to its low density. As a consequence, the ratio of wetted surface area to volume was quite large, which indicates that viscous forces are not negligible.

Froude scaling with a geometric scale factor s results in the scaling of physical parameters as shown in Figure G.1.

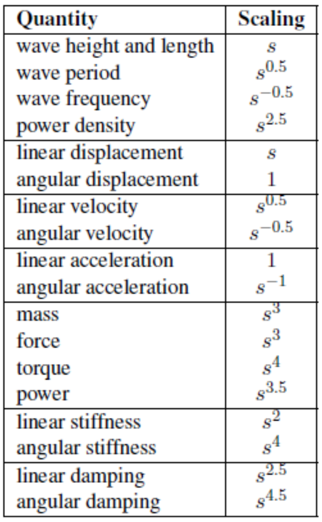

Quantity	Scaling
wave height and length	s
wave period	$s^{0.5}$
wave frequency	$s^{-0.5}$
power density	$s^{2.5}$
linear displacement	s
angular displacement	1
linear velocity	$s^{0.5}$
angular velocity	$s^{-0.5}$
linear acceleration	1
angular acceleration	s^{-1}
mass	s^{3}
force	s^{3}
torque	s^{4}
power	$s^{3.5}$
linear stiffness	s^{2}
angular stiffness	s^{4}
linear damping	$s^{2.5}$
angular damping	$s^{4.5}$

Figure G.1: Scaling of physical quantities when using Froude scaling with geometric scale s. [53]

The choice for a geometric scaling parameter $s = 25$ ensured the water depth and (significant) wave height to be equivalent to the offshore conditions while keeping s as low as possible, such that errors due to accuracy limits do not grow larger at full scale size. In the Scheldt flume, this results in a (maximum) water depth of $h = 21.25$ m and North sea wave conditions up to a significant wave height of $H_s = 5$ m.

H

Details flume setup

In this appendix, the elements within the flume setup will be discussed in more detail. These are the measurement devices, the floating model and the mooring connection.

Measurement devices
In terms of monitoring, the devices that were used are:

- 8 wave gauges or wave height meters
- cameras
- inertial measurement unit with gyroscope and accelerometer

The camera footage and accelerometer results will not be used to analyse the wave effects of the system, and are therefore left outside the scope of this thesis. The wave height meters were positioned at a distance of at least 2 m from the floating system, and were all centred in the middle of the flume (in direction orthogonal to the waves). These measured the wave height at a sampling rate of 400 Hz, and were calibrated at the equilibrium water level. The distances in between the wave gauges were determined by Deltares in such a way that the results would be well processable into two spectra of wave characteristics (one in front of the system and one behind the system) with the ELA method [19]. This will be explained further in the result analysis section 4.1.2.

Floating model
The floater design has been discussed in section 4.1.1. The system consists of connected floater blocks of 3 by 8 floaters, which were combined together and installed in the flume. As can be seen in Figure 4.1, the system was expanded with new floater blocks in direction of the wave paddle. In other words, the tests started with the smallest floating system and new rows of floaters were added at the fore side of the system. The system sizes that were tested are shown in Table H.1.

test file label	number of floater arrays	total number of floaters
A	0	0
B	6	48
C	12	96
D	18	144
E	24	192
F	33	256

Table H.1: System size configurations used during the basin tests. The first column shows the name of the test series, denoted by a letter. The second column shows the number of floater rows present in these tests. The third column shows the total number of floaters which are then present, which is equal to 8 times the number of floater arrays.

The total setup was placed as much to the front of the basin (as near to the wave paddle) as possible, such that the measurement time without a reflected wave present in the signal was maximised. However, the minimal distance between the wave paddle and the first WHM was preserved. This distance, needed for the wave to settle to an appropriate shape, is approximately 8 m.

Mooring

The structure was being held in place during the tests by 4 horizontal mooring lines, which were connected to mooring points at the edge of the basin. A Dyneema line was attached to each floater at the corner points of the system. On the other side, this rope was connected to two dynamometers, which were used as mooring line springs to resemble the actual mooring dynamics and measure the mooring forces at the same time. For each mooring line, a dynamometer spring of $k = 200$ N/m and a dynamometer spring of $k = 500$ N/m were put in series, such that their equivalent spring constant resulted in $k_{eq} = 142.8$ N/m. The dynamometers were then attached to the mooring points, located at the side of the basin at still water level. The angle that the mooring lines made with respect to the basin sides were small; the lines were almost in line with the floating system.

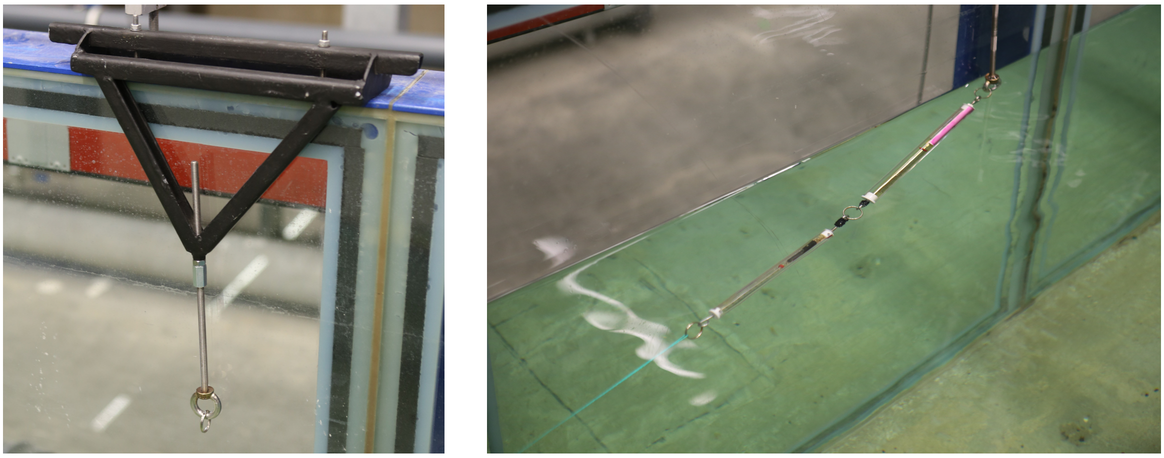

(a) Mooring point attached to basin side.

(b) Mooring line combination.

Figure H.1: Details of the mooring connection used to keep the model in place.

The fore side mooring points were moved for each new configuration, which was easily done because they were attached to the basin with magnets.

I

Wave conditions basin test

The wave conditions that were used for the Scheldt flume basin tests are given in Tables I.1 and I.2 for the regular and irregular wave tests respectively.

These wave conditions were chosen within restrictions of the flume possibilities. The work area of the Scheldt flume is shown in Figure I.1. This area shows combinations of (significant) wave height and (peak) wave period that can be tested, at basin test scale. It is restricted by three curves, which will be explained below.

1. Depth curve (green)
   The sides of the basin are 1.20 m high, measured from the bottom of the water column. Therefore, a water level of 0.85 m leaves a maximum (regular) wave height of 0.35 m. In case of an irregular JONSWAP wave spectrum, the maximum significant wave height due to limited water depth is 0.27 m.
2. Stroke curve (red)
   The wave paddle is restricted in its (horizontal) motion amplitude. Therefore, the amount of water that can be pushed forward to generate a wave is limited. which results in the red stroke curve as shown in Figure I.1.
3. Steepness curve (blue)
   The steepness curve of the waves shows the point where waves start to break. Since breaking waves are not constant over their distance travelled and cannot be measured as accurately, this is a condition to avoid for the wave gauge measurements.

Together, these restrictions form the envelope within which test conditions can be chosen.

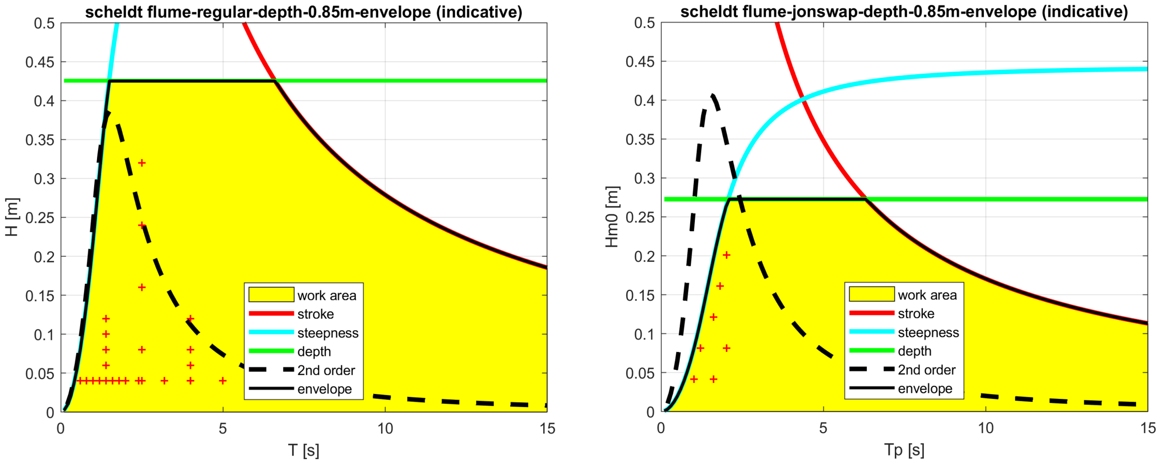

(a) regular waves

(b) irregular waves, JONSWAP spectrum

Figure I.1: Plots of possible work area Scheldt flume wave conditions for a water depth of 0.85 m. The envelope of the work area is defined by the restrictions of the stroke, steepness of the waves and depth of the basin. The red '+' marks inside this area show the wave conditions that were used during testing.

The regular wave conditions are shown in Table I.1, and have been plotted in Figure I.1a as the red '+' marks. Not all of these tests were performed for every system size. For the configurations with $n_{FL} = 12$ floater arrays and $n_{FL} = 24$ floater arrays, some of the regular wave tests were skipped because of time limitations.

The irregular wave conditions are shown in Table I.2 and have been plotted in Figure I.1b as the red '+' marks.

Steering file code	REG/ IRREG	H basin scale [m]	T basin scale [s]	k basin [1/m]	λ basin [m]	H full scale [m]	T full scale [s]	λ full scale [m]
T01REGH100T070	REG	0.04	1.4	2.16	2.91	1.0	7.0	72.7
T02REGH150T070	REG	0.06	1.4	2.16	2.91	1.5	7.0	72.7
T03REGH200T070	REG	0.08	1.4	2.16	2.91	2.0	7.0	72.7
T04REGH250T070	REG	0.10	1.4	2.16	2.91	2.5	7.0	72.7
T05REGH300T070	REG	0.12	1.4	2.16	2.91	3.0	7.0	72.7
T06REGH100T125	REG	0.04	2.5	0.96	6.56	1.0	12.5	163.9
T07REGH200T125	REG	0.08	2.5	0.96	6.56	2.0	12.5	163.9
T08REGH400T125	REG	0.16	2.5	0.96	6.56	4.0	12.5	163.9
T09REGH600T125	REG	0.24	2.5	0.96	6.56	6.0	12.5	163.9
T10REGH800T125	REG	0.32	2.5	0.96	6.56	8.0	12.5	163.9
T11REGH100T200	REG	0.04	4.0	0.56	11.14	1.0	20.0	278.4
T12REGH150T200	REG	0.06	4.0	0.56	11.14	1.5	20.0	278.4
T13REGH200T200	REG	0.08	4.0	0.56	11.14	2.0	20.0	278.4
T14REGH300T200	REG	0.12	4.0	0.56	11.14	3.0	20.0	278.4
T32REGH100T030	REG	0.04	0.6	11.18	0.56	1.0	3.0	14.1
T15REGH100T040	REG	0.04	0.8	6.29	1.00	1.0	4.0	25.0
T16REGH100T050	REG	0.04	1.0	4.03	1.56	1.0	5.0	39.0
T17REGH100T060	REG	0.04	1.2	2.84	2.21	1.0	6.0	55.3
T18REGH100T080	REG	0.04	1.6	1.74	3.60	1.0	8.0	90.1
T19REGH100T090	REG	0.04	1.8	1.47	4.29	1.0	9.0	107.1
T20REGH100T100	REG	0.04	2.0	1.27	4.95	1.0	10.0	123.8
T21REGH100T120	REG	0.04	2.4	1.01	6.24	1.0	12.0	156.0
T22REGH100T160	REG	0.04	3.2	0.72	8.72	1.0	16.0	218.1
T23REGH100T200	REG	0.04	4.0	0.56	11.14	1.0	20.0	278.4
T24REGH100T250	REG	0.04	5.0	0.45	14.11	1.0	25.0	352.7

Table I.1: Regular wave test conditions for Scheldt flume tests.

Steering file code	REG/ IRREG	Hs basin scale [m]	Tp basin scale [s]	kp basin [1/m]	λp basin [m]	Hs full scale [m]	Tp full scale [s]	λp full scale [m]
T25IRRH100T050	IRR	0.04	1.0	4.03	1.56	1.0	5.0	39.0
T26IRRH200T060	IRR	0.08	1.2	2.84	2.21	2.0	6.0	55.3
T27IRRH300T080	IRR	0.12	1.6	1.74	3.60	3.0	8.0	90.1
T28IRRH400T090	IRR	0.16	1.8	1.47	4.29	4.0	9.0	107.1
T29IRRH500T100	IRR	0.20	2.0	1.27	4.95	5.0	10.0	123.8
T30IRRH100T080	IRR	0.04	1.6	1.74	3.60	1.0	8.0	90.1
T31IRRH200T100	IRR	0.08	2.0	1.27	4.95	2.0	10.0	123.8

Table I.2: Irregular wave test conditions for Scheldt flume tests (JONSWAP spectrum).

J

Time series analysis

In every wave test, the surface elevation was measured by 8 wave gauges. These wave height meters were calibrated at the still water level $z = 0$ and measured at a frequency of 400 Hz. This results in 8 time series per test; 4 of them on each end of the flume. The time series data is combined and processed to filter out forward and backward propagating waves. This is done for the two locations; both the first set of wave gauges, wave height meters 1-4, and the second set of wave gauges, wave height meters 5-8, will give a forward and backward propagating wave signal each. How these wave signals are obtained from the dataset of time series will be explained in this section. After showing examples of the time series obtained, the regular wave approach will be explained in section J.1. It shows the least-squares fit to find leading order harmonic coefficients for regular wave tests. Lastly, the ELA method for filtering the irregular waves is introduced in section J.2.

The basin tests were performed for each system size (and the calibration test), for all wave conditions as given in Appendix I. Examples of the surface elevation output of a single wave gauge are shown below for a regular wave test and an irregular wave test.

The regular wave test ran for 4 minutes in total. The wave generator and sensors are started at the same time, such that the surface elevation before the first waves arrive is included in the measurement. An example of the full time series data of aregular wave test from a single wave gauge is shown in Figure J.1.

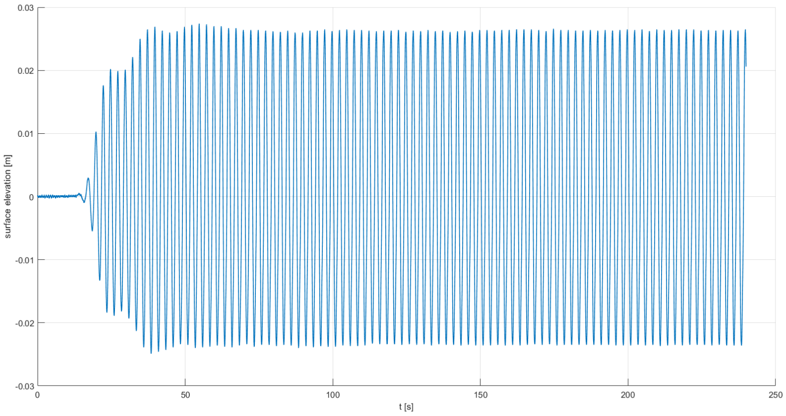

Figure J.1: Example of regular time series data. This plot shows the (basin test scale) surface elevation measured by WHM 2 for regular wave test 6 with a system size of 6 by 8 floaters. Test conditions were $H = 0.04$ m on basin scale, $H = 1.0$ m full scale, $T = 2.5$ s on basin scale, $T = 12.5$ s full scale.

This example shows that some time is needed to start up the wave, before it reaches the intended wave height of $H = 0.04$ m. The surface elevation started at $t = 7$ s, and settled to the correct wave height after about 3 wave periods around $t = 15$ s. After some more time, the reflections from the back of the flume start to arrive at this wave height meter, leading to the change in surface elevation after time reflection is added to the signal. This happened around the time $t = 40$ s. Therefore, the time in between the first surface elevation and the presence of the first reflections in the time series measurements at WHM 2 is $\Delta t = 33$ s. This is in accordance with the expectations. Namely, this wave gauge was located at $x_{WHM2} = 8.6$ m, thus the distance travelled before the wave returns to this wave gauge is around 82.8 m. The position at the end of the flume where the waves are reflected was around $x = 50$ m, but it consisted of an artificial beach before a wall, so this position might not be exact. With a phase velocity $v_p = \lambda/T \approx 2.6$ m/s, the travel time for a reflection for WHM 2 is 31.85 s, which is in the range of the Δt observed.

The irregular wave tests ran for in between 20 and 40 minutes. Namely, a minimum of 1100 waves was needed to have enough time series data to perform spectral analysis. The tests with longer wave periods thus took longer to run. In Figure J.2, an example of the first part of an irregular time series from a single wave gauge is shown.

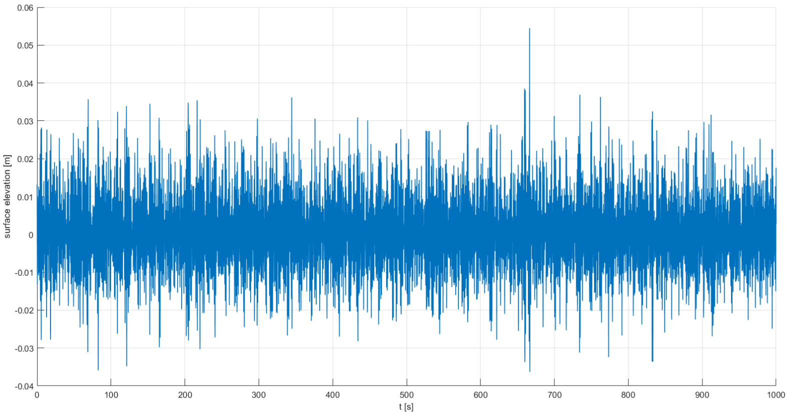

Figure J.2: Example of irregular time series data. This plot shows the (basin test scale) surface elevation measured by WHM 2 for irregular wave test 25 with a system size of 6 by 8 floaters. Test conditions were $H_s = 0.04$ m on basin scale, $H_s = 1.0$ m full scale, $T_p = 2.5$ s on basin scale, $T_p = 12.5$ s full scale. The first 1000 s of the time series are shown.

Figure J.2 shows the irregular character of the waves; wave heights fluctuate over time. The measurement for irregular tests shows no start up time in the signal because the data acquisition from the sensors was started after the first wave had passed through the whole basin. Namely, for spectral analysis it is convenient to leave the start up time of the signal out.

J.1. Least-squares fit regular waves

For the regular wave analysis, the leading order harmonic coefficients are determined by least squares fit of the amplitudes for the forward and backward propagating modes, as described in the appendix of Jacobsen et al. (2011) [29]. In short, the optimal solution to an over-determined set of equations is found by performing a least-squares fit for the coefficients A, B, C and D in the equations below. Equation (J.1) shows the forward propagating modes within the wave signal and equation (J.2) describes the backward propagating modes. This analysis is done for the two sets of wave height meters separately. The surface elevation $\eta(x)$ is used to fit the harmonic modes

$$A\cos(i_f(\omega t - kx)) + B\sin(i_f(\omega t - kx)) \tag{J.1}$$

$$C\cos(i_f(\omega t + kx)) + D\sin(i_f(\omega t + kx)) \tag{J.2}$$

at the positions x of the wave gauges and for the times t in a specified time interval $[t_1, t_2]$ within the time series measurements. In these equations, ω is the radial frequency and k the linear wave number. The index $i_f \in \{1, 2..., n_{freq}\}$ gives the order of the harmonic. Thus $i_f = 1$ gives the first harmonic, which corresponds to waves with frequency ω, $i_f = 2$ and higher give the higher harmonic components for the frequency 2ω and onwards, which might be present if the wave is not a perfect sinusoidal airy wave.

In the final analysis, the number of harmonics included in the calculations was $n_{freq} = 5$. The eight locations x of the wave height meters were given as input, and are shown in Table 4.1. The time interval for which the analysis is performed was chosen $[150, 200]$ s for each regular wave test. In this range, all regular wave tests were in the 'constant equilibrium state'; the setup time had passed and the reflections were part of the wave signal. The surface elevation showed (approximately) constant in amplitude for these times, see for example the data in Figure J.1. The time interval $[100, 150]$ s gave almost exactly the same results. The cyclic frequency ω and linear wave number k were determined from the wave period T that was specified in the steering file as the intended wave period. The dispersion relationship was solved numerically to find k.

A few assumptions are made when using this least-squares approach for the evaluation of harmonic amplitudes. Firstly, the distance between the wave height meters within a set is small enough such that the amplitudes are not altered by energy exchange nor by numerical diffusion. Secondly, the specified wave period T is considered constant along the flume. This period is used to determine the frequency and the wave number of the modes which the waves are fit to.

Regarding the first assumption, the distance between the wave gauges was maximally 2 m. The transmission coefficient in the calibration tests was found to have a minimum $K_t = 0.85$ (see Figure 4.5) over the distance in between the WHM sets, which is approximately 30 m. If we assume the dissipation by friction from the flume was constant over this distance, the transmission percentage per meter is $\sqrt[30]{0.85} = 0.994$. Therefore, the 2 m wave height difference between WHM 1 and 4 or WHM 5 and 8 due to the friction of the flume is estimated at maximally 1.1%.

J.2. ELA method irregular waves

The wave height measurements initially only include the desired incident wave spectrum. However, the waves are not dampened out completely at the end of the basin. Therefore, after the first waves have had enough time to travel to the end of the basin and back to the wave gauges, the measured signal will consist of both an incident wave and a reflected wave. The non-linear separation method which was used to separate these waves is the Eldrup Lykke Andersen (ELA) method [19]. It works for two-dimensional (long crested) regular and irregular waves.

The wave gauges time series were used as an input for the ELA method. The analysis was done separately for the first 4 wave height meters in front of the system and the last 4 wave height meters behind the system. Their data was combined into two sets of wave parameters; one in front of the system and one behind the system. The resulting parameters that were used are the significant wave height, H_{m0}, for irregular waves, and the peak period T_p. Furthermore, the variance density spectra of the irregular wave tests were analysed as well.

K

Variance density spectra for all irregular wave tests

The variance density spectra for the irregular JONSWAP wave tests, with test-IDs 25 - 31 and wave conditions as specified in Appendix I Table I.2. Each subfigure shows the spectrum for one of the system configurations, the amount of floater arrays n_{FL} included shows below. For each test, the incident and transmitted spectra are plotted. The incident spectrum is the forward propagating spectrum in front of the system, from wave gauges 1-4 (previously denoted as $p1$). The transmitted spectrum is the forward propagating spectrum behind the system, from wave gauges 5-8 (previously denoted as $p2$)The JONSWAP curve at which the test was initialised shows in the plots as well. All variance densities were scaled back to offshore scale values using the Froude scaling with $s = 25$ (Figure G.1). The spectral plots have been cut off at $f = 0.5$ Hz, in order to show the part of the figure where energy was present.

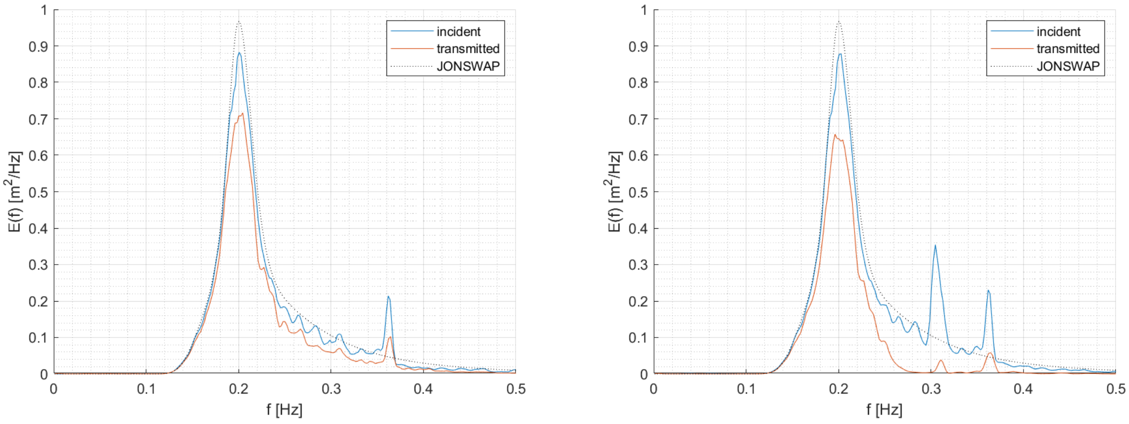

(a) Calibration test $n_{FL} = 0$

(b) System size $n_{FL} = 6$

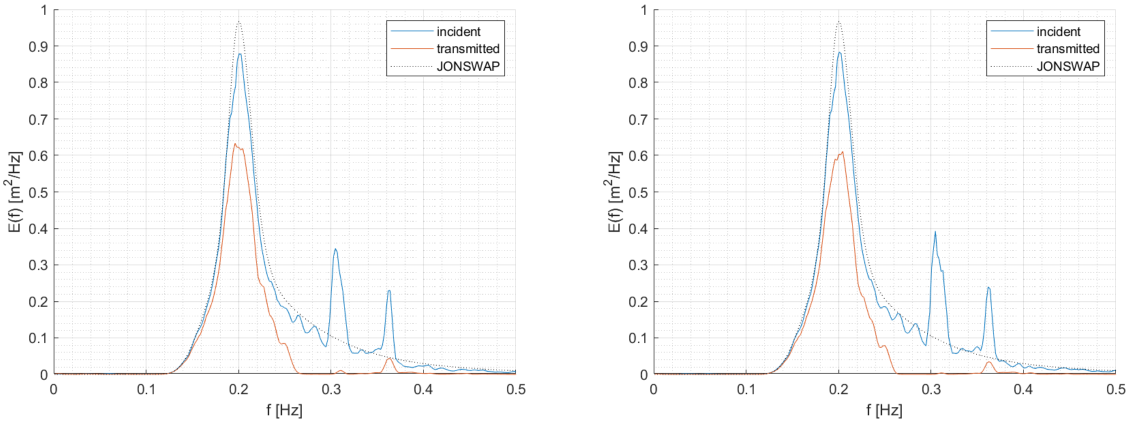

(c) System size $n_{FL} = 12$

(d) System size $n_{FL} = 18$

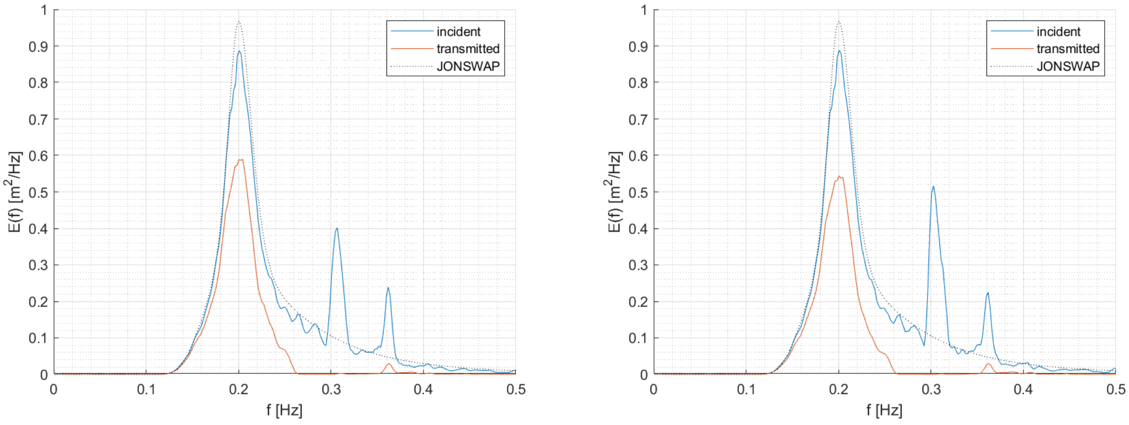

(e) System size $n_{FL} = 24$

(f) Maximum system size $n_{FL} = 33$

Figure K.1: Smoothed variance density spectra E as a function of the wave frequency f for irregular wave test 25 ($H_s = 1$ m, $T_p = 5$ s at offshore scale). Variance density is plotted for the incident wave spectrum (first 4 wave gauges) and transmitted wave spectrum (last 4 wave gauges), as well as the theoretical JONSWAP spectrum that the test was initialized at.

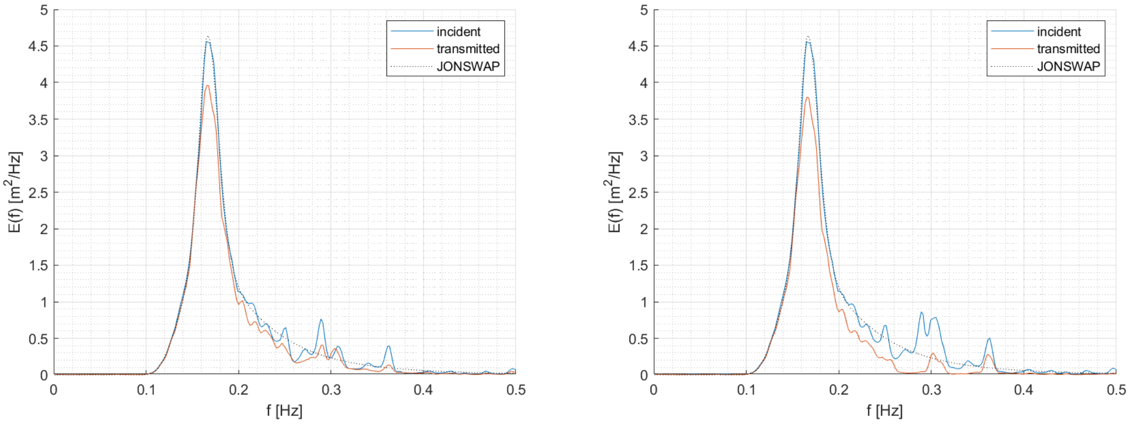

(a) Calibration test $n_{FL} = 0$

(b) System size $n_{FL} = 6$

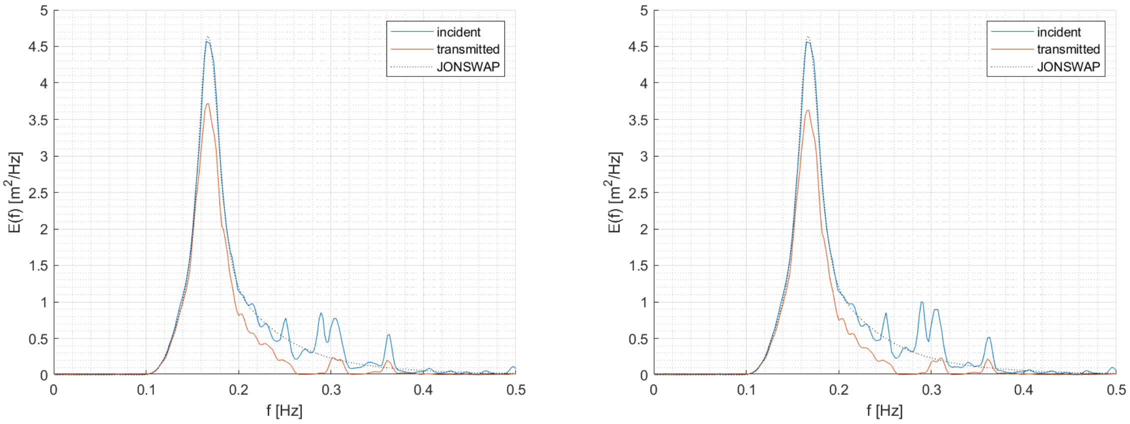

(c) System size $n_{FL} = 12$

(d) System size $n_{FL} = 18$

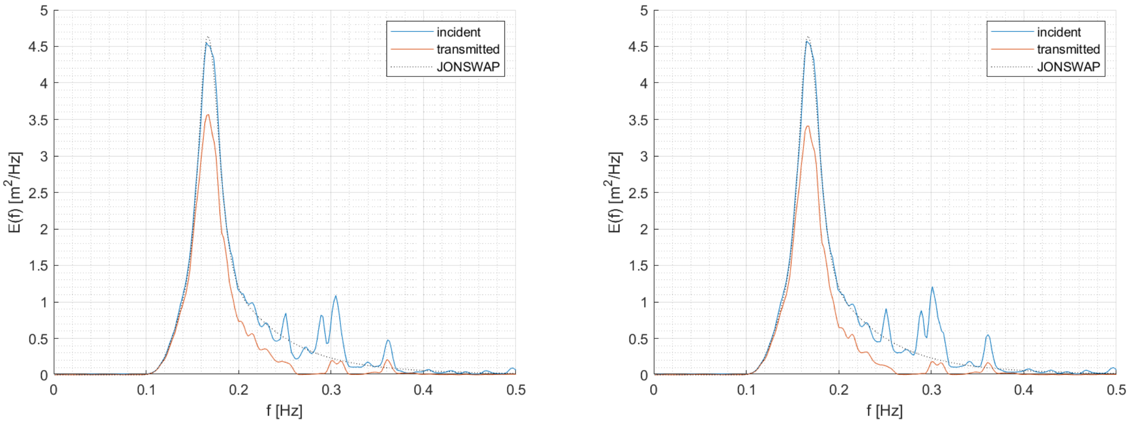

(e) System size $n_{FL} = 24$

(f) Maximum system size $n_{FL} = 33$

Figure K.2: Smoothed variance density spectra E as a function of the wave frequency f for irregular wave test 26 ($H_s = 2$ m, $T_p = 6$ s at offshore scale). Variance density is plotted for the incident wave spectrum (first 4 wave gauges) and transmitted wave spectrum (last 4 wave gauges), as well as the theoretical JONSWAP spectrum that the test was initialized at.

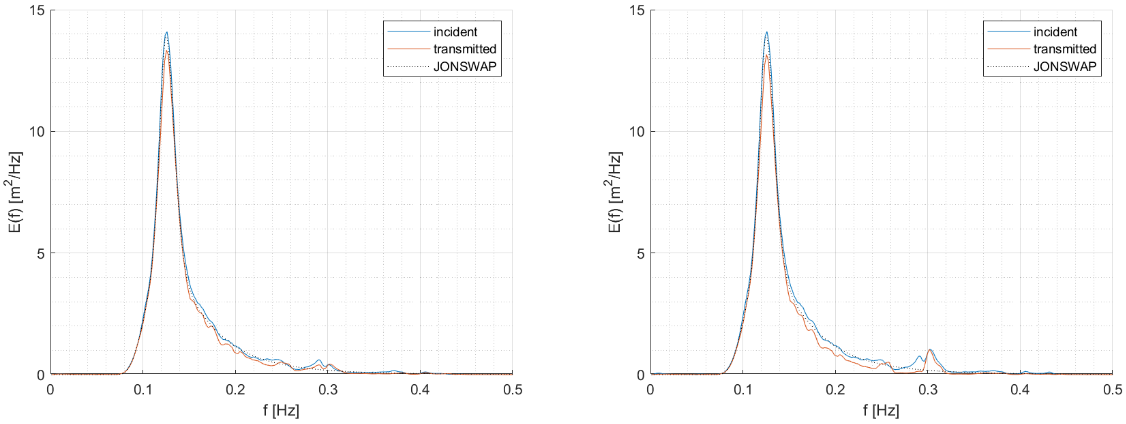

(a) Calibration test $n_{FL} = 0$

(b) System size $n_{FL} = 6$

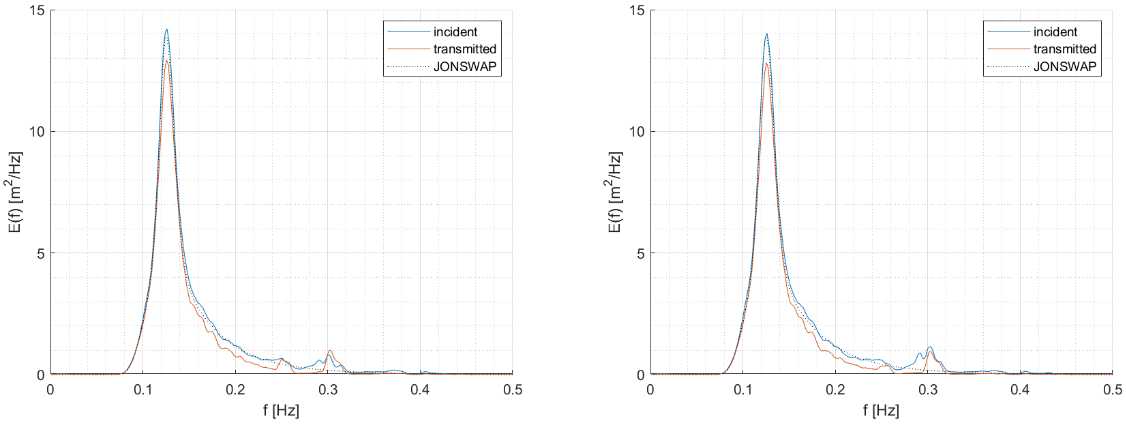

(c) System size $n_{FL} = 12$

(d) System size $n_{FL} = 18$

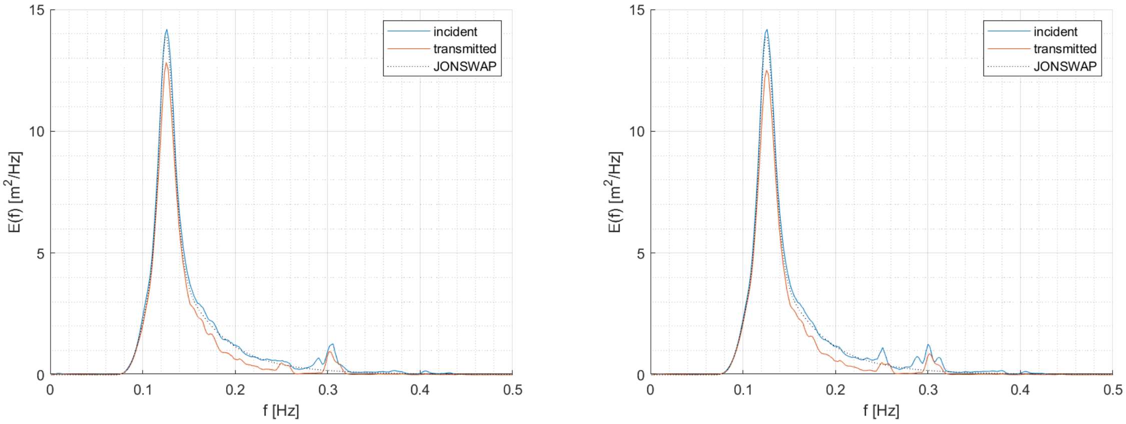

(e) System size $n_{FL} = 24$

(f) Maximum system size $n_{FL} = 33$

Figure K.3: Smoothed variance density spectra E as a function of the wave frequency f for irregular wave test 27 ($H_s = 3$ m, $T_p = 8$ s at offshore scale). Variance density is plotted for the incident wave spectrum (first 4 wave gauges) and transmitted wave spectrum (last 4 wave gauges), as well as the theoretical JONSWAP spectrum that the test was initialized at.

New

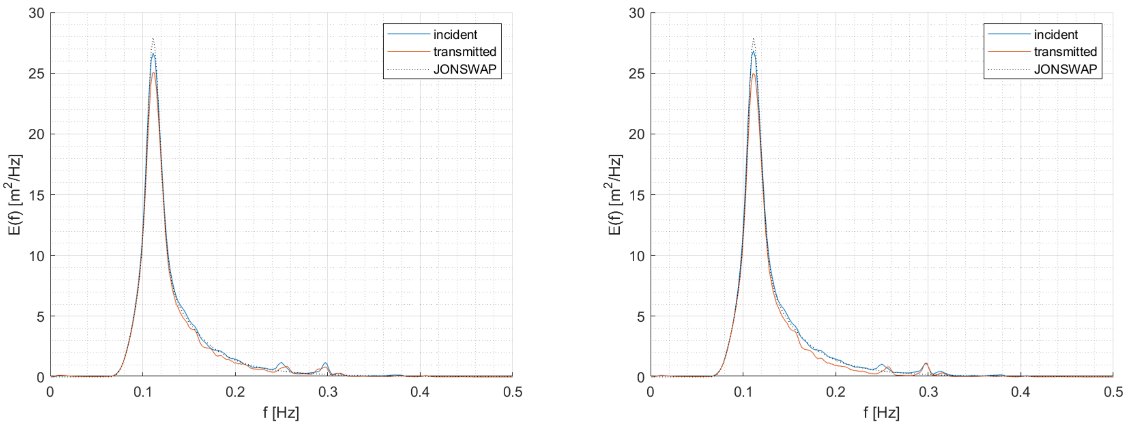

(a) Calibration test $n_{FL} = 0$

(b) System size $n_{FL} = 6$

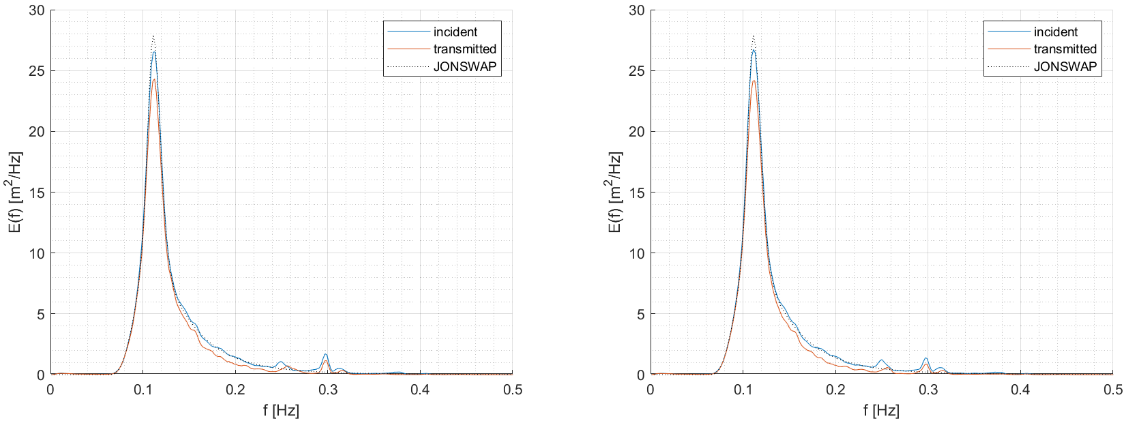

(c) System size $n_{FL} = 12$

(d) System size $n_{FL} = 18$

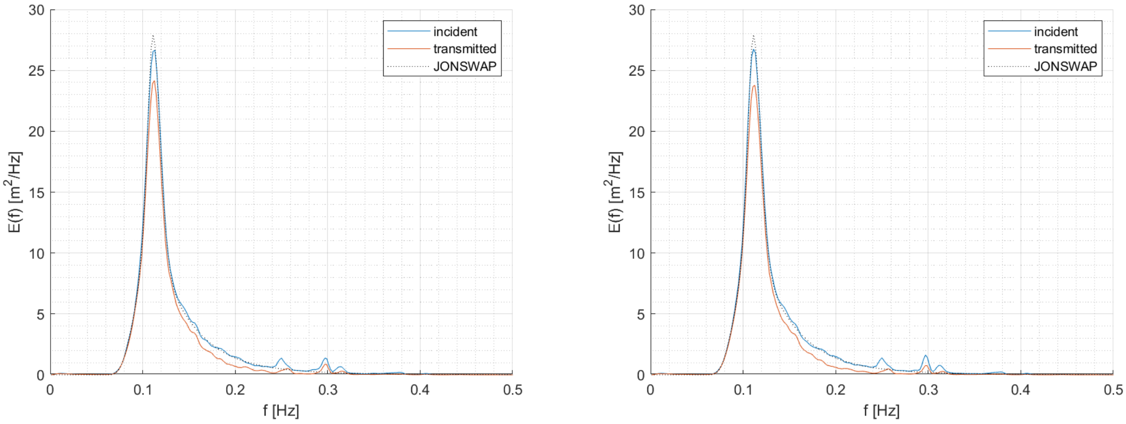

(e) System size $n_{FL} = 24$

(f) Maximum system size $n_{FL} = 33$

Figure K.4: Smoothed variance density spectra E as a function of the wave frequency f for irregular wave test 28 ($H_s = 4$ m, $T_p = 9$ s at offshore scale). Variance density is plotted for the incident wave spectrum (first 4 wave gauges) and transmitted wave spectrum (last 4 wave gauges), as well as the theoretical JONSWAP spectrum that the test was initialized at.

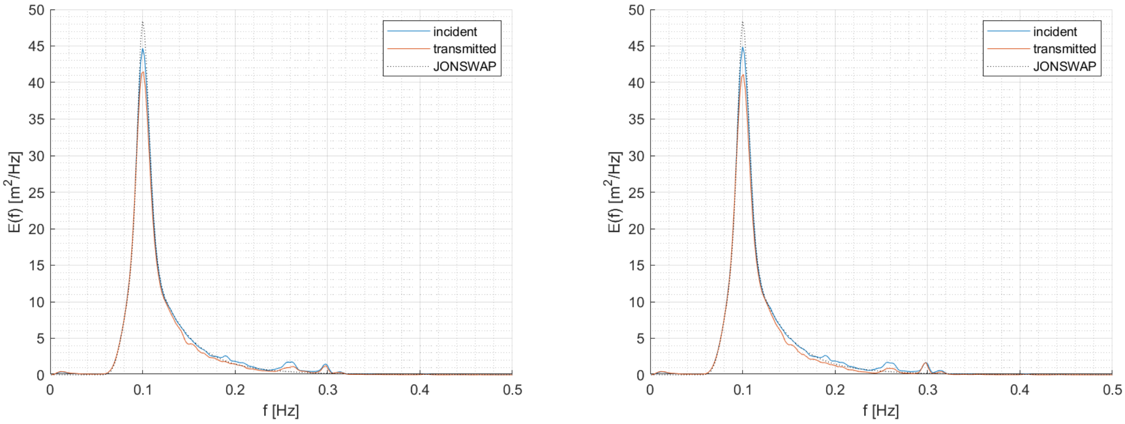

(a) Calibration test $n_{FL} = 0$ (b) System size $n_{FL} = 6$

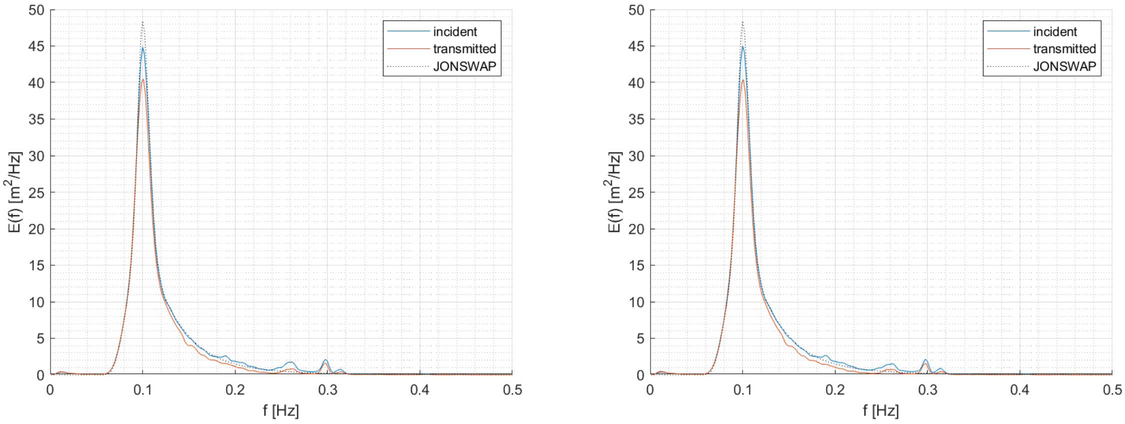

(c) System size $n_{FL} = 12$ (d) System size $n_{FL} = 18$

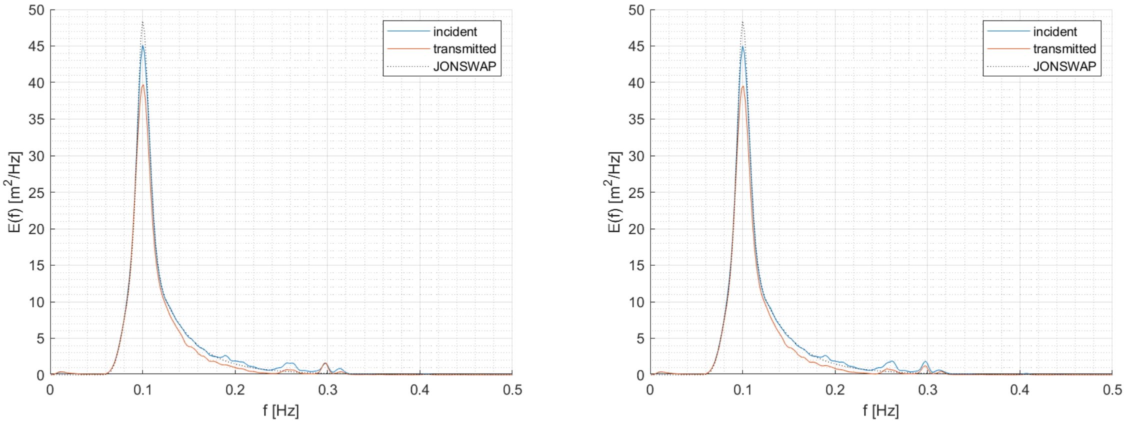

(e) System size $n_{FL} = 24$ (f) Maximum system size $n_{FL} = 33$

Figure K.5: Smoothed variance density spectra E as a function of the wave frequency f for irregular wave test 29 ($H_s = 5$ m, $T_p = 10$ s at offshore scale). Variance density is plotted for the incident wave spectrum (first 4 wave gauges) and transmitted wave spectrum (last 4 wave gauges), as well as the theoretical JONSWAP spectrum that the test was initialized at.

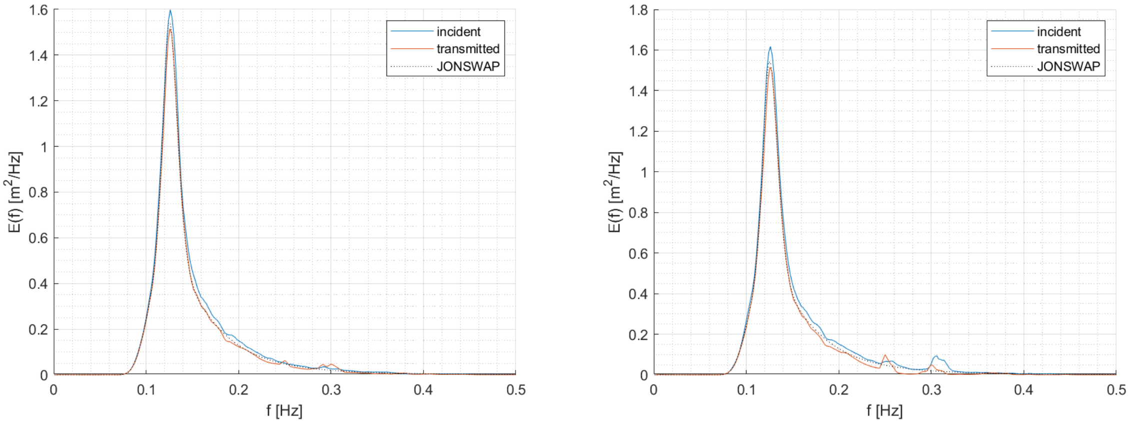

(a) Calibration test $n_{FL} = 0$

(b) System size $n_{FL} = 6$

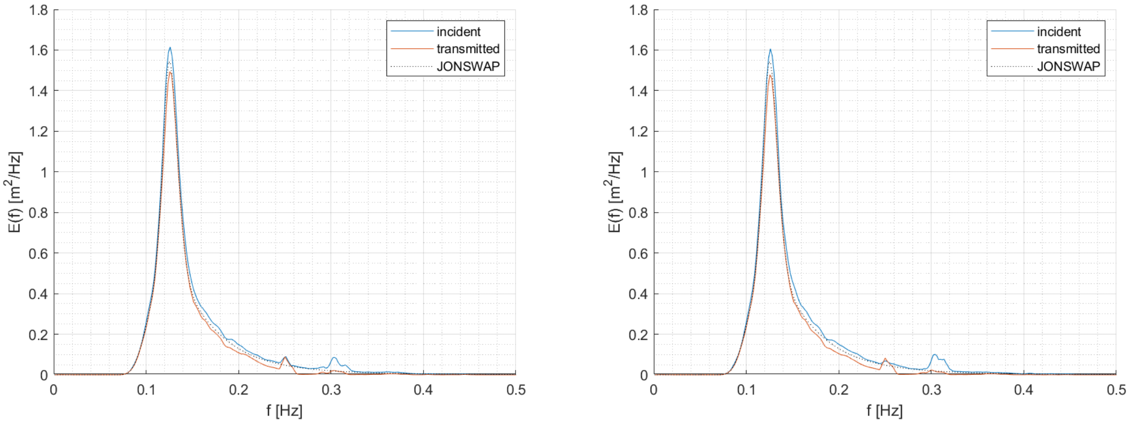

(c) System size $n_{FL} = 12$

(d) System size $n_{FL} = 18$

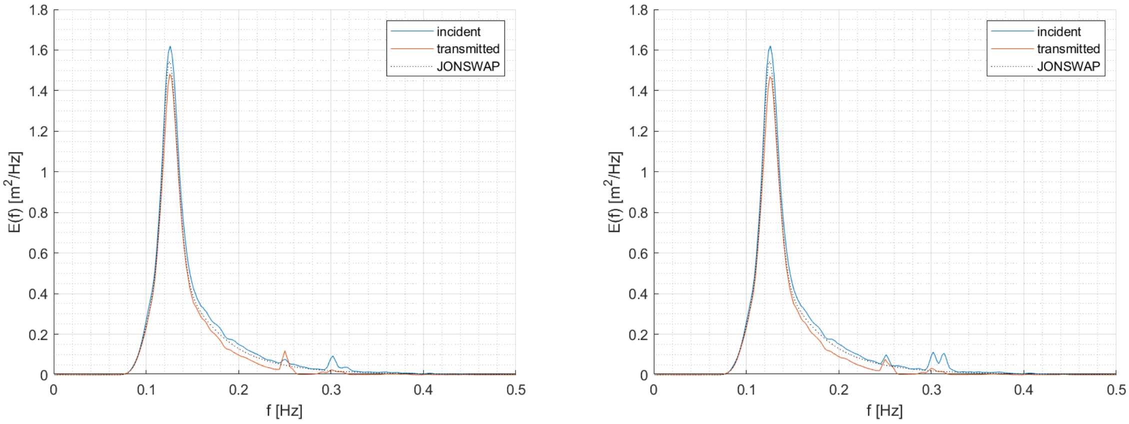

(e) System size $n_{FL} = 24$

(f) Maximum system size $n_{FL} = 33$

Figure K.6: Smoothed variance density spectra E as a function of the wave frequency f for irregular wave test 30 ($H_s = 1$ m, $T_p = 8$ s at offshore scale). Variance density is plotted for the incident wave spectrum (first 4 wave gauges) and transmitted wave spectrum (last 4 wave gauges), as well as the theoretical JONSWAP spectrum that the test was initialized at.

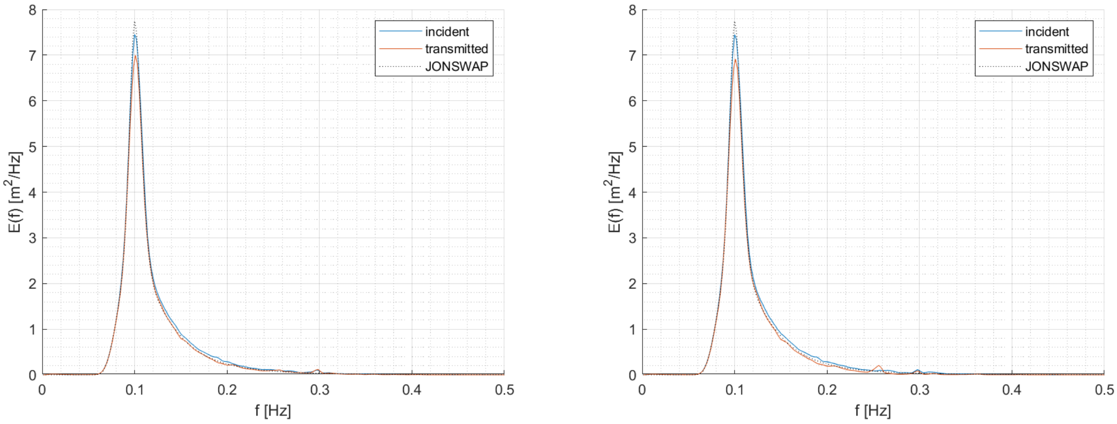

(a) Calibration test $n_{FL} = 0$ (b) System size $n_{FL} = 6$

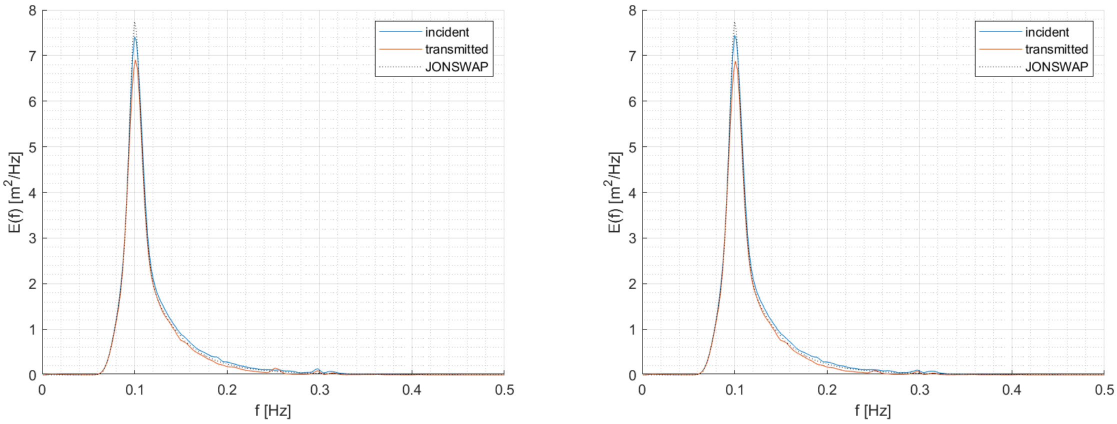

(c) System size $n_{FL} = 12$ (d) System size $n_{FL} = 18$

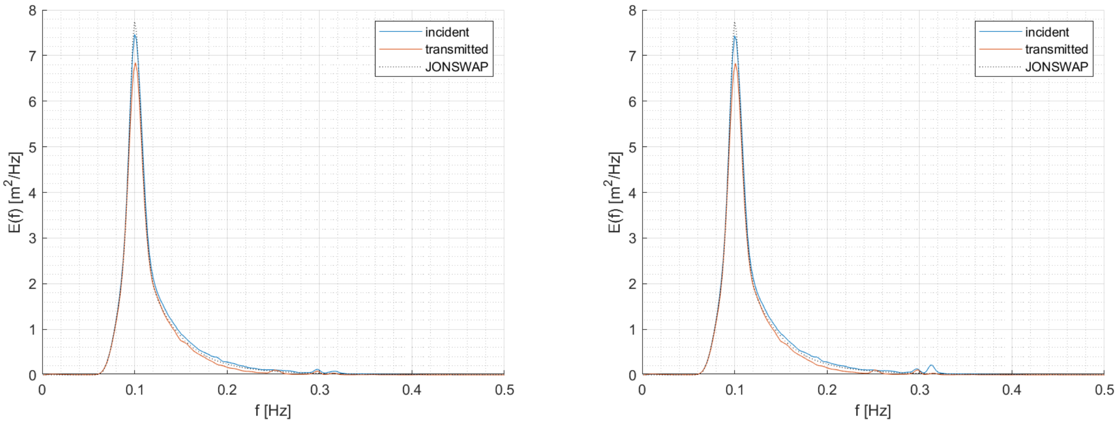

(e) System size $n_{FL} = 24$ (f) Maximum system size $n_{FL} = 33$

Figure K.7: Smoothed variance density spectra E as a function of the wave frequency f for irregular wave test 31 ($H_s = 2$ m, $T_p = 10$ s at offshore scale). Variance density is plotted for the incident wave spectrum (first 4 wave gauges) and transmitted wave spectrum (last 4 wave gauges), as well as the theoretical JONSWAP spectrum that the test was initialized at.

L

Transmission coefficients for all irregular wave tests

The transmission coefficients K_t, computed in each frequency interval with upper bound f_j, is shown in Figure L.1. Each plot shows a different system configuration with a different number of floater arrays n_{FL}. The values for all the irregular wave tests 25 - 31 are shown in each subplot, as well as the mean over these tests. These test-IDs correspond with different irregular wave conditions (and thus different incoming wave spectra) as defined in Table I.2.

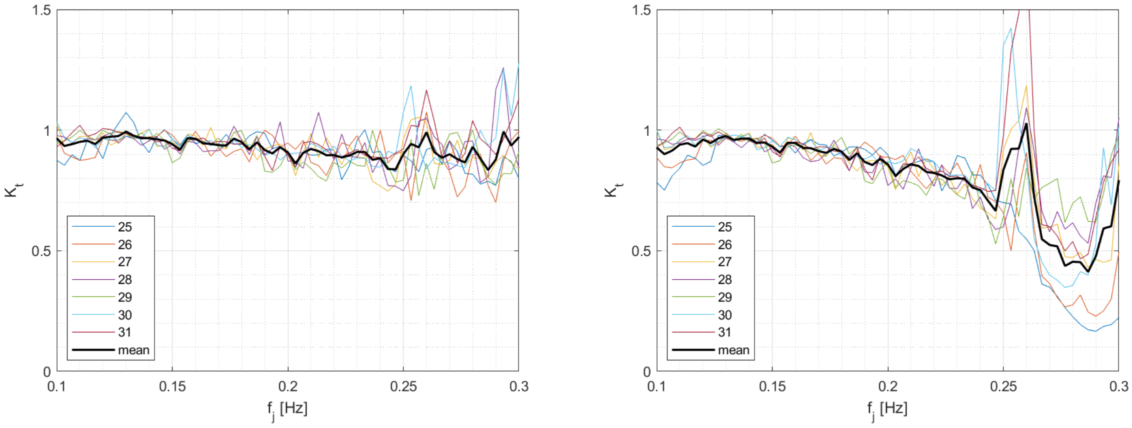

(a) Calibration test $n_{FL} = 0$

(b) System size $n_{FL} = 6$

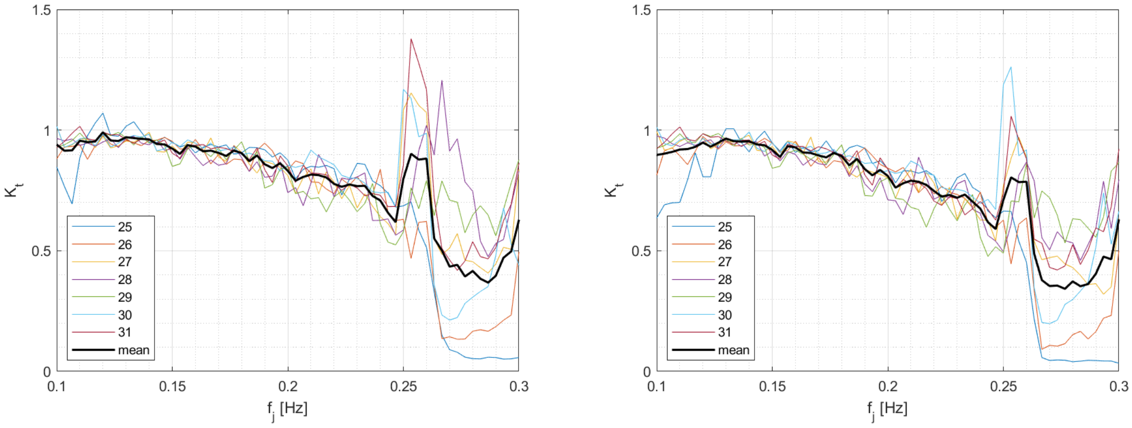

(c) System size $n_{FL} = 12$

(d) System size $n_{FL} = 18$

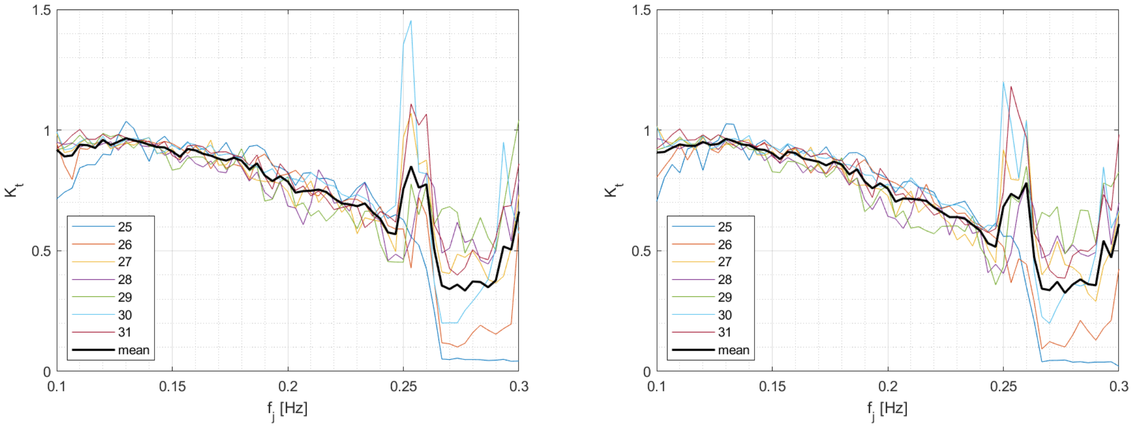

(e) System size $n_{FL} = 24$

(f) Maximum system size $n_{FL} = 33$

Figure L.1: Transmission coefficient K_t computed in each frequency interval with upper bound f_j for the irregular wave tests. Values for each irregular wave test are shown, with test-IDs 25-31 corresponding to the wave conditions given in Table I.2. The mean over these transmission values is shown in black.

M

Additional discussion points basin test

Apart from the discussion points that were presented in Chapter 6, more discussion points and suggestions are presented in this appendix.

Regular wave test results

- Measurement uncertainties could be large due to the small working scale. $H = 0.04$ m used as wave height, so small differences in surface elevation measurement can cause large relative errors. Examples could be measurement errors due to 'white wash' waves, a different mooring pretension, waves that were not dampened out completely, etc.
- Influence of second order stokes waves instead of linear
- Influence of three-dimensional diffraction or radiation effectsthat were present in the 2D setup used, and amount water passing next to the object (although minimised)
- Effect of mooring contributions. Structure moved back and forth, mooring forces increased less than linearly with number of floaters. Mooring forces were not kept entirely constant over the test runs
- When analysing the reflected signal in calibration tests before the time that a wave could travel back, values K_r up to 0.04 were found. Gives error indication and questions in splitting procedure wave analysis. Error was too large to say anything quantitatively about short timespan reflections.
- What has now been defined as reflection, could also be redirection of waves due to radiation from the structure movement. Defining wave components *b* and *e* in Figure 4.4 as reflections from the structure might thus be an incorrect interpretation, as these could also be parts of the radiated waves.
- Friction from the flume influences results; $K_t < 1$ for calibration tests (has been included in analysis)
- Standing waves could influence measurements surface elevation: location of the WHM matters (either in node or antinode)
- $K_t > 1$ values for some calibration tests, but no energy is added along the flume
- Definition dissipation parameter from $K_t^2 + K_r^2 + K_d^2 = 1$, although $K_r < 0$ for some values.

Irregular wave tests results

- Spectral results: longer running time / repitition of irregular tests could increase accuracy of spectra. Infinite time series needed for Fourier Transform is now approximated with 1100 waves.

- Define gain of wave paddle better such that the waves actually represent the JONSWAP spectrum at the location of WHM 1-4. Gain 0.84 seems to have worked best. (gain was kept constant for various system sized, and reflection and transmission are always defined as a proportion of the incoming signal thus fine)
- Spectral transmission coefficient results $K_t(f)$: use weighted average to energy value instead of regular mean: For the tests with irregular wave spectra, the amount of wave energy in the regime $f > 0.25$ Hz varied between 60% (test 25) and 8% (tests 29 and 31), which indicates how many of the high-frequent waves were present. This means more confidence lies in the tests with a low peak period T_p when looking at the high frequency range. The transmission coefficient was now computed as a simple average over all spectral wave tests, but a weighted average with respect to the amount of wave energy present in the spectrum for each frequency f could give more accurate results.
- Include backward propagating wave spectra, analysis on reflection here as well. More difficult as waves of changing characteristics are sent out
- Look into differences in wave response between regular and irregular wave tests, as the type of waves could also be of influence to the transmission results. Spectral waves will not allow for the structure to act as a perfect wave follower as the waves change over time.

Possible improvements on test procedure

- Visually changes in model: torn in U shape: gap size changed because rubber cords slipped underneath the zip ties
- Mooring tension changed a bit as the test continued because the structure deformed a little
- Active dampening at the back end of the flume, or larger flume such that time for reflection to occur is longer. Also has negative effects because it is not a passive system any more: influences energy sent into the flume
- There are some advantages of disabling the ARC: constant amount of energy sent into the flume. At least add some tests where this is done.

New research directions suggested

- 3D setup, test various incoming angles θ. Response could be very different if waves are incident at $\theta = 45\,\mathrm{deg}$, stiffness of structure higher
- Further research dissipation and reflection / radiation effects: possible tests with a fixed floating object to simulate the diffraction effects, radiation could be measured by oscillating the structure in an initially still flume
- More tests for the higher frequencies, to see exact frequency dependence. Zoom in at interesting area: what happens exactly when $K_t < 1$ (dissipation or reflection)? Answer last research question better (reflection vs dissipation)
- Research wave height dependence in different region where $K_t \not\approx 1$
- More tests could be done with different water depth, other wave conditions (maybe different flume such that the wave envelope is also different)
- Alter floater characteristics to determine dependence on floater dimensions or mooring

  Stay more in linear regime such that results can be compared with airy wave theory based numeric model
- Look into IMU data that was collected to study floater dynamics: difference in behaviour front and back floater.

Bibliography

[1] Internal Source Oceans of Energy. 2012.

[2] Matthieu Ancellin and Frédéric Dias. Capytaine : a Python-based linear potential flow solver The capytaine Python package. *Jounral of Open Source Software*, 4:1–3, 2019. doi: 10.21105/joss.01341.

[3] Emil Andersson. *Application of the open source code Nemoh for modelling of added mass and damping in ship motion simulations*. PhD thesis, KTH Royal Institute of Technology Stockholm, 2018. URL `http://www.diva-portal.org/smash/get/diva2:1263450/FULLTEXT01.pdf`.

[4] ANSYS. AQWA User Manual. 2012. URL `https://cyberships.files.wordpress.com/2014/01/wb_aqwa.pdf`.

[5] Arie Cornelis Biesheuvel. *Effectiveness of Floating Breakwaters*. PhD thesis, 2013.

[6] J. L. BLACK and C. C. MEI. Radiation and Scattering of Water Waves By Rigid Bodies, Part 1: General Aspects and Horizontal Rectangular Cylinders. *Journal of Fluid Mechanics*, 46((1970)): 151–164, 1970.

[7] G. Chang, K. Ruehl, C. A. Jones, J. Roberts, and C. Chartrand. Numerical modeling of the effects of wave energy converter characteristics on nearshore wave conditions. *Renewable Energy*, 89 (December 2017):636–648, 2016. ISSN 18790682. doi: 10.1016/j.renene.2015.12.048. URL `http://dx.doi.org/10.1016/j.renene.2015.12.048`.

[8] Limin Chen, Guanghua He, Harry B. Bingham, and Yanlin Shao. Gap resonance of fixed floating multi caissons. *Proceedings of the International Conference on Offshore Mechanics and Arctic Engineering - OMAE*, 7A-2019:1–9, 2019. doi: 10.1115/OMAE2019-96383.

[9] Young-Kwan Choi. A study on power generation analysis of floating pv system considering environmental impact. *International Journal of Software Engineering and Its Applications*, 8:75–84, 01 2014. doi: 10.14257/ijseia.2014.8.1.07.

[10] W.E. Cummins. The Impulse Response Function and Ship Motions. In *Symposium on Ship Theory*, Hamburg,, 1962. URL `https://dome.mit.edu/handle/1721.3/49049`.

[11] M.A. da Graça Neves, M. Losada, I.J. Losada. Short-Wave and Wave Group Scattering by Submerged Porous Plate. *Journal of Engineering Mechanics*, 126(October):1048–1056, 2000.

[12] Jian Dai, Chien Ming Wang, Tomoaki Utsunomiya, and Wenhui Duan. Review of recent research and developments on floating breakwaters. *Ocean Engineering*, 158(October 2017):132–151, 2018. ISSN 00298018. doi: 10.1016/j.oceaneng.2018.03.083. URL `https://doi.org/10.1016/j.oceaneng.2018.03.083`.

[13] Ranadev Datta and Debabrata Sen. A B-spline-based method for radiation and diffraction problems. *Ocean Engineering*, 33(17-18):2240–2259, 2006. ISSN 00298018. doi: 10.1016/j.oceaneng.2005.12.002.

[14] Roy de Winter. *Designing Ships using Constrained Multi-Objective Efficient Global Optimization*. PhD thesis, Universiteit Leiden, 2017.

[15] Deltares. NEMOH Introductory User Guide version March, 2018. pages 1–25, 2018.

[16] DNV GL. Energy Transition Outlook 2020 - A global and regional forecast to 2050. *Dnv Gl Energy Transition Outlook*, 2020. URL `https://eto.dnvgl.com/2020/index.html`.

[17] Arnav Doss. *Impact of box-type floating breakwater on motion response of hydrodynamically coupled floating platforms downstream*. PhD thesis, Delft University of Technology, 2020. URL `https://repository.tudelft.nl/islandora/object/uuid:1d2dbe5d-d2d5-47d6-a218-081f007060ec/datastream/OBJ/download`.

[18] Ghassan Elchahal, Rafic Younes, and Pascal Lafon. Parametrical and motion analysis of a moored rectangular floating breakwater. *Journal of Offshore Mechanics and Arctic Engineering*, 131(3): 1–11, 2009. ISSN 08927219. doi: 10.1115/1.3124125.

[19] Mads Røge Eldrup and Thomas Lykke Andersen. Estimation of Incident and Reflected Wave Trains in Highly Nonlinear Two-Dimensional Irregular Waves. 1(1):1–22, 2019. doi: 10.1061/(ASCE)WW.1943-5460.0000497.

[20] European Environment Agency. Dashboard – Renewable energy in Europe 2020. 2020. URL `https://www.eea.europa.eu/themes/energy/renewable-energy/renewable-energy-in-europe-2020`.

[21] X. Feng and W. Bai. Hydrodynamic analysis of marine multibody systems by a nonlinear coupled model. *Journal of Fluids and Structures*, 70(January):72–101, 2017. ISSN 10958622. doi: 10.1016/j.jfluidstructs.2017.01.016. URL `http://dx.doi.org/10.1016/j.jfluidstructs.2017.01.016`.

[22] S. Zahra Golroodbari and Wilfried van Sark. Simulation of performance differences between offshore and land-based photovoltaic systems. *Progress in Photovoltaics: Research and Applications*, 28(9):873–886, 2020. ISSN 1099159X. doi: 10.1002/pip.3276.

[23] Floris Groenendijk, Paul Bikker, Rolf Blaauw, Willem Brandenburg, Sander van den Burg, Jan Wilco Dijkstra, Luca Van Duren, Jaap Van Hal, Paulien Harmsen, Robbert Jak, Pauline Kamermans, Jelle Van Leeuwen, Van Krimpen, Henri Prins, Sjoerd Van Der Putten, Joost Schouten, Marian Stuiver, Adrie Van Der Werf, Niels Jacobsen, Rene Joosten, Anna De Kluijver, Bo Paulsen, and Julia Wald. North-Sea-Weed-Chain: Sustainable Seaweed from the North Sea; an exploration of the value chain. *IMARES*, (May), 2016. URL `https://www.wur.nl/nl/download/Rapport-North-Sea-Weed-Chain.htm`.

[24] Y. Guo, S. C. Mohapatra, and C. Guedes Soares. Wave interaction with a rectangular long floating structure over flat bottom. *Progress in Maritime Technology and Engineering - Proceedings of the 4th International Conference on Maritime Technology and Engineering, MARTECH 2018*, (2011): 647–656, 2018. doi: 10.1201/9780429505294-72.

[25] Lyndell Z. Hales. Floating Breakwaters: State-of-the-Art Literature Review. *U.S.Army, Corps of Engineers Coastal Engineering Research Center*, pages 1–289, 1981.

[26] K. Hasselmann, T.P. Barnett, E. Bouws, H. Carlson, D.E. Cartwright, P. Kruseman, A. Meerburg, P. Müller, D.J. Olbers, K. Richter, W. Sell, and H. Walden. Measurement of Wind-Wave Growth and Swell Decay during the Joint North Sea Wave Project (JONSWAP). *Deutschen Hydrograpischen Zeitschrift*, 8(12):1–95, 1973. URL `https://repository.tudelft.nl/islandora/object/uuid%3Af204e188-13b9-49d8-a6dc-4fb7c20562fc`.

[27] T. S. Hedges. Regions of validity of analytical wave theories. *Proceedings of the Institution of Civil Engineers: Water, Maritime and Energy*, 112(2):111–114, 1995. ISSN 17537819. doi: 10.1680/iwtme.1995.27656.

[28] Leo Holthuijsen. *Waves in Oceanic and Coastal Waters*. Cambridge University Press, 2007. doi: 10.2277/0521860288.

[29] Niels G. Jacobsen, David R. Fuhrman, and Jørgen Fredsøe. A wave generation toolbox for the open-source CFD library: OpenFoam. *International Journal for Numerical Methods in Fluids*, 65 (October 2011):236–253, 2011. ISSN 02712091. doi: 10.1002/fld.

[30] J.M.J. Journée and W.W. Massie. *Offshore Hydromechanics (lecture notes)*. Delft University of Technology, 2 edition, 2008.

[31] F J Koppes. *Numerical Modelling of Interconnected Floating Solar Energy Platforms*. PhD thesis, TU Delft, 2019. URL `https://oceansofenergy.blue/`.

[32] E. Koutandos, P. Prinos, and Xavi Gironella. Floating breakwaters under regular and irregular wave forcing: Reflection and transmission characteristics. *Journal of Hydraulic Research*, 43(2): 174–188, 2005. ISSN 00221686. doi: 10.1080/00221686.2005.9641234.

[33] Tara LaForce. PE281 Boundary Element Method Course Notes. 2006. URL `https://web.stanford.edu/class/energy281/BoundaryElementMethod.pdf`.

[34] H. Lamb. *Hydrodynamics*. Dover Publications, Inc., New York, 6 edition, 1936.

[35] Bernard Le Méhauté. *An Introduction to Hydrodynamics and Water Waves*. Springer, 1976. ISBN 978-3-642-85569-6,978-3-642-85567-2.

[36] C.-H. Lee. WAMIT Theory Manual. *WAMIT Theory Manual*, pages 1–19, 1995.

[37] C.H. Lee and J.N. Newman. First- and second-order wave effects on a submerged spheroid. *Journal of Ship Research*, 35(3):183–190, 1991. doi: 10.5957/jsr.1991.35.3.183.

[38] Hui Liang, Kie Hian Chua, and Hongchao Wang. Wave heading effects on gap resonance with energy dissipation. In *Proceedings of the Fourteenth (2020) ISOPE Pacific-Asia Offshore Mechanics Symposium*, number November, pages 110–114, Dalian, China, 2020. ISBN 9781880653838. URL `https://www.researchgate.net/publication/345788136_Wave_heading_effects_on_gap_resonance_with_energy_dissipation`.

[39] P. Linton, C.M. McIver. *Handbook of Mathematical Techniques for Wave/Structure Interactions*. Chapman and Hall/CRC, 2001. ISBN 1584881321. doi: https://doi.org/10.1201/9781420036060.

[40] Philip L□F Liu and Madjid Abbaspour. An integral equation method for the diffraction of oblique waves by an infinite cylinder. *International Journal for Numerical Methods in Engineering*, 18(10): 1497–1504, 1982. ISSN 10970207. doi: 10.1002/nme.1620181005.

[41] Yingyi Liu. HAMS : A Frequency-Domain Preprocessor for Wave-Structure Interactions — Theory , Development , and Application. *Journal of Marine Science and Engineering*, 7(81):1–19, 2019. doi: 10.3390/jmse7030081. URL `https://www.mdpi.com/2077-1312/7/3/81`.

[42] Yong Liu and Hua Jun Li. A new semi-analytical solution for gap resonance between twin rectangular boxes. *Journal of Engineering for the Maritime Environment*, 228(1):3–16, 2014. ISSN 20413084. doi: 10.1177/1475090213482893.

[43] Eva Loukogeorgaki, Oral Yagci, and M. Sedat Kabdasli. 3D Experimental investigation of the structural response and the effectiveness of a moored floating breakwater with flexibly connected modules. *Coastal Engineering*, 91:164–180, 2014. ISSN 03783839. doi: 10.1016/j.coastaleng.2014.05.008. URL `http://dx.doi.org/10.1016/j.coastaleng.2014.05.008`.

[44] Lin Lu, Bin Teng, Liang Sun, and Bing Chen. Modelling of multi-bodies in close proximity under water waves - Fluid forces on floating bodies. *Ocean Engineering*, 38(13):1403–1416, 2011. ISSN 00298018. doi: 10.1016/j.oceaneng.2011.06.008. URL `http://dx.doi.org/10.1016/j.oceaneng.2011.06.008`.

[45] E. Macagno. Houle dans un canal présentant un passage en charge. *Le Houille Blanche*, 1953.

[46] MARIN. 3-D potential theory including wave diffraction: DIFFRAC. page 317, 2013. URL `https://www.marin.nl/facilities-and-tools/software/diffrac`.

[47] J. Cameron McNatt, Aaron Porter, and Kelley Ruehl. Comparison of numerical methods for modeling the wave field effects generated by individual wave energy converters and multiple converter wave farms. *Journal of Marine Science and Engineering*, 8(3), 2020. ISSN 20771312. doi: 10.3390/jmse8030168.

[48] Chiang C. Mei and Jared L. Black. Scattering of surface waves by rectangular obstacles in waters of finite depth. *Journal of Fluid Mechanics*, 38(3):499–511, 1969. ISSN 14697645. doi: 10.1017/S0022112069000309.

[49] Constantine Michailides and Demos C. Angelides. Modeling of energy extraction and behavior of a Flexible Floating Breakwater. *Applied Ocean Research*, 35:77–94, 2012. ISSN 01411187. doi: 10.1016/j.apor.2011.11.004. URL `http://dx.doi.org/10.1016/j.apor.2011.11.004`.

[50] Sarat Chandra Mohapatra and C. Guedes Soares. Hydroelastic response of a flexible submerged porous plate for wave energy absorption. *Journal of Marine Science and Engineering*, 8(9), 2020. ISSN 20771312. doi: 10.3390/JMSE8090698.

[51] Huu Phu Nguyen, Jeong Cheol Park, Mengmeng Han, Chien Ming Wang, Nagi Abdussamie, Irene Penesis, and Damon Howe. Representative Transmission Coefficient for Evaluating the Wave Attenuation Performance of 3D Floating Breakwaters in Regular and Irregular Waves. *Journal of Marine Science and Engineering*, 9(4):388, 2021. ISSN 20771312. doi: 10.3390/jmse9040388.

[52] G Parisella and T P Gourlay. Comparison of open-source code Nemoh with Wamit for cargo ship motions in shallow water. (October), 2016.

[53] Grégory S. Payne. Guidance for the experimental tank testing of wave energy converters. *University of Edinburgh*, 2008. URL `http://www.supergen-marine.org.uk/sites/supergen-marine.org.uk/files/publications/WEC_tank_testing.pdf`.

[54] Markel Penalba, Thomas Kelly, and John V Ringwood. Using NEMOH for Modelling Wave Energy Converters : A Comparative Study with WAMIT. 2017. URL `https://www.researchgate.net/publication/319160625_Using_NEMOH_for_Modelling_Wave_Energy_Converters_A_Comparative_Study_with_WAMIT`.

[55] Chien Ming Wang. Floating Forest: A Novel Concept of Floating Breakwater-Windbreak Structure. In *Lecture Notes in Civil Engineering*, pages 219–234. Springer, 41 edition, 2020. ISBN 9789811387425. doi: 10.1007/978-981-13-8743-2_12.

[56] Chien Ming Wang, Eiichi Watanabe, and Tomoaki Utsunomiya. *Very large floating structures*. 2006. ISBN 9781482265927. doi: 10.1201/9781482265927.

[57] H. Y. Wang and Z. C. Sun. Experimental study of a porous floating breakwater. *Ocean Engineering*, 37(5-6):520–527, 2010. ISSN 00298018. doi: 10.1016/j.oceaneng.2009.12.005.

[58] A. N. Williams, H. S. Lee, and Z. Huang. Floating pontoon breakwaters. *Ocean Engineering*, 27 (3):221–240, 2000. ISSN 00298018. doi: 10.1016/S0029-8018(98)00056-0.

[59] Siming Zheng and Yongliang Zhang. Wave diffraction and radiation by multiple rectangular floaters. *Journal of Hydraulic Research*, 54(1):102–115, 2016. ISSN 00221686. doi: 10.1080/00221686.2015.1090492.

[60] Y. H. Zheng, Y. G. You, and Y. M. Shen. On the radiation and diffraction of water waves by a rectangular buoy. *Ocean Engineering*, 31(8-9):1063–1082, 2004. ISSN 00298018. doi: 10.1016/j.oceaneng.2003.10.012.